
HIGHLY CHARGED ION JETS FROM MEDIUM FLUX LASER PLASMAS

Vom Fachbereich Physik der
TECHNISCHEN UNIVERSITÄT DARMSTADT

zur Erlangung des Grades eines
Doktors der Naturwissenschaften
(Dr. rer. nat.)

genehmigte Dissertation von
Dipl.-Phys. Gonzalo Rodríguez Prieto,
aus Pontevedra

Referent: Prof. Dr. D. H. H. Hoffmann
Korreferent: Prof. Dr. M. Roth
Tag der Einreichung: 30. Oktober 2006
Tag der mündlichen Prüfung: 5. Juli 2006

Darmstadt 2006

D 17

To my parents, Maty, Félix, and Asia,
because of so many things.

Zusammenfassung

Die Arbeitsgruppe Plasmaphysik an der Gesellschaft für Schwerionenforschung (GSI) untersucht die Wechselwirkung von beschleunigten Schwerionen mit lasererzeugten, dichten Plasmen. Hierfür ist die experimentelle Charakterisierung der Laserplasmen wichtig, die trotz der steigenden Anzahl von analytischen Modellen und Simulationen ein aktives Feld wissenschaftlicher Untersuchungen bleibt. Durch Messung der Dopplerverschiebung von Spektrallinien im Röntgenbereich wurde in Experimenten bei der GSI sowie in anderen Laboratorien mit lasererzeugten Plasmen bei mittleren Laserintensitäten von 10^{11} - 10^{12} W/cm² die Präsenz von Ionen mit kinetischen Energien im MeV-Bereich nachgewiesen.

In dieser Arbeit werden Experimente präsentiert, die die Bedingungen zur Erzeugung dieser Ionen erfüllen. Das Lasersystem nhelix wurde eingesetzt, um lange Jets hochgeladener Ionen mit gemessenen kinetischen Energien unterhalb 9 keV zu charakterisieren. Messungen mit Röntgenlochkameras und ortsauflösenden Röntgenspektrometern zeigen eine Länge der Jets von mehr als 4 mm.

Die Expansionseigenschaften eines während der Laserpulsdauer quasistatischen Plasmas sowie des später expandierenden Plasmas wurden miteinander verglichen. Für diesen Vergleich wurden an dem expandierenden Plasma Messungen mit einer Schmierbildkamera (Lichtemission im sichtbaren Spektrum), einem UV-Spektrometer, sowie Messungen der Röntgenemission im quasistatischen Bereich durchgeführt.

Die beobachtete Jetstruktur wird erzeugt, wenn der Laserfokus in einem Abstand von 0.5 bis 1.0 mm vor der Targetoberfläche liegt. Zur Erzeugung der Jets muss, unabhängig von den anderen Parametern, der Laserfluss oberhalb der Schwelle von 10^{12} W/cm² liegen. Eine Abweichung der Laser-Einfallrichtung von der Normalen führt zu einer Steigerung der Jetlänge.

Es ist möglich, diese Resultate auf Targets, die bei Experimenten zur Wechselwirkung von Schwerionenstrahlen und Laserplasmen eingesetzt werden, zu erweitern. Die Laser-Plasma Wechselwirkung findet in einer wenige nm dicken Schicht statt, während die verwendeten Targets eine Dicke von einigen Mikrometern haben. Die Erzeugung von Jets hochgeladener Ionen führt zu einem größeren Wechselwirkungsvolumen der Schwerionen im lasererzeugten Plasma und stellt somit eine Ver-

besserung der Möglichkeiten zur Untersuchung von Schwerionenstrahl-Plasma Wechselwirkungen dar.

Abstract

The plasma physics group at the Gesellschaft für Schwerionenforschung (GSI) studies the interaction of accelerated heavy ions with dense laser created plasmas with special focus on the energy loss of the ions. Thus experimental characterization of the laser plasmas becomes important, and despite the increased quantity of analytical models and simulations, it still is an active area of research. In experiments made at GSI and other laboratories, the presence of ions with MeV kinetic energies has been found from laser created plasmas with medium laser fluxes of 10^{11} - 10^{12} W/cm². They were found through measurement of the doppler shift of spectral lines in the X ray range.

Experiments performed to establish the conditions of this ion generation are presented here. Large jets of highly charged ions have been produced with the *nhelix* laser system, while their measured kinetic energies were not larger than 9 keV. The jet length has been measured and resulted to be 4 mm, detected with X ray pinhole cameras and spatially resolved X ray spectrometers.

Expansion properties of the quasi-static plasma during the laser pulse and the laser expansion have been compared. The comparison has been made with light emission recorded with a visible spectral range streak camera and an ultraviolet spectrometer from the expanding plasma and the X ray emission from the quasi-static state.

The observed jet structure is created when the laser focus is at distances of 0.5 to 1.0 mm in front of the target surface. There is a laser flux threshold for jet generation in the order of 10^{12} W/cm², independently of other parameters. Changes in the laser beam angle incidence from normal to non normal lead to an increment of jet length.

It is possible to extend these results to the targets suitable for ion beam-laser interaction experiments. The laser absorption in the planar laser-plasma interaction takes place near the critical density in a sheath of nanometers, while the targets have micrometers thickness. The creation of the highly charged ion jets will increase the interaction volume of the ion beam-laser created plasma thus providing a better tool for studying the ions' energy loss.

Contents

| | | |
|----------|---|-----------|
| 1 | Introduction | 13 |
| 2 | Theoretical background | 17 |
| 2.1 | Plasma definitions and concepts | 17 |
| 2.1.1 | Plasma temperature | 17 |
| 2.1.2 | Local thermal equilibrium | 18 |
| 2.1.3 | Debye length | 18 |
| 2.1.4 | The plasma parameter | 19 |
| 2.1.5 | Particle motion in magnetic fields | 20 |
| | Magnetic pressure | 20 |
| 2.1.6 | Plasma frequency | 20 |
| 2.1.7 | Critical density | 21 |
| 2.1.8 | Radiative processes in plasmas | 21 |
| 2.2 | Plasma generation | 22 |
| 2.2.1 | Artificial plasmas | 22 |
| | Low-pressure cold-cathode discharges | 23 |
| | Arc discharge | 23 |
| | Plasma guns | 23 |
| | Alkali metal vapor plasma—Q machines | 23 |
| | Radio frequency produced plasmas | 24 |
| | Tokamak plasmas | 24 |
| | Z-pinch plasmas | 24 |
| 2.2.2 | Laser created plasmas | 25 |
| | Laser light absorption | 25 |
| | Quasi-steady plasma state | 26 |
| | Plasma expansion | 26 |
| | Magnetic field generation in laser created plasmas | 28 |
| 2.3 | Introduction to spectroscopic plasma parameters diagnostics | 28 |

| | | |
|----------|---|-----------|
| 3 | Experimental setup and techniques | 33 |
| 3.1 | The <i>nhelix</i> laser system | 33 |
| 3.1.1 | The <i>nhelix</i> setup | 33 |
| 3.1.2 | Laser flux measurements | 36 |
| | Laser pulse temporal profile | 37 |
| | Laser energy | 37 |
| | Focal spot | 38 |
| 3.2 | Plasma Diagnostics | 40 |
| 3.2.1 | Pinhole cameras | 40 |
| | Working principle of pinhole cameras | 40 |
| | X ray pinhole camera characteristics | 42 |
| | Plasma angular distribution from X ray pinhole images | 42 |
| 3.2.2 | Visible streak camera | 44 |
| | Streak Cameras Working Principle | 44 |
| | Laboratory Setup | 45 |
| | Camera Calibration and Plasma Velocity Measurement | 45 |
| 3.2.3 | Spectrometers | 46 |
| 3.2.4 | The VM-502 spectrometer | 47 |
| 3.2.5 | Focusing X ray spectrometers | 48 |
| | Operation of the focusing X ray spectrometers | 48 |
| | FSSR 1-D | 49 |
| | FSSR 2-D | 49 |
| 3.2.6 | X ray film calibration | 50 |
| 3.3 | General setups | 52 |
| 3.3.1 | Normal incidence setup | 52 |
| | FSSR spectral adjustment for <i>normal</i> incidence | 53 |
| | X ray pinhole camera | 54 |
| | Visible streak camera | 55 |
| 3.3.2 | 45° incidence | 55 |
| | FSSR | 56 |
| | X ray pinhole cameras | 57 |
| | Visible streak camera | 58 |
| 4 | Experimental Results | 59 |
| 4.1 | Plasma jets | 59 |
| 4.1.1 | Jet generation | 59 |
| 4.1.2 | Laser flux threshold | 64 |
| 4.1.3 | Influence of the laser incidence angle | 66 |
| 4.2 | Influence of the laser beam divergence in the generated plasmas | 68 |
| 4.2.1 | Non divergent laser beam | 68 |

| | | |
|----------|--|------------|
| 4.2.2 | Divergent laser beam | 72 |
| | X ray diagnostics | 73 |
| | Ultraviolet spectra results | 75 |
| 4.3 | Analysis of the ultraviolet spectra | 76 |
| 4.3.1 | Ultraviolet spectra calibration | 76 |
| 4.3.2 | Influence of the laser beam divergence | 79 |
| 5 | Conclusions and outlook | 83 |
| | Bibliography | 86 |
| | Index | 95 |
| A | Program ANGULINT.f90 | 97 |
| B | Module DATA_WORK.f90 | 103 |
| C | Module OptDen.f90 | 107 |

Chapter 1

Introduction

Plasma is considered the fourth state of matter after solid, liquid, and gas: it is a quasineutral gas formed by charged and neutral particles that can be altered by electromagnetic fields. Typically a plasma is generated by increasing the internal energy of matter which starting from solid state will pass through liquid and gas states. If even more energy is given to this system, part or all the atoms or molecules of the system are ionized and the gas becomes a plasma if the number of ionized particles is large enough.



Figure 1.1: Aurora borealis illuminating the night sky.

In our universe 99% of the observed matter is in a plasma state. The presence of natural plasmas at the Earth surface is much more rare. One natural plasma example in the Earth surroundings is the aurora borealis, see Fig. 1.1, formed by the collision of plasma ejected from the Sun with the upper sheaths of the atmosphere. Another is the lightning, a result of the very high electric potential differences built up between soil and clouds.

Plasmas are created by mankind in laboratories and factories to study and use them. Plasma technological applications go from metal welding to the creation of protective sheaths on plastic receptacles. One of the numerous methods to create

plasma artificially is laser radiation applied to a solid target as used in the experiments performed within this work. Moreover short laser pulses (pulse width in the order of picoseconds) applied onto thin sheets can generate ions of the order of MeV, with certain control over the peak energy of the ions by the alteration of the sheath thickness [1], [2], [3]. This method of ion acceleration may be used to build more compact accelerators needed in medicine and new physics facilities.

With longer pulses, on the order of nanoseconds, extensive experimental work has initially been performed during the seventies aiming for laser fusion [4], recently reacquiring importance by the National Ignition Facility (NIF) under construction in the United States¹. The NIF facility will use 192 pulses with 10 ns time duration each to uniformly heat a spherical target mainly composed of deuterium. Such a setup is thought to reach the adequate conditions to initiate fusion of part of the target. Nanosecond laser pulses are used nowadays in the industry for plasma chemical vapour deposition. These are low flux lasers with values not higher than 10^9 W/cm², whereas the *nhelix* laser used during this work reaches values up to 10^{14} W/cm².

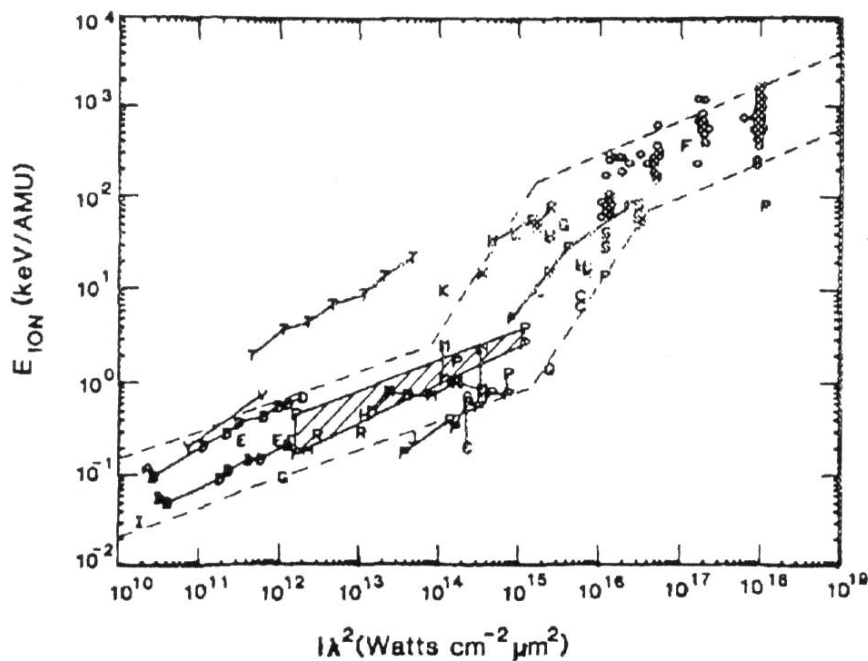


Figure 1.2: Laser fluency scaling of the ion energy. Adapted from [5]

Another use of nanosecond pulsed lasers is to study the interaction of ions with plasmas, where nanosecond plasmas are needed due to the long duration of the ion bunch generated by standard accelerators. How ions interact with different targets and lose their energy within the target is an active area of research [6], with many questions to be addressed from the beginning of its history [7]. When the stopping medium is converted into plasma, there is an increase of the energy loss of ions [8];

¹<http://www.llnl.gov/nif/>

an effect also investigated by the plasma physics group at GSI.

More uses of the nanosecond lasers are related to some of the most recent applications of laser plasmas, like X ray lasers [9] and X ray sources to be used for backlighting illumination in warm dense matter experiments.

From laser created plasmas ion velocities far from the normal thermal value, called suprathermal ions, are reached. Scale laws of these velocities with the laser flux and wavelength ($\text{flux} \cdot \lambda^2$, $I\lambda^2$ in $\text{W}/\text{cm}^2 \cdot \mu\text{m}^2$) were found by Gitomer et al. [5] with data compiled from many laser facilities, see Fig. 1.2. Ions accelerated to kinetic energies of the order of MeV for $I\lambda^2$ around $10^{12} \text{ W}/\text{cm}^2 \cdot \mu\text{m}^2$, thus far from the ones from Fig. 1.2, were detected previously at GSI and other laboratories under experimental conditions similar to those used in this work [10], [11].

With X ray pinhole cameras large jet structures were observed in coincidence with the MeV ions observed with X ray space resolved spectroscopy. In this work the suprathermal ions were not observed but the jet structures were detected by the X ray pinholes. With maximum velocities of the order of keV, the jets were characterized and the experimental conditions that lead to their formation from magnesium targets were firmly established. These experimental conditions are mainly related to the position of the last laser beam lens, that focuses the beam in front of the target surface to produce them. The relations of the quasi-stationary plasma formed within the laser pulse duration and the expanded plasma afterward were clarified and threshold laser flux values were also established.

This work starts with an introduction to plasma theory, with special attention given to the laser created plasma generation and some spectroscopic procedure to deduce the electron temperature. It continues with an explanation of the employed setup and used devices, followed by the results obtained. Finally, some conclusions are given, with an outlook to future work that remains to be done.

Chapter 2

Theoretical background

A plasma can be defined as *a quasineutral gas of charged and neutral particles which exhibits collective behaviour* [12]. The collective behaviour is caused by free electrons and ions. Since the electrons and ions are charged particles, their movements can create and alter electromagnetic fields that act collectively on the plasma, without the intervention of collisions, as happens in a normal gas. The behaviour of the ions inside the plasma can also be addressed considering their individual characteristics. The study of plasmas began in the end of the XIXth century with the experiments on ionized gases produced by electrical discharges.

Some concepts and definitions relevant for plasma physics are explained in the next section. A review of the mechanisms to produce them follows, with special attention paid to laser produced plasmas. The last section of this chapter deals with the theory of plasma diagnostics using its self generated radiation.

Section 2.1 Plasma definitions and concepts

In order to introduce concepts that will be used later on during this work, let us define and discuss some important plasma properties and states.

2.1.1 Plasma temperature

The quantity named ‘plasma temperature’ measures the average internal energy per particle of a many body system. The definition is coined from statistical thermodynamics. If a many body system relaxes through binary collisions it will reach an equilibrium state which has the temperature as a characteristic parameter that is related to the quantity of particles in a certain velocity interval through the Maxwellian distribution:

$$f(v) = \left(\frac{m}{2\pi kT}\right)^{3/2} \exp\left(\frac{-mv^2}{2kT}\right), \quad (2.1)$$

where m is their mass, v the velocity, and T the temperature. From eq. 2.1 the mean velocity $\langle v \rangle$ increases with T . Besides, the mean kinetic energy in a one dimen-

sional system is related to the mean velocity through the kinetic energy formula:

$$\langle E_k \rangle = \frac{1}{2} m \langle v^2 \rangle . \quad (2.2)$$

So the plasma temperature is related to the internal kinetic energy of the system. As electrons and ions inside the plasma usually have different kinetic energies, it is common in plasma physics to assign different temperatures for them.

2.1.2 Local thermal equilibrium

Not always a plasma reaches a stage where the ion and electron velocity distributions follow the Maxwellian one. Defining the collision frequency as the number of collisions between plasma elements per time unit, the equilibrium is obtained when the collision frequency is big. It means that the interactions between neighbor particles are incremented, so their energetic state changes fast and the achievement of a Maxwellian distribution is possible. Frequently, such conditions are achieved with diverse temperature values for the different plasma regions, so their electronic temperature is not the same. In these conditions, the plasma is in *local thermodynamic equilibrium*. Some analytical models make use of this equilibrium approximation to generate their results.

2.1.3 Debye length

The plasma charged particles are very mobile, with the electrons moving faster due to their lower mass if compared with the ions. For the same kinetic energy of 100 eV, the electron velocity is $6 \cdot 10^8$ cm/s with a value of $3 \cdot 10^6$ cm/s for magnesium ions. They feel attracted or repulsed following their charges. The electrons tend to move towards the ions and to separate among themselves and vice versa. The expression of a punctual particle electrostatic potential is affected and changes from $\phi \approx q/r$ to $\phi \approx q/r \exp -r/\lambda_D$ on a plasma environment, with r the distance from the particle center and λ_D the Debye length defined as:

$$\lambda_D = \sqrt{\frac{kT}{4\pi n e^2}}, \quad (\text{CGS units}) \quad (2.3)$$

where T and n are, respectively, the plasma temperature and density, k the Boltzmann constant, and e the electron charge. This distance is determined by the interplay between the thermal movement of the particles that tends to take them apart, and the electrical interaction that tends to keep charges of opposite sign together. It can be derived from the shielded electrostatic potential that at one Debye length distance from the isolated charge the value of the potential will drop to $1/e$, 0.37, of the un-screened value. As a consequence an electrostatic potential generated by any plasma

charge will be sensed mainly inside a sphere of radius λ_D centered on the charge. This effect is named *Debye screening* or *shielding*, in reference to the fact that at distances greater than the Debye length the electrostatic potential loses its strength.

2.1.4 The plasma parameter

The number of plasma particles inside a sphere having a radius equal to the Debye length is the quantity that defines the plasma parameter, which is inversely proportional to them ($4/3 \pi \lambda_D^3 n$) and defined as:

$$g = \frac{1}{n \lambda_D^3}, \quad (2.4)$$

with n the density of plasma particles, and reflects the strength of the Debye shielding. If the plasma parameter is large then just a small number of plasma particles are inside the Debye sphere and the shielding is low. Thus the electrical interaction between plasma particles becomes more effective over longer distances. The ratio of the mean interparticle potential to the mean kinetic energy is proportional to the plasma parameter. The mean kinetic energy is given by:

$$\langle E_k \rangle = \frac{1}{2} m \langle v^2 \rangle \propto n \lambda_D^2,$$

and the mean interparticle potential energy is:

$$\langle E_p \rangle = -\frac{e^3}{8\pi} \left(\frac{\bar{Z}}{\epsilon_0} \right)^{3/2} \sqrt{\frac{n}{T}} \propto \frac{\bar{Z}^{3/2}}{\lambda_D},$$

with \bar{Z} the mean plasma charge. Therefore, we have:

$$\frac{\langle E_p \rangle}{\langle E_k \rangle} \propto \frac{\bar{Z}^{3/2}}{\lambda_D} \propto \frac{1}{n \lambda_D^3} = g. \quad (2.5)$$

When $g \ll 1$ then the mean kinetic energy is much larger than the mean electrostatic energy and the plasma can be understood as an ideal gas of charged particles. To achieve this the plasma should have either low density or high temperature or a combination of both, as the plasma parameter can also be expressed as:

$$g = \frac{1}{n \lambda_D^3} \propto \frac{\sqrt{n}}{T^{3/2}}.$$

If many plasma particles enter on the sphere the electrostatic potential will affect stronger the plasma particles.

2.1.5 Particle motion in magnetic fields

Despite the collective nature of plasmas, some properties can be understood by observing single particles. The plasma motion due to electromagnetic fields, external or self-generated, is one of these properties. If there is a static and homogeneous magnetic field \mathbf{B} , the motion of a single charged particle will follow a helical trajectory with its axis along the magnetic lines. This movement can be decomposed in two independent ones, an accelerated straight line and a rotation around this line caused by the magnetic field. The rotation frequency for an electron is given by:

$$\omega_c = \frac{eB}{m_e c}, \quad (\text{CGS units}) \quad (2.6)$$

and it is known as the cyclotron frequency. Here, e is the electron charge, m_e the electron mass, B the value of the magnetic field, and c is the light speed.

Magnetic pressure

A magnetic field \mathbf{B} exerts a force per surface unit perpendicular to the magnetic flux direction equal to $B^2/8\pi$ dynes/cm². A plasma is diamagnetic, so it excludes any external magnetic field from the volume that it occupies. Thus, at the magnetic field boundary the magnetic pressure balances the combined electron and ion kinetic pressures $n_e kT_e + n_i kT_i$ as reflected by the β or ratio of magnetic to kinetic pressure:

$$\beta = \frac{n_e kT_e + n_i kT_i}{B^2/8\pi}. \quad (2.7)$$

This parameter indicates the possibility of magnetic compression. If $\beta > 1$ then the kinetic pressure overcomes the magnetic compression and the plasma will expand and decrease its temperature and density. And the opposite also happens: if $\beta < 1$ then the magnetic pressure is able to compress and heat the plasma. This is the physical process underlying the Tokamak design: a magnetic confinement with $\beta = 1$. But in practice the confinement provided by the magnetic field is inherently unstable. Z-pinch machines produce an effective plasma compression as in these devices β is smaller than unity.

2.1.6 Plasma frequency

This frequency is associated with collective motion of charged particles in the plasma, taking place for the neutralization of macroscopic ion charge fluctuations. Given that the electron thermal velocity can be expressed as: $C_s = \sqrt{kT_e/m_e}$, and from the defi-

dition of the Debye length, we obtain the expression of the plasma frequency ω_p :

$$C_s = \frac{\lambda_D}{\text{time}} \Rightarrow C_s^2 = \left(\frac{\lambda_D}{\text{time}} \right)^2,$$

$$\frac{kT_e}{m_e} = \frac{4\pi n_e e^2}{\text{time}^2}, \quad (2.8)$$

$$\frac{1}{\text{time}} \equiv \omega_p = \sqrt{\frac{4\pi n_e e^2}{m_e}}. \quad (\text{CGS units})$$

2.1.7 Critical density

The dispersion equation for electromagnetic waves in a homogeneous plasma can be written as $k^2 = (\omega^2 - \omega_p^2)/c^2$. Thus electromagnetic waves with a frequency bigger than ω_p will propagate into the plasma, the ones with a frequency equal to ω_p will be reflected back, and when the waves' frequency is smaller than ω_p , the electromagnetic waves will become evanescent and they will not propagate into the plasma. The plasma density for which the incident electromagnetic wave with a given wavelength is reflected is known as critical density [12]. The *nhelix* laser is a Nd-YAG laser with a wavelength of 1.064 micrometers, thus the corresponding critical density is $9.8 \cdot 10^{20} \text{ cm}^{-3}$, consequently the *nhelix* laser beam will not propagate into plasma with higher densities.

2.1.8 Radiative processes in plasmas

Photons are emitted and absorbed in a plasma mainly as a result of changes in the electronic states of the plasma species¹ together with the interaction of ions with free electrons. Emission and absorption of electromagnetic radiation can be grouped within three categories: bound-bound, bound-free and free-free transitions depending on the energetic levels which are involved.

Electronic transitions between defined electronic levels within a plasma species are called bound-bound processes. If one electron inside an excited ion relaxes its state and goes to lower energetic levels, energy is freed in the form of a photon. The inverse is also possible, and electrons inside an ion can be excited by the absorption of a photon of energy at least equal to the difference between the levels. The emitted radiation is unique to each element due to the variation of the electronic levels between the elements, so the emitted bound-bound or discrete spectrum can be used to identify a chemical element.

¹Plasma species' means in this context molecules, atoms and ions.

When the absorbed photon energy exceeds the electron binding energy the electron is freed from the ionic attraction with a kinetic energy equal to the photon energy minus the electron binding energy, leaving a higher charged ion. This ionization mechanism is named photoionization and its a bound-free process, like the reverse transition called photorecombination: the capture of a free electron by an ion accompanied by photon emission. As photoionization and photorecombination processes involve free states of the electron being absorbed or emitted, the correspondent photon spectrum is continuous.

Free-free transitions are the ones that involve free electrons of the plasma being accelerated by the electric field of ions. During this process photons with a continuous spectrum are emitted and the corresponding radiation is called Bremsstrahlung. Another emission process is the Plank or black body radiation, where photons have a continuous spectrum that follows the main temperature of the emitting body.

Section 2.2 Plasma generation

Plasma is the most abundant state of matter in the universe, being up to 99% of the observed matter [13]. From the coronal stars to the upper atmosphere of the Earth, nature presents a large variety of plasma types. Many analytical plasma models rely on a group of assumptions named ‘coronal mode’ which is characterized by a low density, of the order of 10^{10} cm^{-3} , and temperatures of the order of 100 eV. These are just the sun corona conditions, hence the name. Many other natural plasmas have these coronal mode conditions, like the Earth ionosphere, the solar wind, and the gaseous planet atmospheres up to a certain depth [14], [15].

One of the largest plasma sources in the universe are the stars. They expel plasma as a result of inner processes like the solar flares [16]. Other astronomical objects produce collimated plasma flows of different kinds. They are generally called plasma jets because of collimation and velocity [17]. The study of these natural plasmas is rather difficult if possible, but plasmas can be also produced in laboratories under controlled conditions [18]. Moreover, artificially produced plasmas have numerous industrial applications [19].

2.2.1 Artificial plasmas

The artificial generation of plasmas started in the 1920’s with the generation of gas discharges. Nowadays the plasmas in a wide range of parameters are produced using numerous different approaches as detailed in the following parts of the section.

Low-pressure cold-cathode discharges

In a sealed vessel with low pressure gas a plasma with low density ($n \approx 10^{10} \text{ cm}^{-3}$) and temperature ($T_e < 0.5 \text{ eV}$) can be created by a continuous or pulsed electrical discharge between the electrodes placed inside. The electrical current passes through the gas, heating it and generating the plasma. The total current passing through the device must be limited due to the 'negative resistance' of the plasma. Electrons emitted from the cathode are very soon absorbed by the gas leading to an absorption of the current measured from outside the vessel, so the external resistance of the system is 'negative'. Glow discharges, as this kind of discharges is also frequently named, are used in the panel lights. There the visible light is obtained either by the phosphorescent cover of the inner tube wall, that glows excited by the ultraviolet light created by the plasma or by the self emission from the gas at a certain wavelength in the visible bandwidth.

Arc discharge

Higher plasma densities ($n \approx 10^{13} \text{ cm}^{-3}$) can be achieved by a slight modification of the cold-cathode discharge device. If the cathode is coated with an oxide, the number of emitted electrons is increased by cathode heating [20]. The increase in the number of electrons permits the generation of plasmas with higher densities. Since the plasma density is proportional to the electric current, it can be controlled and tuned to the desired value. Currently arc discharges are of interest for the industry as plasma generators for many different purposes

Plasma guns

A plasma gun is a device where an accelerated plasma is produced [21]. Electrodes in a coaxial configuration, one cylinder surrounding the central solid bar, are fired from a capacitor bank with large current values. In this moment a small quantity of ions is allowed to enter in the central part of the coaxial geometry. As the voltage between the electrodes is larger than the gas breakdown, the gas is ionized and converted in a plasma with the remained electrons. The current between the electrodes accelerates the plasma and produces a ring shaped current sheath. This is magnetized by a radial magnetic field that helps to maintain its shape for relatively long times, of the order of μs , and distances of approximately 1 m.

Alkali metal vapor plasma—Q machines

With the development of plasma studies for fusion purposes, one of the main concerns are plasma instabilities. It is still a big area of research, since considerable part of the energy given to the plasma is lost in the generation and maintenance of these instabilities. The Q machine was supposed to solve the instability problem, as the

produced plasma was thought to be stable in comparison with the one produced by discharges or other means [22]. However, low frequency instabilities were also in this case unavoidable, thus Q-machines are today just of academic interest.

The working principle is simple. Under vacuum conditions the heated plate of a metal with high boiling point is bombarded with neutral atoms of a much lighter element. The neutral atoms transfer electrons to the heated area and are repelled as ions from it. At the same time, the heated plate generates thermionic electrons because of its high temperature. The mixture of these electrons and the light element ions creates the plasma. Opposite to this plate a cooled plate may be placed resulting in a single ended Q machine. If this plate is also heated, the ion and electron streams are reflected there, and the plate is a second plasma source. The device is then a double ended Q machine.

Radio frequency produced plasmas

When a gas is excited by an intense oscillating electromagnetic field, the gas molecules are broken and ionized producing a plasma. Typically, radio frequency (RF) waves are used, so the produced plasmas are called RF plasmas. This plasma generation technique has certain advantages. The plasma vessel does not need inner electrodes, since the RF waves can pass through the dielectric vessel wall. The obtained electron densities are on the order of 10^{10} cm^{-3} but can be made higher with the application of an oscillating electromagnetic field. If the field frequency is nearly the cyclotron resonant frequency, plasma temperatures in the 20 keV range are obtained.

Tokamak plasmas

Tokamak devices are able to create very hot and relatively long-lived plasmas with the aim of fusion energy. A Tokamak is a vacuum toroidal shaped device. Its vessel is surrounded by very intense magnetic fields that mimic the toroidal shape of the wall by the use of adequate magnets. The plasma is initiated by external means, like radio frequency. After the plasma is created, its own rotation inside the magnetic field and the diamagnetic plasma properties help to confine and compress the original plasma.

Z-pinch plasmas

Z-pinch machines produce plasmas using high voltage pulses applied to a pair of electrodes in a cylindrical geometry. The cylinder is either pre-filled with a gas or made using a wire array (usually of high-Z metals like tungsten). Once the electric discharge is initiated, the plasma implodes by the magnetic pressure of the azimuthal magnetic field created by the axial current. Due to this initial implosion, at the stagnation stage of the plasma a hot and dense core is formed at the axis of the discharge with electron temperatures in the range of 0.1 to 1 keV. When the plasma reaches this point it is very unstable, and it finally expands and cools.

2.2.2 Laser created plasmas

Laser light can also produce plasmas provided that the laser flux is high enough. The electromagnetic wave emitted by the laser interacts with matter through their electrons. Initially free electrons from the target material absorb energy from the laser electromagnetic field and transfer it through collisions thus increasing the ionization degree and temperature of the irradiated sample. Finally a plasma is formed.

Two aspects of plasma generation by lasers are more closely considered in the following sections. One is laser light absorption by the plasma and the other is plasma expansion. A quasi-steady state situation is assumed, due to the long duration of the laser pulse used in the experiments.

Laser light absorption

Plasma generation by laser radiation applied on solid targets is mainly a surface phenomenon, in the sense that the typical dimensions of the absorption length are orders of magnitude smaller than the target dimensions. The main mechanism of light absorption for laser fluxes from 10^{10} to 10^{14} W/cm² is inverse bremsstrahlung. The laser photons are absorbed by the target free electrons and give them their energy. They collide with the bound electrons of the target atoms, becoming then ions. Due to the electron–ion collisions the ions are excited and removed from the target, ablating it.

The laser light can also be absorbed by resonant absorption, studied by its relation with electrons at energies far off from the thermal kinetic energy values. When the laser light reaches the critical density region, its frequency is equal to the local plasma frequency. Resonance coupling between the laser light and the plasma can then happen if the wave vector and the electric field are parallel, and plasma electrons can be accelerated to very high energies [23]. It is an angle dependent process that demands a laser beam entering at an angle different of 0° with respect to the target surface. However it is claimed that with a laser beam with a normal incidence to the target surface, 0° incident angle, and short focus distances due to the high $f/\#^2$, the part of the laser beam parallel to the target surface could produce resonant absorption [24].

The simple scheme shown here is far from completion. The study of the energy absorption from laser radiation and instabilities on plasmas is still a very active area of development in physics [25]. One of the reasons is their importance in the energy transfer in the laser fusion scenario [26].

²The f number or $f/\#$, also called aperture ratio, denotes the ratio of the equivalent length of one lens to the aperture of the lens pupil.

Quasi-steady plasma state

Stationary or quasi-steady plasma state happens when the temporal changes are smooth enough to separate the laser wave, therefore the total problem, in two parts. One with a time variation equal to zero in a first order approximation and the other a fast varying part oscillating at the laser frequency, as it is made in [27] to study the magnetic field generation by plasmas. The time necessary to reach the quasi-steady state for the supercritical plasma, plasma with an electron density higher than the critical can be expressed as [28]:

$$t_0 \cong 7 \left(\frac{I_a}{10^{14} \text{W/cm}^{-3}} \right) \left(\frac{\lambda_l}{1 \mu\text{m}} \right)^4 \left(\frac{A}{2Z} \right)^{3/2} \text{ ns}, \quad (2.9)$$

where I_a is the absorbed flux, λ_l the laser wavelength, A the atomic number, and Z the mean ionic charge of the target material. Within the experimental conditions obtained with the *nhelix* laser this time is on the order of $t_0 \approx 1$ ns and the *nhelix* temporal Full Width Half Maximum (FWHM) is 16 ns. These numbers mean that the plasma created in these experiments was in a quasi-stationary state during the pulse duration.

Plasma expansion

Plasma characteristics like the electron temperature, electron density, and the plasma expansion depend on the incident laser flux. Using the quantity $\phi \lambda_l^2$ as parameter, with ϕ the laser flux in W/cm^2 and λ_l the laser wavelength in μm , scaling laws for the kinetic energy of the ions and electrons and their quantities have been found from numerous experimental results [5].

Other laws for the electron temperature and density with a flux value have threshold flux values that indicate the change between different scaling regimes. The threshold flux value can be expressed as:

$$\phi_{th} = 1.5 \cdot 10^{-21} \frac{(1+Z)^{3/2}}{\sqrt{A}} n_c^2 r, \quad \text{W/cm}^2 \quad (2.10)$$

with A and Z the average ionic mass and charge in atomic units, n_c the critical density defined in 2.1.7 and r the laser spot radius [29]. For a laser flux above the threshold value the electronic temperature scales as $T_e \approx r^{2/9} \phi^{4/9}$, and below it the scaling law changes to $T_e \approx \phi^{2/3}$. With the *nhelix* parameters given in section 3.1 on page 33 and a typical mean ionic charge of 10 valid for the magnesium targets employed in the experiments, this flux is $\approx 10^{21} \text{ W/cm}^2$, so the plasmas presented in this work follow the scaling law of $T_e \approx \phi^{2/3}$.

The models for plasma expansion in vacuum relay on a quasi-steady situation, in which the plasma is formed and it has well defined electron density and temperature

profiles [30]. These profiles have a certain dependence on the expansion model of the plasma zone with electron density under the critical value, the so-called subcritical region. The variation is not very high, but nevertheless differences exist between the profiles for isothermal or adiabatic plasmas in the subcritical region [31]. The plasma created in the experiments performed during this work did not fulfill the conditions to be isothermal, so deviations from this kind of profile can be expected. To match the isothermal expansion of the subcritical region, the flux absorbed by the plasma should comply with:

$$I_a \geq 5 \cdot 10^{12} \tau_L \left(\frac{1}{\lambda_l} \right)^4 \left(\frac{2Z}{A} \right)^{3/2} \text{ W/cm}^2 \quad (2.11)$$

were τ_L is the laser pulse duration in ns, λ_l is the laser wavelength in μm , Z is the mean ion charge, and A the atomic weight in a.m.u. Using the *nhelix* laser parameters and an average magnesium ion charge of 10, this value is $5 \cdot 10^{13} \text{ W/cm}^2$, like the measured fluxes values, and the condition for isothermal expansion of the plasma is not fulfilled.

The initial quasi-stationary vacuum plasma state is modified by the dynamics of its components [32]. The electrons move faster from the plasma than the heavier ions. This motion creates very intense electric fields that push the ions in the electron direction, creating an ion density front wave and a rarefaction wave in the opposite direction. The waves from the electron front, the ion front and the rarefaction wave define three regions within the plasma expansion:

- I A pure electron gas ahead of the ion front,
- II an expansion region with similar electron and ion densities between the ion front and the rarefaction wave and
- III an unperturbed plasma behind the rarefaction wave.

The propagation velocity of the rarefaction wave is of the order of the ion sound velocity, while the electron density of the expansion region follows an exponential decay. Due to its use in laser pulsed vapour deposition, the geometry of the laser plasmas was intensively studied for low fluxes of the order of 10^8 to 10^{10} W/cm^2 . The plasma expansion from a planar slab has privileged directions. The expansion in the direction perpendicular to the target surface is stronger than in any other direction [33]. The particle distribution from the plasma follows a Gaussian distribution with the main dependence on the emission angle [34], α :

$$\text{Ion angular distribution} = \frac{1}{\sigma\sqrt{2\pi}} \cdot e^{(\alpha-\epsilon)^2/2\sigma^2}. \quad (2.12)$$

The width has been analytically fitted [34] so that in the previous expression it is $2\sigma = C1/A + C2$, with the parameters $C1 = 1115$ and $C2 = 34.8$ respectively, allowing its prediction for many different materials. A is the atomic mass of the target material in a.m.u.

External factors can affect plasma expansion. With the presence of static magnetic fields, for instance, the expansion symmetry mentioned in the previous paragraph is altered and the expansion plume is divided in two parts, with their shape depending on the laser focus position with respect to the magnetic field [35]. The plasma X ray emission increases in the presence of a magnetic field, that is related to the magnetic confinement [36].

The plasma is rarely a monoionic fluid, and many ionic species may be present. The ionic abundance can be approximated with the help of collisional radiative models [37] which state that the relative ionic abundance has a strong dependence on the electron density and temperature. The ion dynamics depend also on the ion kind, each ion species having a different spatial and temporal distribution within the plasma plume: the angular distribution narrows for higher charge states [38].

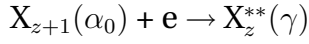
Magnetic field generation in laser created plasmas

The generation of magnetic fields in plasmas was demonstrated from the beginning of studies on laser created plasmas [39]. With laser fluxes of 10^{15}W/cm^2 and pulses of a few nanoseconds, Megagauss fields were obtained [4]. Magnetic fields were also obtained with picosecond lasers [40]. To generate such magnetic fields, the plasma should produce electric currents of the order of 10^4 A [41].

Section 2.3 Introduction to spectroscopic plasma parameters diagnostics

Dielectronic satellites are formed by spontaneous photon emissions from doubly excited ions and they are an important diagnostic tool [42], [43]. The dielectronic satellites have wavelengths near the resonant transitions. The satellites to the H-like resonant line $2p - 1s$ are the transitions $2pnl - 1s nl'$ in He-like ions. The transitions $1s2pnl - 1s^2 nl'$ from Li-like ions are the satellites to the He-like resonant line $1s2p - 1s^2$. Starting with carbon their wavelengths belong to the X ray range. The main dependences of their intensity are from the plasma electron density and temperature and this feature is used in the plasma diagnostics.

Dielectronic capture and inner-shell excitation are the two main ways to generate these lines [44]. The dielectronic capture is the process which takes place when the capture of an electron is possible at energies lower than the excitation threshold for the resonant line. In this case the ion passes to a doubly excited state of lower charge:



where X is the ion, z is its charge state, α_0 is the ion initial state, and γ the final double excited state of the lower charged ion. This final state is unstable, having the total energy above the ionization limit and it decays either through autoionization or by spontaneous emission of a photon. The latter is the dielectronic recombination.

Another way to create double excited states is the inner-shell excitation of excited ionic levels, when an electron is excited without alteration of the charge state. The efficiency of inner-shell excitation is smaller than that of dielectronic capture, thus this mechanism is neglected for the estimation of the satellite intensity.

The figure 2.1 is a simplified scheme of the levels for the three charged states of H-, He-, and Li-like ions with the resonant(w) and intercombination(y) transitions with some important satellites(j, a, k)

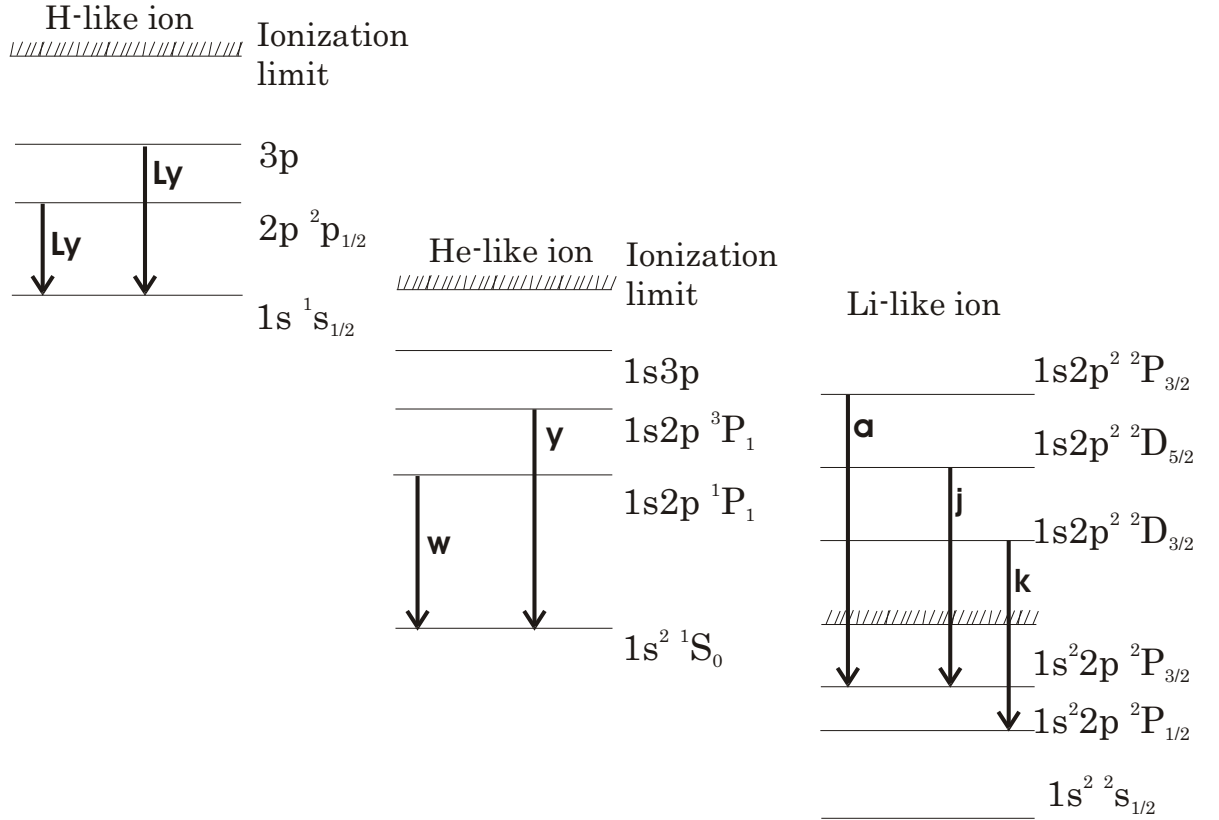


Figure 2.1: Levels with the satellite (**a**, **j**, **k**), resonance (**w**), and intercombination(**y**) transitions for the three first charged states.

The ratio of the satellite line to the resonant line intensity has a strong dependence on electronic temperature. Thus by measuring this ratio one may estimate the electron temperature [45]. The intensity of the dielectronic capture satellite can be expressed for He-like transitions as:

$$I_{Sat} = n_{He} n_e \frac{4\pi^{3/2} a_0^3}{T_e^{3/2}} \frac{g_{Sat}}{g_1} A_r \frac{A_a}{A_a + \sum A_r} \exp(-E_s/T_e), \quad (2.13)$$

where n_{He} is the relative abundance of He-like ions, n_e the electronic density, a_o the Bohr radius, g_{Sat} and g_1 the statical weights of the satellite and ground resonant levels, A_a and A_r the autoionization and radiative transition probabilities. E_s is the energy from the Li-like satellite excited to the He-like ion ground level and T_e the electronic temperature. Within the coronal model, the intensity of the resonant line $1s2p - 1s^2$ can be written:

$$I_{Res} = n_{He} n_e C (1 + \alpha), \quad (2.14)$$

where α is a parameter that counts for satellite transitions not considered here but with wavelength close enough to the resonant line, mainly $1s3l - 1s^2$ and higher n , and C is the impact excitation rate coefficient, that according to the Van Regemorter formula [46] can be written:

$$C = 8 \sqrt{\frac{\pi}{3}} \frac{h a_o}{m_e} \frac{f}{E_0 T_e^{1/2}} P \exp(-E_0/T_e), \quad (2.15)$$

where E_0 is the energy of the resonant line, $h\nu$, P an effective Gaunt factor of 0.2, and f the oscillator strength. Substituting it in eq. 2.14, one finally obtains:

$$I_{Res} = n_{He} n_e 8 \sqrt{\frac{\pi}{3}} \frac{h a_o}{m_e} \frac{f}{E_0 T_e^{1/2}} P \exp(-E_0/T_e). \quad (2.16)$$

The ratio of the satellite line to the resonant line intensities is then:

$$\frac{I_{Sat}}{I_{Res}} = \frac{\pi a_o^2 \sqrt{3} m_e}{2 \cdot 0.2 h} \frac{g_{Sat} E_0}{g_1 f T_e} \frac{1}{1 + \alpha} A_r \frac{A_a}{A_a + \sum A_r} \exp\left(\frac{E_0 - E_s}{T_e}\right). \quad (2.17)$$

With adequate numerical substitutions for the satellite between the levels $1s2p^2 \ ^2D_{5/2}$ and $1s^2 2p \ ^2P_{3/2}$, denoted by j in Fig. 2.1, and the corresponding resonant line one obtains for magnesium ions:

$$\frac{I_{Sat}}{I_{Res}} = \frac{5.104}{T_e} \exp\left(\frac{391.23}{T_e}\right), \quad (2.18)$$

with electron temperature T_e in eV.

One important plasma parameter related to the electromagnetic wave emission is the optical thickness of the lines,³ Photon emission takes place inside the plasma, thus they can be reabsorbed with the final result of a reduction in the detected intensity for each specific transition. This process depends on the plasma size and density and on photon energy. The reemission probability must also be taken into account in the calculation of the optical thickness:

³Capability of the emitted photons to pass through the medium and arrive at the detector

$$\tau_0 = 1.25 \cdot 10^{-40} \left(\frac{\lambda \cdot 0.1}{\text{nm}} \right)^3 \left(\frac{g_u}{g_d} \right) A_{line} \left(\frac{\lambda}{\Delta\lambda} \right) \left(\frac{n_l}{\text{cm}^{-3}} \right) \left(\frac{L_{eff}}{\mu\text{m}} \right), \quad (2.19)$$

with $\lambda/\Delta\lambda$ the intrinsic FWHM of the emitted line, A_{line} the radiative decay probability, g_u and g_d the statistical weights of the upper and lower levels of the transition, L_{eff} the effective plasma dimension, and n_l the absorbing ground state density. Considering typical plasma parameters for experiments performed within this work, a plasma size of 0.5 mm and n_l approximately 10^{17} cm^{-3} the optical thickness for the j satellite and the He-like resonant line were calculated, see Table 2.1

| Line name | Radiative decay (s^{-1}) | λ (\AA) | $\Delta\lambda$ (\AA) | g_u | g_d | Opt. thickness |
|-----------|-------------------------------------|----------------------------|----------------------------------|-------|-------|----------------|
| w | $1.97 \cdot 10^{13}$ | 9.1697 | $7 \cdot 10^{-3}$ | 3 | 1 | 0.373 |
| j | $9.23 \cdot 10^{12}$ | 9.3206 | $9 \cdot 10^{-3}$ | 6 | 4 | 0.075 |

Table 2.1: Optical thickness of some lines.

From these data it is clear that the transmission of the resonant line in the plasma will be lower than the satellite line j , so the ratio of j to w emission lines will underestimate the electron temperature. When the optical density is taken into account, the intensity of a line is altered as follows:

$$I_{Sat}^{OD} = \frac{I_{Sat}}{1 + \tau_S}$$

with τ_S the optical density of the line, I_{Sat}^{OD} the measured value and I_{Sat} the real one. Considering values of Table 2.1, underestimation of the electron temperature is low and no need of correction for the measured values is considered.

Chapter 3

Experimental setup and techniques

This chapter describes the setup and devices employed in the experiments. The *nhelix* laser system is described first, including the diagnostic methods employed to characterize the laser beam. The plasma diagnostic devices are presented in the next section and are classified according to the working wavelength range. During the experiments two different setups were used, differing from each other through the positioning of diagnostic devices and the laser-target geometry. These are described in the last section.

Section 3.1 The *nhelix* laser system

The name *nhelix* is an acronym of **nanosecond high energy laser for heavy ion experiments**. It is a laser system with two beams. One of them is used for plasma production and the other for the interferometry experiments. The high energy beam described here can deliver up to 120 Joules with a FWHM of 16 ± 2 ns of infrared light at $1.064 \mu\text{m}$ to the target. The laser beam used for the interferometry experiments has up to 3 Joules in 0.5 ns. The frequency is doubled with respect the main beam and corresponds to a wavelength of $0.532 \mu\text{m}$.

3.1.1 The *nhelix* setup

The *nhelix* system is of the master oscillator-pulse amplifier laser type. This means that the low energy pulse delivered by the master oscillator is amplified by the amplifier chain each time that the laser is fired. The amplifiers are solid silica glass rods doped with neodymium, with their diameters increased gradually up to a final value of 64 mm. This is done to maintain the laser flux under the damage threshold value of the glass, that is, to have a laser fluency low enough to avoid the damage on the rod due to the high laser energy concentration in the surface material. The initial master oscillator is a commercial Coherent Powerlite 8 000 Nd:YAG laser with a FWHM of 16 ± 2 ns and a central wavelength of $1.064 \mu\text{m}$. The output energy is approximately 180 mJ.

The initial transverse shape of the laser beam is elliptical. In order to couple the

laser to the circular amplifier rods, a cylindrical lens telescopic system is used. Figure 3.1 shows the initial elliptical intensity shape and the circular output after the telescope.

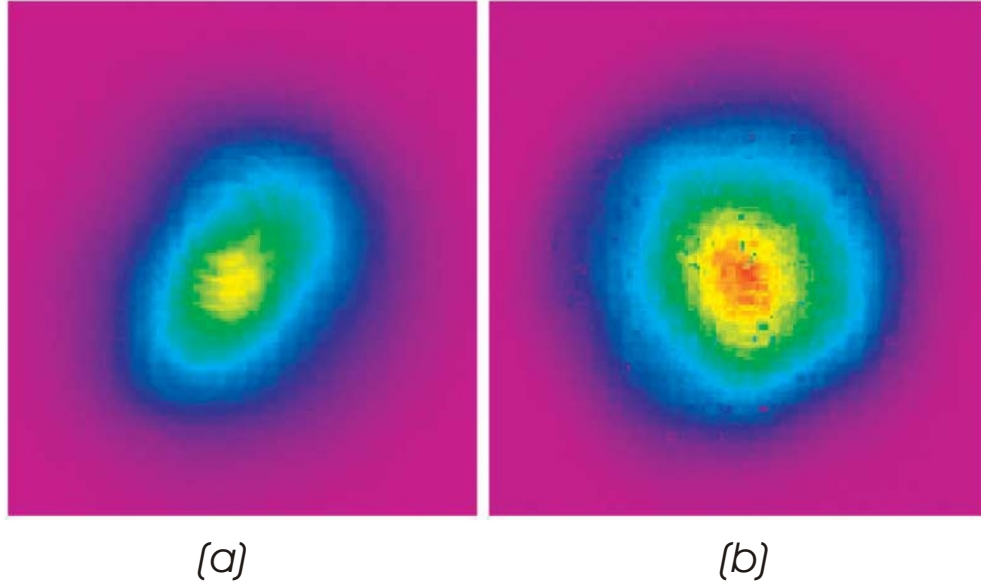


Figure 3.1: Transverse beam shape (a) before and (b) after the telescope. Adapted from [47]

After transverse shape correction, two amplification stages follow. Each one has a spatial filter followed by a rod amplifier. The spatial filters are telescopes composed of two plane-concave lenses at the common focal distance and a central metallic pinhole at the common focus. Due to the spatial properties of the lenses, frequencies below or above the central laser frequency are focused away from the pinhole, being filtered as the laser beam passes through the pinhole. Thus the output of the spatial filter is a laser beam with a cleaned spatial frequency spectrum, necessary to improve the beam properties and the laser focus diameter. The rod amplifiers are pumped by flash lamps.

After passing these two stages the laser beam is reshaped with a **soft polarizing aperture (SPA)** system. This system is composed of a birefringent plane-convex lens, a plane-concave BK-7 lens, and a thin film polarizer. The linear polarization of the incident beam is rotated according to the thickness of the birefringent lens. Taking into account the polarizer, the power transmission of the SPA can be written as a function of the radius:

$$T(r) = \cos\left(\frac{1}{2}\Delta n \frac{\pi r^2}{\lambda R}\right), \quad (3.1)$$

where $\Delta n = 0.009$ is the difference between the refractive index of the ordinary and the extraordinary waves, λ is the laser wavelength, $R = 1197$ mm is the radius of

curvature of the birefringent lens, with $r_0 \approx 12$ mm as zero transmission radius value, dependent on Δn , λ and R . The laser beam transmission is then larger in the center, where the amplification of the rods is smaller, see Fig. 3.1.1. Thus the SPA shape transmission compensates the differences in amplification due to the geometry of the amplifiers, making the flux distribution more uniform.

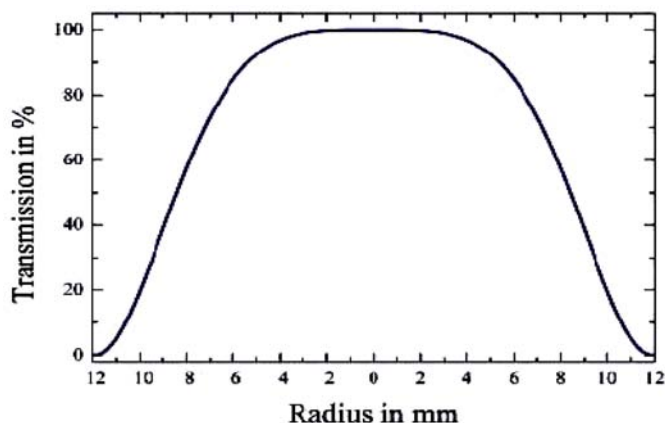


Figure 3.2: Calculated SPA transmission. From [47]

Following the SPA, a Faraday isolator is placed in order to avoid damage produced through backward radiation. The Faraday isolator allows for the transmission of light only in one direction. It is made of three components: an input linear polarizer, a middle Faraday rotator, and a second polarizer orientated 45° with respect to the first polarizer. The linear polarizer is orientated along the direction of the incoming light, that is rotated 45° by the internal Faraday rotator, so the beam passes through the last 45° polarizer. But any reflected light coming from the output of the device will be first polarized to 45° and then rotated to a direction perpendicular to the first polarizer by the Faraday rotator, so that it will not pass through it, effectively isolating the rest of the laser chain from reflected light.

After this Faraday isolator, the laser beam is once again spatially filtered and then amplified in a double pass amplifier. In this amplifier the beam goes two times through the same amplification stage, gaining almost the double energy as compared to single pass amplification. Next step is once again a spatial filter, followed by the last two amplification stages with the spatial filter between them and the mirror which direct the laser beam onto the optical units that divert the laser beam onto the target chamber, as it is depicted in Fig. 3.3.

Inside the target chamber, the last lens of the optical system directs the laser beam to the target surface. The focal length of this lens is 13 cm, and with a pupil size of 5.5 cm, the $f/\#$ of the system is $f/2.4$, a rather low value compared with standard laser facilities with $f/\#$ going from $f/8$ to $f/16.7$. Such low $f/\#$ value could increase the resonant absorption of the laser light because of the larger part of the laser electric field that can be considered to take part in the resonant absorption, even with normal

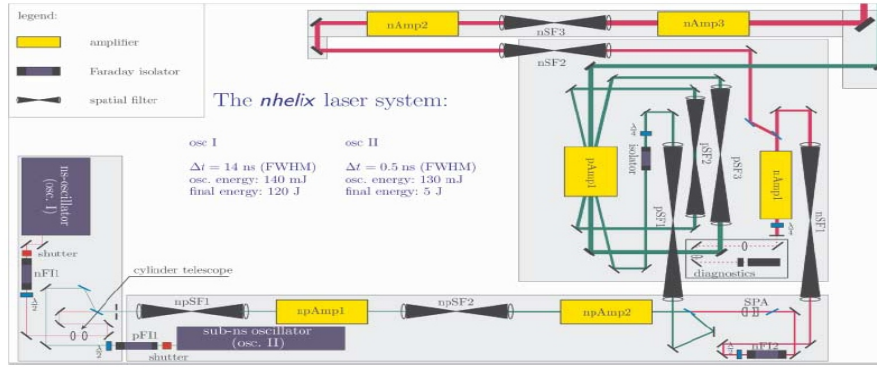


Figure 3.3: Nhelix laser scheme. Adapted from [47]

laser beam incidence.

3.1.2 Laser flux measurements

The laser flux is one of the main parameters that determines the characteristics of the generated plasma. It is defined by:

$$\phi = \frac{E}{t * S}, \quad (3.2)$$

where E is the laser energy in Joules, t is the pulse duration in seconds, and S is the focal spot surface in cm^2 .

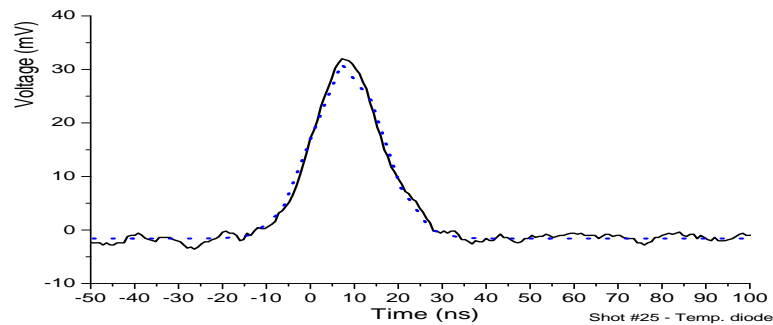


Figure 3.4: Temporal laser profile from the photodiode (—) and the Gaussian fit (.....)

The laser energy was measured in each experiment by a calorimeter. The pulse duration is taken as the FWHM value of the Gaussian time profile acquired with photodiodes (see Fig. 3.4) averaged over many shots. The area of the focal spot is estimated from CCD images of the light profile at the target plane.

Laser pulse temporal profile

In order to estimate the energy flux, an accurate value of the laser pulse duration is necessary. Therefore, a measurement of the temporal laser profile and its variation from shot to shot is very important. A fast photodiode was used in these measurements. The laser light leaking from one of the last mirrors in the laser chain was directed to the diode, where the saturation was avoided in order to eliminate the distortion of the results because of the low quantity of energy passing through the mirror. Figure 3.4 shows a typical result obtained from the photodiode together with the fitted curve which exhibits a Gaussian-like shape. The FWHM of the Gaussian fit is 16 ± 2 ns, obtained as the average value from all the measured profiles. The error of 12.5% is caused by the large variations observed in the temporal profile, linked to the hour of the day that the experiment is made.

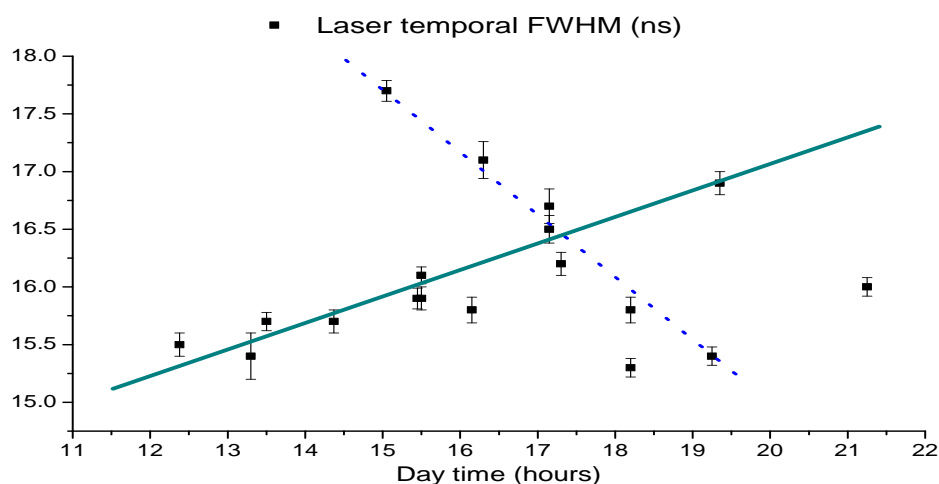


Figure 3.5: FWHM of laser pulse measured with the photodiode as function of the experiment day time

This variation is shown in Fig. 3.5, where two opposite behaviours are visible as represented by the dashed and continuous lines. Limitations of the cooling system of the laser room is the reason for the observed behaviour. The pulse duration increases if the laser system is turned on earlier, and it decreases when it is turned on later, during the evening hours.

Laser energy

The total energy of the laser pulse was measured for each shot because of relatively large shot to shot variations. The laser energy is recorded by a calorimeter positioned at the back of a mirror in the *nhelix* chain.

Light escaped through the mirror is focused by a lens on the calorimeter after, its intensity is reduced with an optical filter of optical density 1 to avoid the calorimeter

sensor head saturation. A lens is necessary to avoid the loss of the external laser profile tails due to its inhomogeneities, that would not fit inside the sensor head surface otherwise.

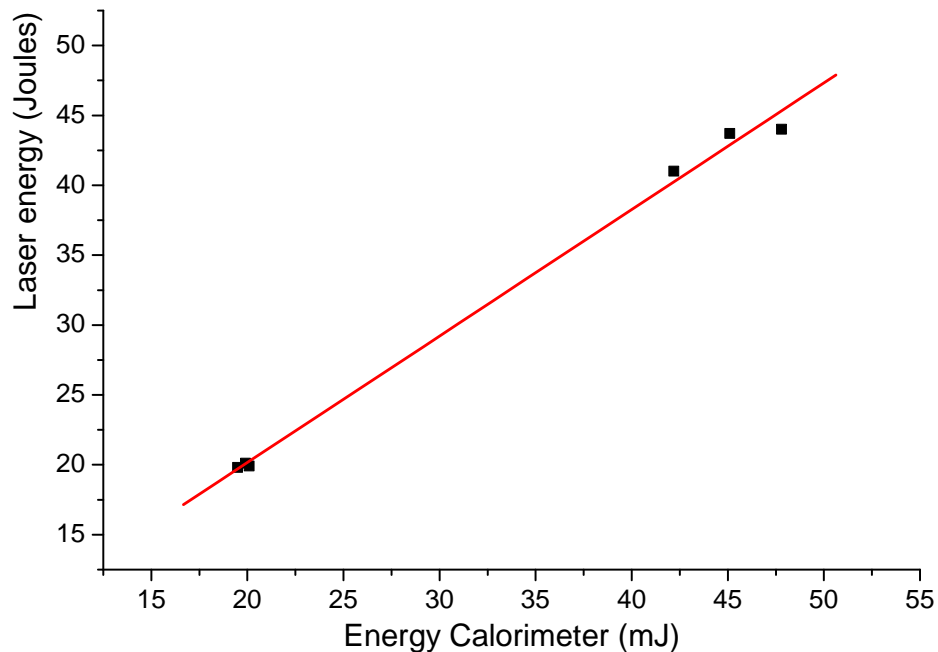


Figure 3.6: Calibration curve for the calorimeter with a normal incidence setup.

The total energy delivered by the laser is much larger than the energy measured by this calorimeter, and a conversion factor between them is necessary. To find out this conversion factor the laser energy was measured by another calorimeter inside the target chamber, thus both values could be compared. The ratio between them is the conversion factor of 1 000, as calculated from the calibration curve on Fig. 3.6.

Focal spot

The focal spot of the laser beam was measured at the target plane and the light distribution as well as the irradiated surface were determined. The focal spot is imaged on a digital camera without any optical system attached to it, so no distortion due to the optical equipment is produced. From the CCD images the light distribution and size of the focal spot can be estimated. The positioning of the *sensing camera* at the desired plane requires a CCD camera called *positioning camera*.

The positioning camera has an objective with a short deep focus¹. The positioning starts by focusing the positioning camera on a glass needle that marks the target position, see (1) in Fig. 3.7.

¹The deep focus is the maximum distance over which the optical system 'can maintain the focusing conditions, therefore the deep focus is a measure of the systems accuracy for distance measurements

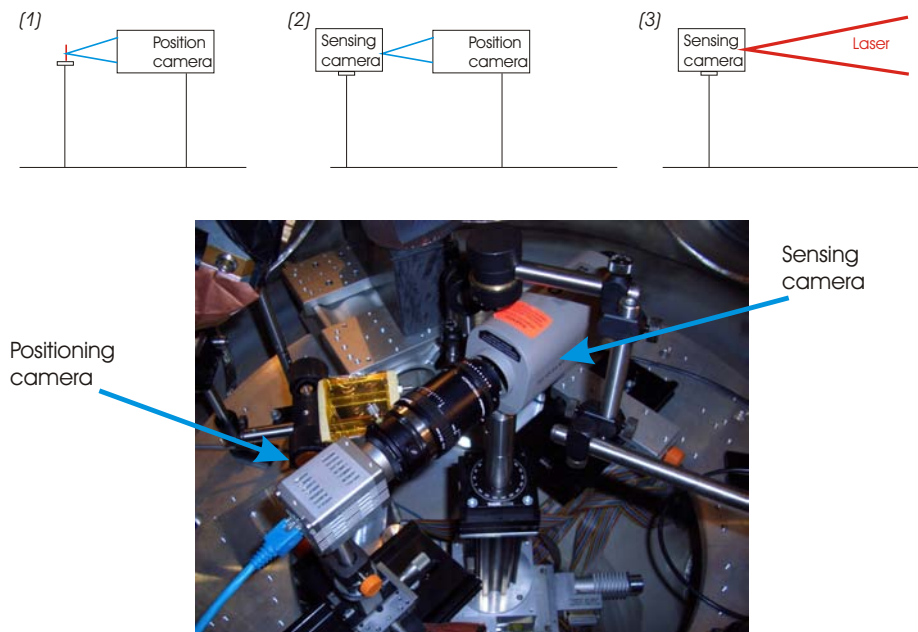


Figure 3.7: Focus measurement procedure scheme. The photo shows the two cameras with the sensing camera focused on the positioning camera.

Once the position of the target surface is fixed by the positioning camera, the needle is removed and the sensing camera is placed there instead such that the CCD plane coincides with the plane imaged by the positioning camera, see (2) in Fig. 3.7. At this point the sensing camera is at the target surface position, thus removing the positioning camera and turning on the laser at minimum energy images the focal spot light intensity distribution on the sensing camera. The laser flux is reduced by a filter with optical density 2, to avoid saturation of the CCD chip.

Figure 3.8 shows the light distribution in the case of a laser beam focused at the target surface. The camera pixel size is $11.5 \times 13.5 \mu\text{m}$. The camera dynamic range is represented by the 1 024 levels of the flux scale. The filter placed between the laser and the camera reduces the total laser flux, diminishing the focal size measured by the camera due to its lack of sensibility in the low energy parts of the distribution.

To find out the value of the correction factor, photosensitive paper sensitive to the laser wavelength was used. The paper surface becomes darker in response to light thus an image of the focal spot surface is created on it. With the help of filters with optical densities 1 and 2, three spot sizes were obtained: one with the laser without any filter, other with the filter at optical density 1 and the last with optical density 2.

The ratio between spot diameters obtained with filters of optical densities 2 and 1 is 1.3 ± 0.3 . The ratio of the diameters resulting from a laser filtered with an optical density of 2 and an unfiltered laser has a value of 4 ± 0.3 . The spots produced without filter in the papers are too big to accurately represent the focal spot, as a result of the very high light intensity that burns the paper in regions outside of the laser spot sur-

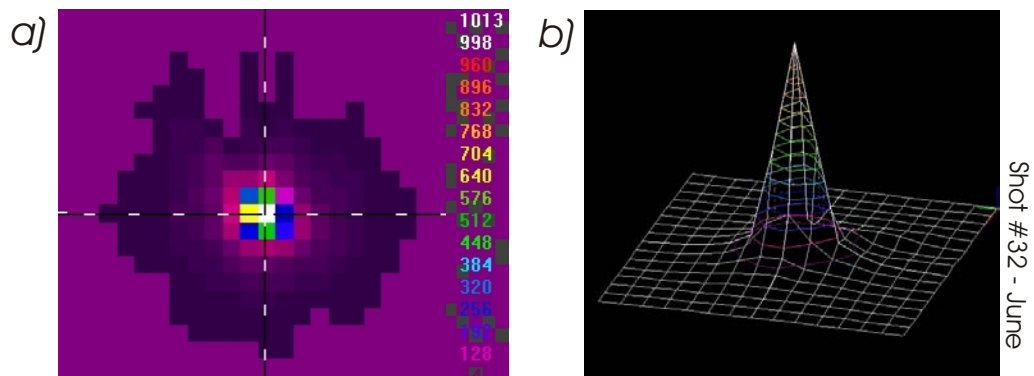


Figure 3.8: *a)* 2-D and *b)* 3-D images of the focus of the target surface.

face. A correction factor of two is taken as a compromise to adjust the value obtained by the CCD camera.

Section 3.2 Plasma Diagnostics

The diagnostic tools used during the experiments were light sensors for different bandwidths, so the plasma properties are not altered by them as there is no contact between the plasma and the sensors. The radiation spectrum emitted from a body can be related to its temperature, and has a maximum emission wavelength that depends on the temperature. Different temperatures are achieved at different plasma stages. Both the hot and the cold plasma parts are measured from emitted X ray and visible radiation. The use of spectrographic methods in the ultraviolet and X ray range allows for the qualitative, if not quantitative, study of the plasma electron temperature. Images obtained with X ray pinhole and visible streak cameras provide data about the plasma spatial features, as related to the irradiation conditions.

3.2.1 Pinhole cameras

The pinhole camera or camera obscura is a well known device. Two-dimensional (2D) images in the X ray range were obtained with appropriate filters and films, and they were used to determine the geometry of the plasma expansion, integrated over time. Measurements of the length of the expansion in a direction perpendicular to the target surface were done. Its angular spread was also estimated from the angular distribution of the recorded X ray emission.

Working principle of pinhole cameras

The pinhole camera is based on the properties of light propagation. When the dimensions of the optical system are much bigger than the wavelength, the paraxial approximation for light propagation is valid. Thus light propagates along straight

lines in any homogeneous media.

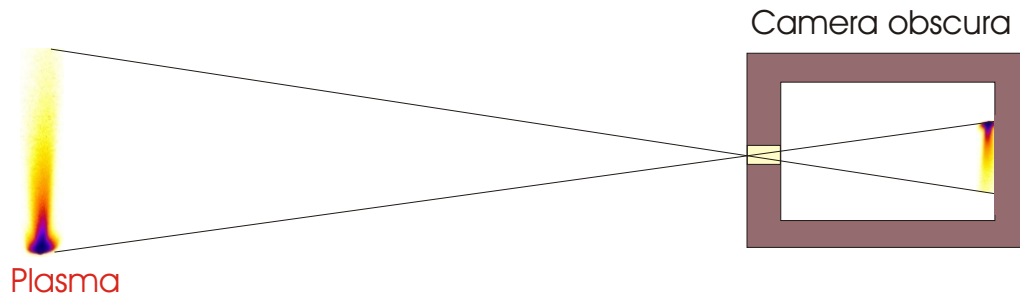


Figure 3.9: Pinhole camera working principle

In a closed box with a hole larger than the light wavelength but small in comparison with the dimensions of the system to be imaged, only light rays that travel in a straight line from the emitter and through the hole can arrive at the back of the box. An inverted 2D-image of the object is then formed on this wall, see Fig. 3.9 .

Figure 3.10 shows the X ray plasma expansion recorded with the pinhole camera and a PP filter with the plasma expansion clearly visible. The laser beam was perpendicular to the target surface and in a direction opposite to the shown expansion.

The image has a scale factor with respect to the original object called magnification. It is the ratio between the distances from the object to the pinhole (d_o) and from the pinhole to the image (d_i):

$$M = \frac{d_i}{d_o} \quad (3.3)$$

If d_o is bigger than d_i then the image is smaller than the object and the magnification is smaller than one.

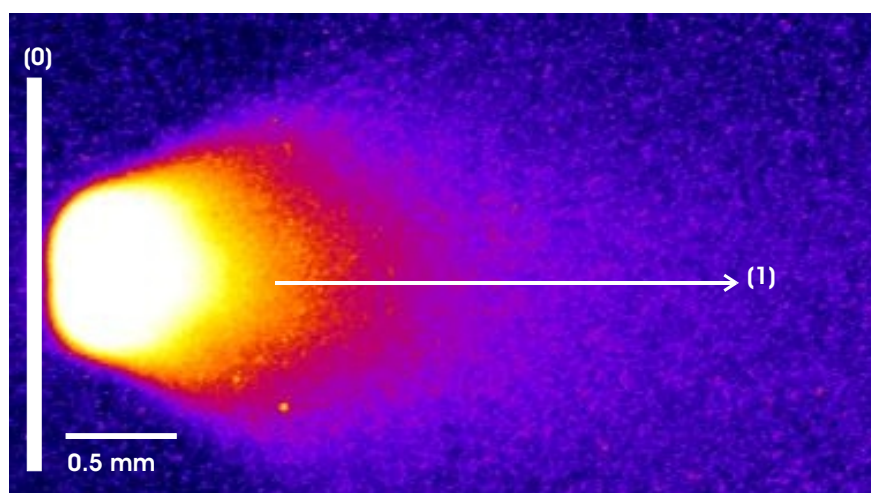


Figure 3.10: X ray plasma expansion recorded with a pinhole camera and the PP filter. (0) Original target surface position and (1) plasma expansion.

X ray pinhole camera characteristics

The pinhole diameters were 80, 150 and 180 micrometers thus no smaller structures could be visualised.

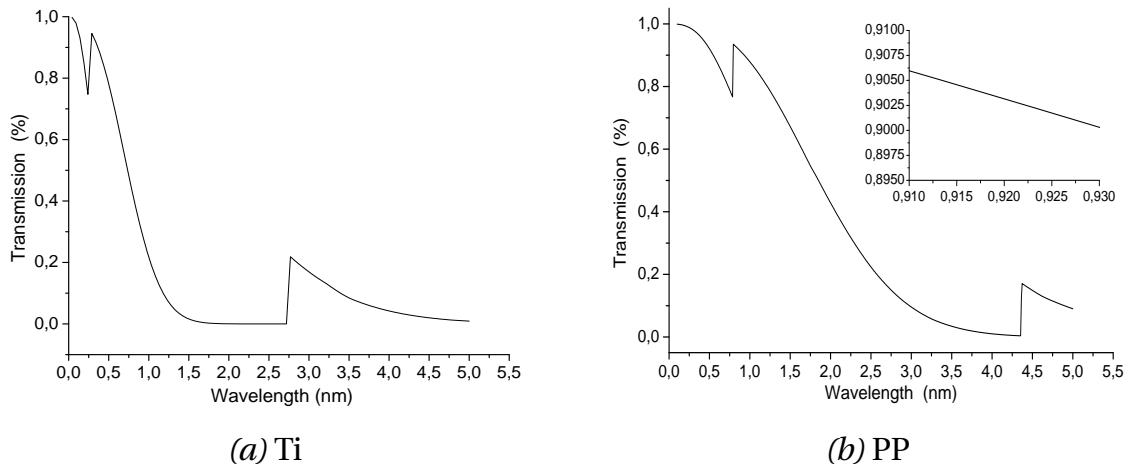


Figure 3.11: Filter transmission, (a) Ti and (b) PP. The inset in the last one shows one of the wavelength regions used with the X ray spectrometers.

Two X ray filters have been used to select the radiation that enters the pinholes. One of them was a 5 μm Ti sheet, the *Ti* filter. The second, called *PP*, was composed of two materials: a 1 μm sheet of polypropylene with 0.2 μm Al coating. Figure 3.11 shows the transmission characteristics of both filters. The Ti filter only transmits the most energetic X rays, giving information about the hotter part of the plasma as the transmitted wavelengths are mainly due to Planck radiation. On the contrary, the PP filters transmit also lower energies, so the images from them contain information on the behaviour of colder plasma regions with electron temperatures in the order of 100 eV with discrete and continuous emission. Commercial X ray films were used to record the images: Fujifilm IX 80 and Kodak DEF film having similar characteristics.

Figure 3.12 shows a photograph of the camera, with its longitudinal dimension. The screw thread at the right side of the picture prevents light from entering the pinhole when the camera is closed. Brass was used for fabrication and has been covered with vacuum proof black paint to avoid light reflections that could be registered by other devices, like the visible streak camera.

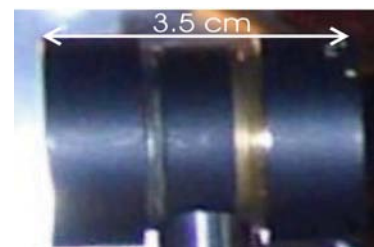


Figure 3.12: Pinhole camera.

Plasma angular distribution from X ray pinhole images

One of the parameters extracted from the X ray pinhole images is the angular distribution of the emitting plasma regions. It is defined as the integral of the X ray emission in a line path with an angle respect the target surface. The integration takes

place between the line positions of maximum emission and half of this maximum and a FORTRAN program was written to automatize this task, see appendix A.

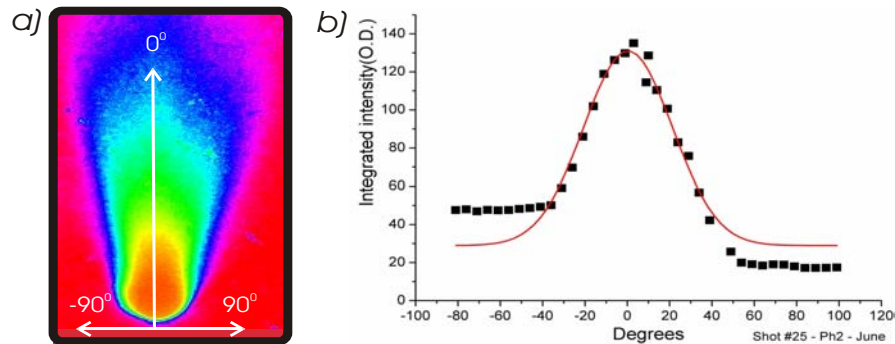


Figure 3.13: *a)* X ray pinhole image and *b)* plasma angular distribution calculated from it.

The angular intensity distribution provides information on the angle of plasma expansion, as any peak on the integrated intensity at a certain angle means there is a higher ion concentration. Figure 3.13 shows a typical angular distribution with the expected Gaussian shape [33]. The 0° angle corresponds to the direction perpendicular to the target surface, where the maximum emission intensity and length are generated; the symmetric values of -90° and 90° are then the limiting angles of the angular distribution of the X ray emission, see Fig. 3.13.

As the pinhole image in Fig. 3.14 shows, the central part of the pinhole images may be saturated and will give no information on the plasma distribution, thus it is avoided in the results presented in this work. A typical trace is shown for a -10° angle on an X ray image with the part to integrate inside the line marked with the dotted line.

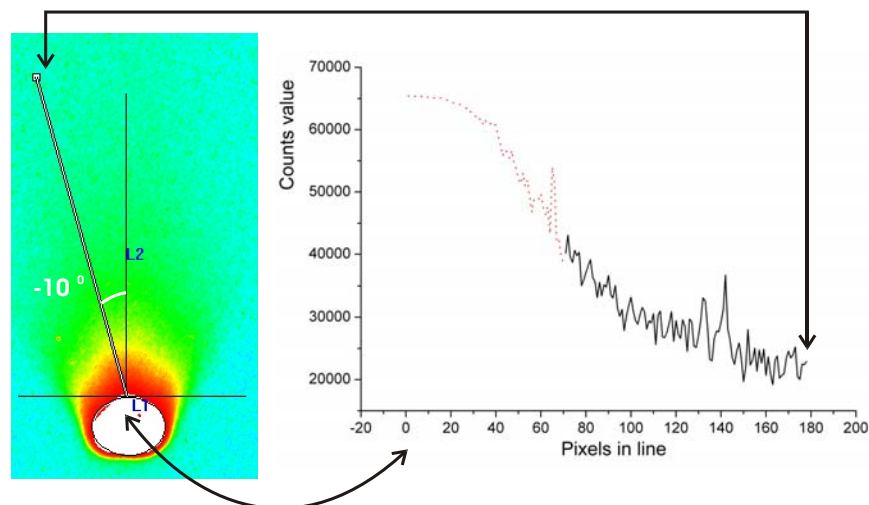


Figure 3.14: Angular pixels line overimposed on the pinhole image (*left*) with the resulting trace at -10° (*right*).

3.2.2 Visible streak camera

Streak cameras generate images with the space and time along perpendicular axes in a particular wavelength range, the visible in the case of the device used within this work, see Fig. 3.15. As observed in the images, the plasma expansion in one spatial dimension is recorded against time, allowing for an estimation of the velocity of the plasma that glows in the visible range. Plasma emission in this wavelength range comes from the colder plasma regions that are expanded after the laser pulse.

As it is explained later in paragraph 3.2.2 at page 45, spatial resolution is obtained along the slit. This was oriented to observe plasma expansion at 90° with respect to the target surface.

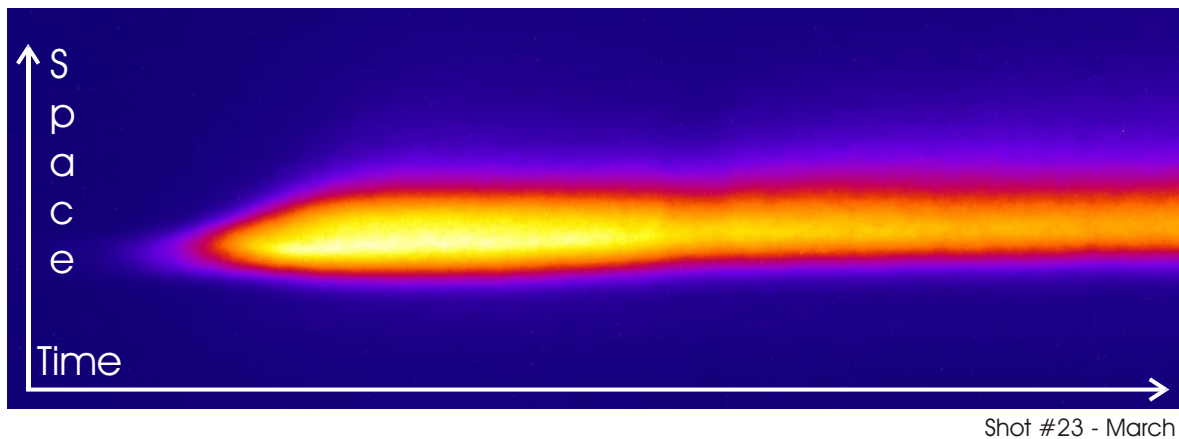


Figure 3.15: Visible streak typical image.

Streak Cameras Working Principle

The light enters the streak camera through a slit which gives the spatial resolution along it. Light which passed the slit is absorbed at a photocathode and generates an amount of electrons proportional to the number of photons. The electrons are accelerated through the streak tube and sent to a multi-channel plate (MCP) that multiplies the number of electrons. A phosphor screen at the end produces a visible image, see Fig. 3.16.

A pair of sweep electrodes in the streak tube deflects the electron beam such that it arrives at the MCP at positions that linearly depend on time. Once the electrons enter the MCP and are multiplied by a factor of 1 000, they impact on the phosphor screen and produce an image which is recorded by a CCD camera. The CCD sends the digital image to a computer where it is stored for later analysis.

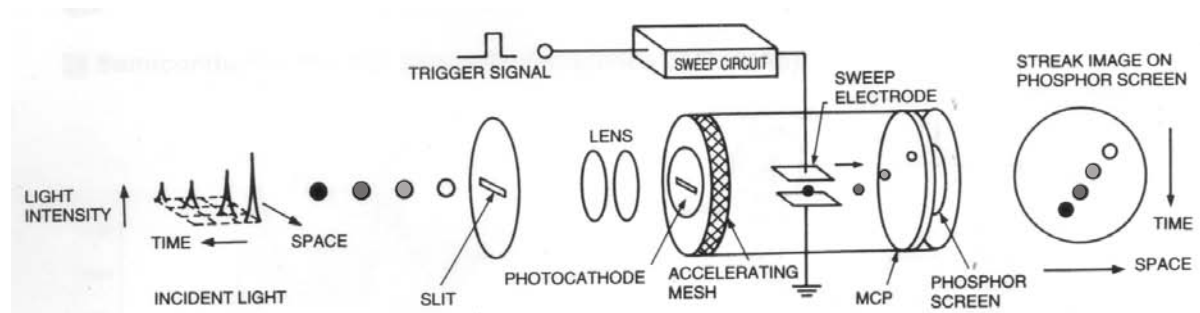


Figure 3.16: Illustration of the streak camera working principle. From [48]

Laboratory Setup

The visible streak camera was placed under the target chamber due to space constraints in the experimental area. A guiding system with a mirror and a teleobjective was assembled as it is shown at the right side of this paragraph in Fig. 3.17. The mirror reflects the light from the plasma inside the target chamber through a vacuum proof transparent window attached to a CF-100 flange. The reflected light goes along the line of sight of the teleobjective attached to the streak camera, and it is focused on the target and increases the spatial resolution of the streak images. The construction has an orientation of 90° with respect to the target surface, thus the observed space direction is the axis parallel to the target surface.

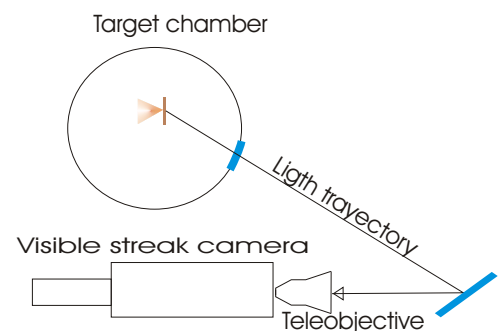


Figure 3.17: Visible streak setup scheme. the streak camera, and it is focused on the target and increases the spatial resolution of the streak images. The construction has an orientation of 90° with respect to the target surface, thus the observed space direction is the axis parallel to the target surface.

Camera Calibration and Plasma Velocity Measurement

The images must be calibrated for both recorded dimensions, the spatial and temporal. For the spatial calibration, the target itself was used. The target was moved by fixed steps along the spatial axis of the visible streak camera and these steps were linked to the corresponding digital images.

The temporal calibration is made with the time delay between the trigger of the streak camera and the laser. This delay can be altered at wish. The *nhelix* laser beam used without amplification can produce light signals when applied to metals like aluminum.

Thus the target frame is used to create light signals from the delayed laser beam. The delay variations appear in the streak images as vertical pixel displacements that can be associated with the time delay between the trigger signals. Figure 3.18 shows the spatial and temporal (200 ns streak time) calibrations of the visible streak camera images obtained by these methods.

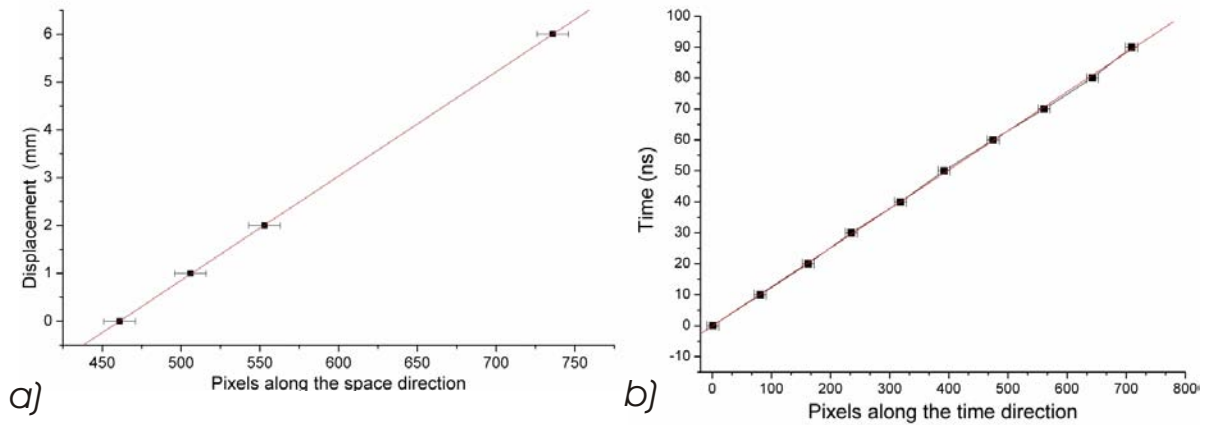


Figure 3.18: Visible streak calibration for *a)* the space and *b)* time dimensions.

With the calibrated images of the streak camera, plasma positions at defined times can be determined and the mean velocity of the glowing plasma regions estimated from:

$$Velocity = \frac{\Delta Space}{\Delta Time}, \quad (3.4)$$

where $\Delta Space$ means the difference between positions of the plasma at the time moments used to calculate $\Delta Time$. The spatial positions of the plasma are calculated from points with well defined glowing properties, like points where the light has half of its maximum intensity. $\Delta Time$ is obtained with the help of a calibration curve like the one shown in Fig. 3.18.

3.2.3 Spectrometers

Spectrometers have many different applications, going from the observation of element abundance on the Moon [49], to the analysis of scattered X rays [50].

The working principle of a diffraction spectrometer is based on the interference of light reflected from a grating [51]. The light reflecting from the grating is sent to the output slit. Due to interference in the grating, the output light has appreciable intensity only at the wavelengths where the interference is constructive. This can happen several times for the same wavelength, producing different orders of reflection. The angles for constructive interference are called Bragg angles and for a given λ , they obey the following relation:

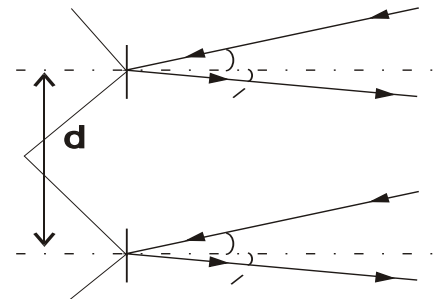


Figure 3.19: Light paths.

$$m \lambda = d(\sin \alpha + \sin \acute{\alpha}) \quad (3.5)$$

with m the order of the reflection. The quantities α and $\acute{\alpha}$ are the incident and re-

flection angles, respectively, and d is the distance between the grating grooves. Figure 3.19 provides a scheme of the optical paths for incident plane waves and their reflections on a grating with two grooves. The specular reflection from the grating occurs when $\alpha = \acute{\alpha}$ and $m = 0$.

3.2.4 The VM-502 spectrometer

The VM-502 is a spectrometer with a concave diffraction grating and a wavelength range going from the far ultraviolet to the visible, from 50 to 450 nm. The bandwidth is of the order of 50 nm and uses only the first diffraction order, as higher orders are too weak to be detected by the device.

The VM-502 spectrometer has two output ports that can be selected by means of an orientable mirror and a concave grating that acts as a diffractive and focusing element at the same time.

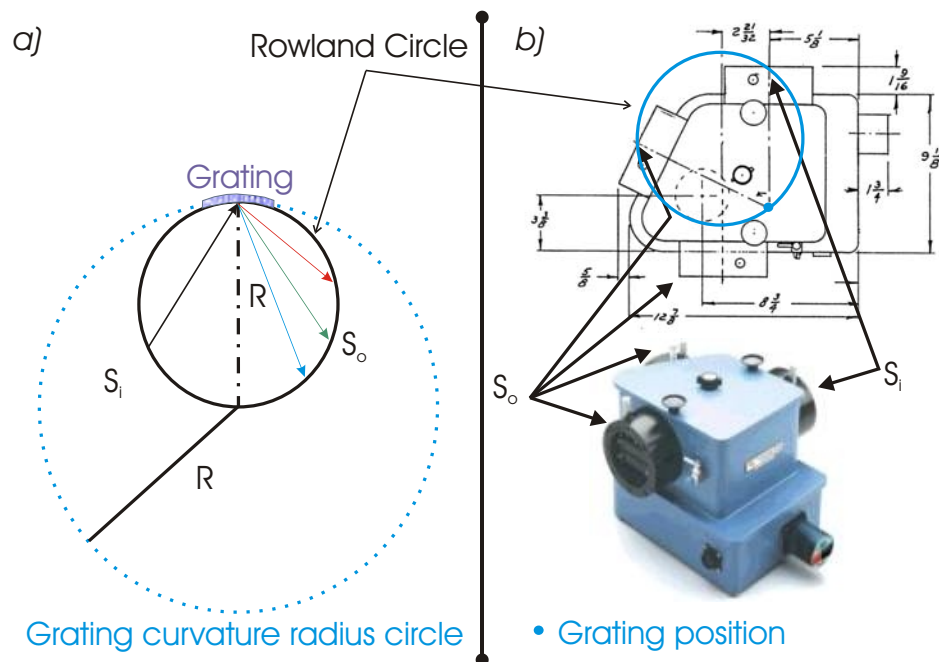


Figure 3.20: Rowland circle scheme *a)* general and *b)* with the parts of the VM-502 signaled. Spectrometer scheme adapted from [52]

The system formed by the entrance slit, grating and light sensor are on the Rowland circle with a Paschen-Runge mounting system. The Rowland circle is a circle with diameter equal to the grating radius of curvature. When a light source is placed on this circle, the spectra produced by the grating are focused on the same circle. On figure 3.20 this geometry is depicted schematically with the corresponding points for the VM-502.

Light enters the spectrometer through the slit S_i and interacts with the grating, being reflected at different angles according to its wavelength, with only a few wave-

lengths going towards the output slit S_o . The observed wavelengths are adjusted by rotation of the grating with a digital controller attached to the monochromator through a serial port. The concave grating has a focal length of 20 cm and an aperture ratio of $f/4.5$. To increase the apparatus sensibility the output slit has been substituted with a CCD camera and a multichannel plate. The system is connected to a PC for data storage. Background correction has been made with an aluminium spectrum to avoid the presence of black body Planck radiation, which is material independent, by subtraction of the background spectrum from the experimental one.

3.2.5 *Focusing X ray spectrometers*

The X ray spectrometers described here have been used in spatially resolved studies of the spectral properties of the plasmas, where the radiation comes mainly from the decay of electron levels through highly charged ion states. The spatial resolution of these spectrometers was employed in correlation with data from the X ray pinhole images. Their high spectral resolution was used for the estimation of electron temperatures from the ratio of resonant to j satellite lines.

X ray spectroscopy is used to access plasma or dense materials not transparent to longer wavelengths. Plasmas may have regions of high density from which only X rays will be transmitted. This radiation was used to study plasmas in many ways. For example, in pinch plasmas, X ray continuum emission was used to probe the electron temperature [53]; and in the study of the sun X ray spectroscopic emission was used to make estimations of the coronal electron temperature [45].

Operation of the focusing X ray spectrometers

The **Focusing Spectrometer with Space Resolution (FSSR)** has been developed by A. Ya. Faenov and his collaborators [54] to obtain high luminosity without compromising the wavelength and spatial resolution. The FSSR provides images with simultaneous spatial and spectral resolution in perpendicular directions by using a crystal with a spherically bent surface. In the meridional plane the geometry is equivalent to the Rowland circle mentioned in section 3.2.4, in the sagittal plane it is a simple curved mirror [55], so the spectral resolution is obtained in the meridional plane and the spatial resolution in the sagittal one, see Fig. 3.21.

The internal structure of the crystals acts as a grating in the meridional plane since the crystal cells have dimensions comparable to the X ray wavelengths. The dispersion law for this system is the previously mentioned Bragg law (equation 3.5). In the perpendicular plane, the curved surface of the mirror gives the spatial resolution just by reflection of the incoming light. The surface is curved to concentrate the light and to assure high luminosity, which is one of the main problems when working with X rays.

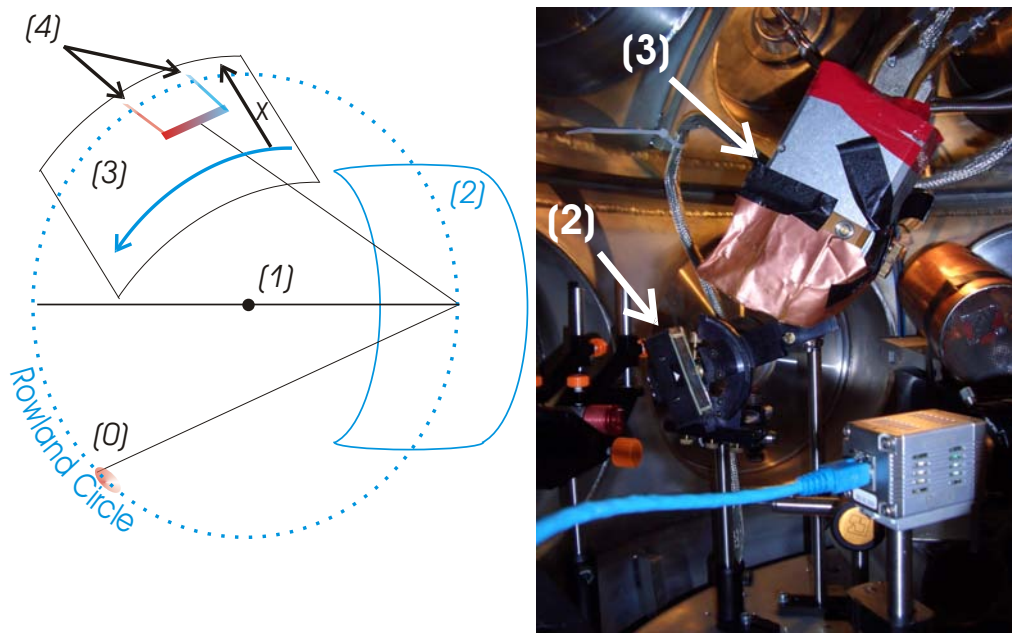


Figure 3.21: FSSR dispersion in the meridional plane(...) and spatial expansion in the sagittal plane. (0) X-ray source, (1) Plane center, (2) crystal, (3) X ray detector, and (4) spatially resolved spectral lines. In the right image the detector is an X ray CCD camera.

One of the main advantages of the FSSR is that the sensor system for the X ray is replaceable, so different devices can be used. In these experiments two sensors have been used: an X ray CCD camera and X ray films. Two configurations are used with the FSSR for wavelength adjustment, the configurations are called 1-D and 2-D because of the number of spatial dimensions that are recorded.

FSSR 1-D In the 1-D configuration, the FSSR is adjusted to have the X ray detector on the Rowland circle in the sagittal focus. Then the light source is focused on the detector by the bent crystal, so the spectral lines are focused on the detector plane. Therefore, the 1-D scheme has the maximum wavelength resolution that the device may give, reaching the theoretical values of $\lambda / \Delta\lambda = 10\,000$.

The bent surface acts as focusing mirror with a radius of curvature equal to the diameter of the Rowland circle in the spatial direction, so the source size is not important in the determination of the FSSR resolution and the only appreciable spatial difference is for the dependence of the spectrum on the spatial position. Figure 3.22 shows a spectrum obtained in this 1-D configuration; the absence of any spatial records on it is indicated by the same line width obtained at different spatial positions. Considering the two constraints for the FSSR adjustment in this scheme, the detector position inside the Rowland circle and the Bragg law, the accessible wavelength range is reduced, which is the main drawback of this configuration.

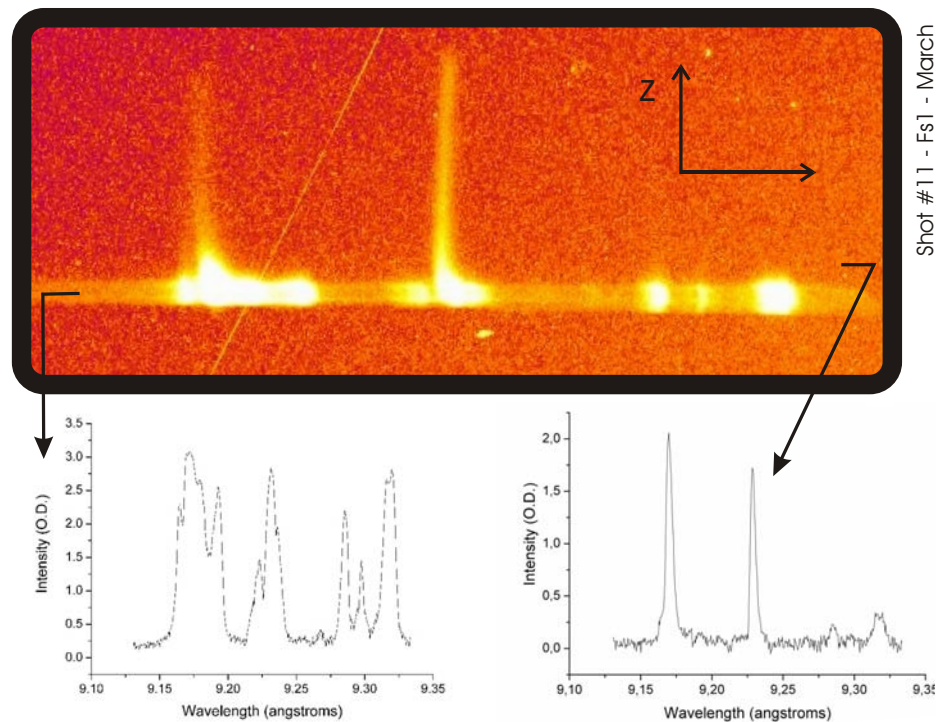


Figure 3.22: FSSR Mg spectrum in the 1-D configuration with spectra at different spatial positions.

FSSR 2-D The other FSSR configuration is named 2-D because of the recorded spatial properties. In this case the detector is placed outside the Rowland circle, so a larger number of wavelengths can be accessed with this configuration. As the detector is outside the Rowland circle, see Fig. 3.23, the spectral resolution is reduced through the dependence of the line width on the source size. Nevertheless this is advantageous for understanding the dynamics of the different ion species of the plasma, since the lines coming from different atomic levels should have different widths. Knowing which different ion species contribute to the observed lines, angular distributions corresponding to these ion species can be detected.

3.2.6 X ray film calibration

X ray films were used in these experiments in two kinds of devices: the previously presented X ray pinhole camera and X ray spectrometers, described in the previous section 3.2.5.

The X ray films employed in these detectors are developed and then digitized, obtaining as a result images where the intensity is expressed in counts. The relation between film darkening and intensity counts obeys an exponential law [57] as the one shown in Fig. 3.24 for a Kodak 101-07 film. So an exponential function was found with

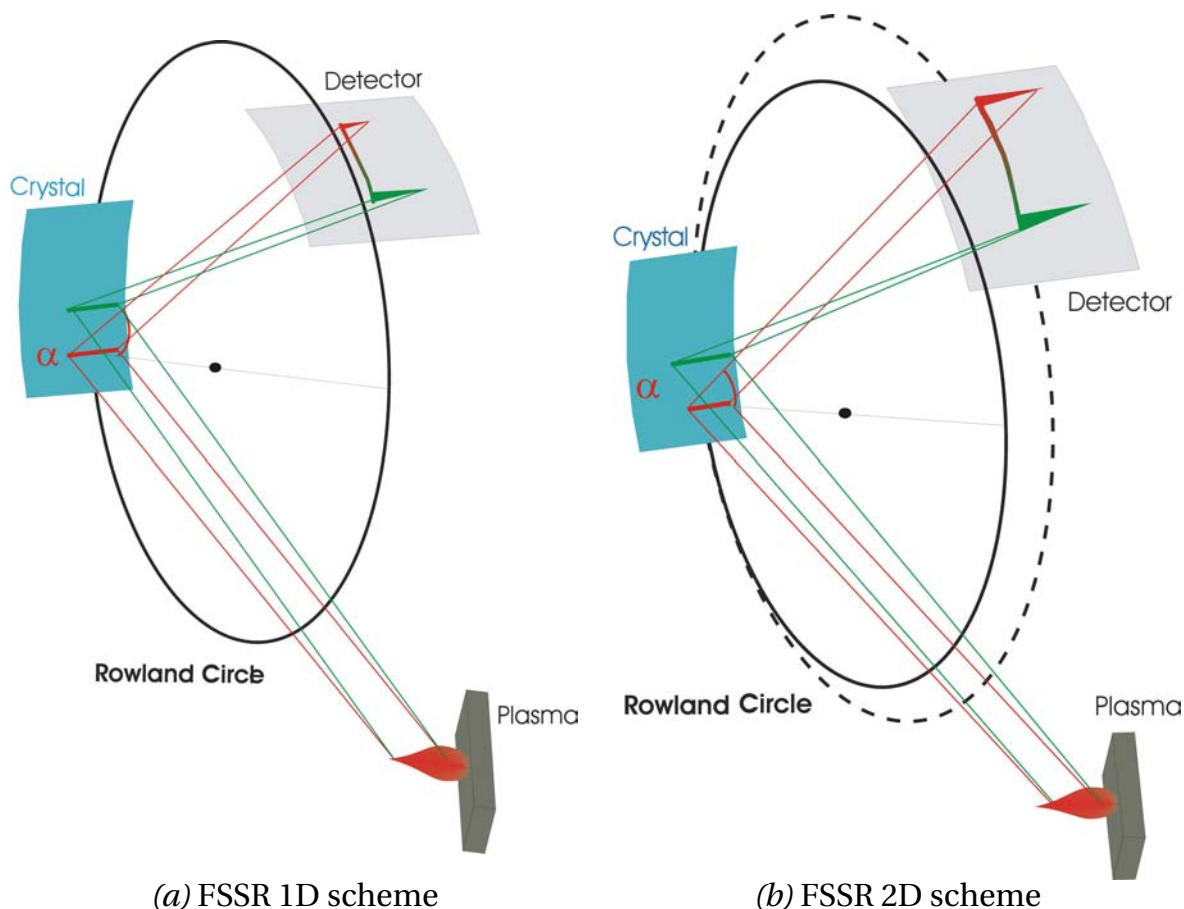


Figure 3.23: Possible FSSR schemes with the Bragg angle α for one wavelength and the center of the Rowland circle emphasized.

the ORIGIN software to fit counts to optical density (OD) values:

$$OD = 0.00002 \cdot \text{Counts} \cdot (1 + 0.00019 \cdot \exp(0.00014 \cdot \text{Counts})), \tag{3.6}$$

with OD the optical density and Counts the digitized intensity value.

The optical density is the quantity obtained from the logarithm of the inverted transmittance of the film for a certain wavelength, and in developed films it is proportional to the light intensity absorbed by the film. The film response or optical density value for a certain light intensity is wavelength sensitive so the OD calibration must consider this variation. But as Fig. 3.25 shows for the Kodak 101–07 film, this response is constant for a large range of wavelengths, going from 20 Å(100 eV) at the beginning of the energy scale to 2 Å(1000 eV) at the middle. The rectangle marks the area of wavelengths used in the X ray spectrometers adjustment. As the film response in such a wide energy range

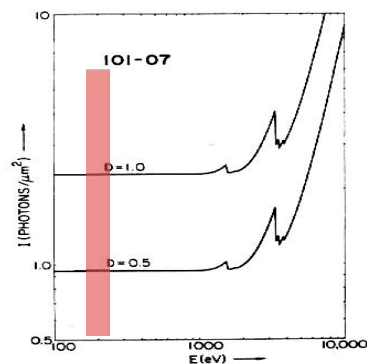


Figure 3.25: Film response at optical densities of 0.5 and 1.0 for the Kodak 101–07 films. Adapted from [56]

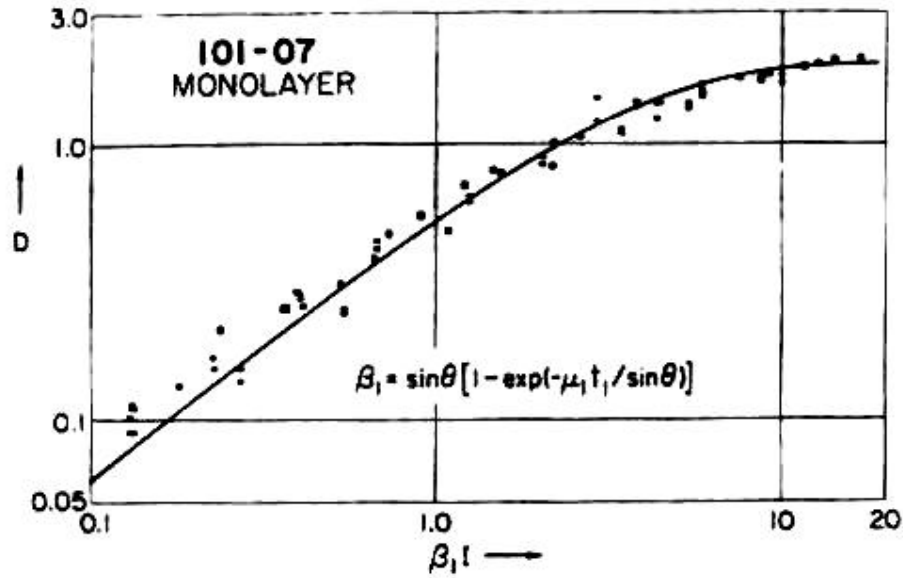


Figure 3.24: Optical density (OD) versus intensity for the Kodak 101–07 film. A similar graph can be obtained for the films used in the experiments. Adapted from [56]

is constant, there is no need to consider any further adjustment of the OD values for the different wavelengths and the obtained OD values are directly proportional to the intensity.

Section 3.3 General setups

All the diagnostics have been used in two different setups, differing by the laser beam orientation with respect to the target surface. They are called the *normal* and 45° setup, referring to the laser beam angle of incidence.

The laser beam orientation limits the possible positions of the plasma diagnostics, which must be changed accordingly. These changes are listed and commented in this section. The targets have always been magnesium slabs of 1 mm thickness, situated in a vacuum target chamber.

In order to change the laser flux and focal spot intensity distribution, changes have been applied to the laser chain, maintaining the target position fixed in all the experiments. To change these two parameters, the focusing lens was moved along the optical axis.

3.3.1 Normal incidence setup

The *normal* setup configuration used a laser beam energy of 44 ± 3 Joules. Since the laser beam is perpendicular to the target surface (see Fig. 3.26), resonant absorption processes are not expected to be important for the laser-plasma interaction within this configuration.

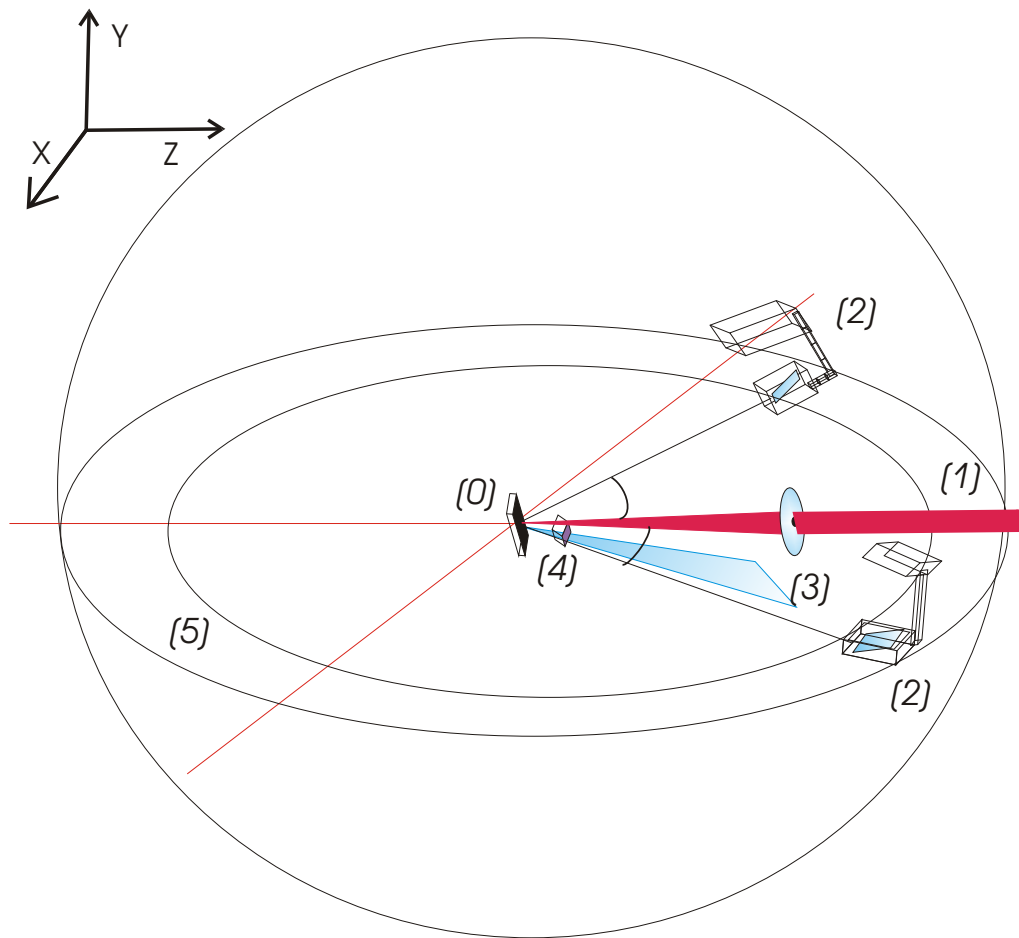


Figure 3.26: Normal incidence experimental setup scheme with the FSSR angles β_1 and β_2 , 40° and 20° respectively. (0) Target, (1) laser beam, (2) FSSR spectrometers, (3) light path to the optical streak camera, (4) X ray pinhole camera, and (5) placement ring inside the vacuum chamber

The two FSSR spectrometers (Fs1 and Fs2) were adjusted with two orientation angles, 40° and 20° with respect to the laser beam axis, $-z$ in Fig. 3.26, so the plasma expansion projected at these angles was visible. As the plasma expansion is symmetric around the axis perpendicular to the target surface, no large differences have been observed for these spectrometers. One pinhole camera was placed directly under the target to check the geometry of the X ray plasma expansion, while the streak camera was used to record the expansion of the cooling plasma perpendicular to the target surface.

FSSR spectral adjustment for *normal* incidence

In this experimental setup the FSSR was configured to observe the resonant line and satellites of the He-like magnesium ions, presented in Table 3.1. Both spectrometers were configured to observe the same group of lines in order to facilitate the comparison between the results.

| Kind of line | Transition | λ (Angstroms) | Key letter |
|-------------------------|---|-----------------------|------------|
| Resonant | $1s^2\ ^1S_0 - 1s2p\ ^1P_1$ | 9.170 | w |
| 4l satellite | $1s^24p\ ^2P_{1/2} - 1s2p4p\ ^2D_{3/2}$ | 9.182 | |
| 4l satellite | $1s^24p\ ^2P_{3/2} - 1s2p4p\ ^2D_{5/2}$ | 9.182 | |
| 3l satellite | $1s^23p\ ^2P_{3/2} - 1s2p3p\ ^2P_{3/2}$ | 9.192 | |
| 3l satellite | $1s^23p\ ^2P_{1/2} - 1s2p3p\ ^2D_{3/2}$ | 9.193 | |
| Intercombination | $1s^2\ ^1S_1 - 1s2p\ ^3P_2$ | 9.231 | y |
| 2l satellite | $1s^22s\ ^2S_{1/2} - 1s2s2p\ ^2P_{3/2}$ | 9.235 | q |
| 2l satellite | $1s^22p\ ^2P_{1/2} - 1s2p^2\ ^2P_{3/2}$ | 9.295 | b |
| 2l satellite | $1s^22p\ ^2P_{1/2} - 1s2p^2\ ^2P_{1/2}$ | 9.298 | d |
| 2l satellite | $1s^22p\ ^2P_{3/2} - 1s2p^2\ ^2P_{3/2}$ | 9.298 | a |
| 2l satellite | $1s^22p\ ^2P_{1/2} - 1s2p^2\ ^2D_{3/2}$ | 9.316 | k |
| 2l satellite | $1s^22p\ ^2P_{3/2} - 1s2p^2\ ^2D_{3/2}$ | 9.320 | l |
| 2l satellite | $1s^22p\ ^2P_{3/2} - 1s2p^2\ ^2D_{5/2}$ | 9.321 | j |

Table 3.1: He-like resonant and intercombination lines with some satellites.

The line identification keys used in the table were obtained from [45] and the wavelength data from the calculations published by Safranov et al. [58]. The resonant and intercombination lines have been seen in plasma regions away from the near main plasma generation region near the target surface. An example is shown in Fig. 3.22, where the base line is produced by bremsstrahlung emission near the target surface, and the expansion of the ions is observed by the extension of the resonance and intercombination lines in a direction perpendicular to the target surface.

In this experimental configuration the sensor systems for both spectrometers were X ray film boxes with two sheets of PP filters. The filters exclude visible light from entering the employed X ray film box. Otherwise it would activate the film in a not desired wavelength range.

X ray pinhole camera

The X ray pinhole camera was placed in front of the target surface at an angle of $53 \pm 0.5^\circ$ with respect to the normal. Its position did not disturb the laser beam and allowed the observation of the plasma expansion along the axis perpendicular to the target surface, which is the main expansion direction. Two pinhole cameras were used with different filters to observe simultaneously two plasma regions emitting in the X ray range: the hot and cold X ray regions, as Fig. 3.27 shows.

The hot region corresponds with a volume frequently called the ‘hot spot’. As wavelengths that pass through the Ti filter used for hot regions are in the range of 0 to 0.5 nm and there is no discrete radiation emitted within this range, only bremsstrahlung radiation can be detected with this filter. With the PP filter, radiation may have up to 2 nm, which implies a much wider range of discrete radiation passing through it and also a larger amount of the bremsstrahlung and recombination radiation that may be detected. The pinhole magnification factor of the camera was 0.42, so the digitized

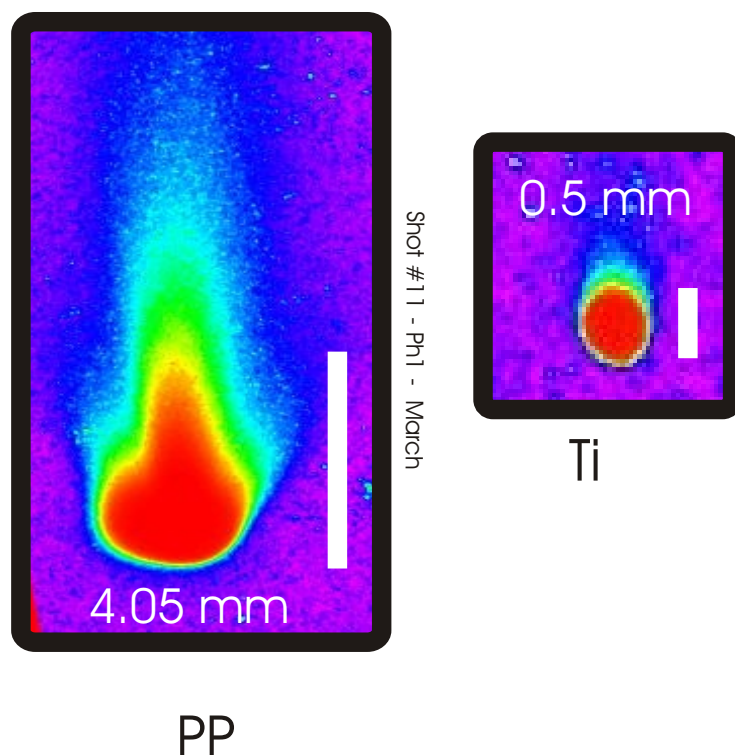


Figure 3.27: Pinhole images with the PP and Ti filters corresponding to the cold(*left*) and hot(*right*) regions, respectively.

images must be multiplied by 2.38 to obtain the correct spatial dimensions.

Visible streak camera

The visible streak camera was placed with a filter of optical density 1 to avoid reflections on the final image. With average values of the laser energy used in this configuration, the reflected light could spoil the interpretation of data from this device. The streak time was adjusted to 100 ns. The real achieved streak time has been of the order of 50 ns which is enough for observing in detail the target heating and the beginning of expansion.

3.3.2 45° incidence

In this setup the laser beam incidence of 45° may allow for resonant absorption phenomena, but the low laser flux with a maximum of about 10^{14} W/cm² actually discards the importance of such a phenomenon [59]. The mean energy of the laser beam was 33 ± 4 Joules, 75% of the *normal* setup.

The setup was changed to accommodate the new laser and target geometry without interfering with any diagnostics. In this configuration two X ray pinhole cameras have been used, and they have been placed at perpendicular directions to the plasma

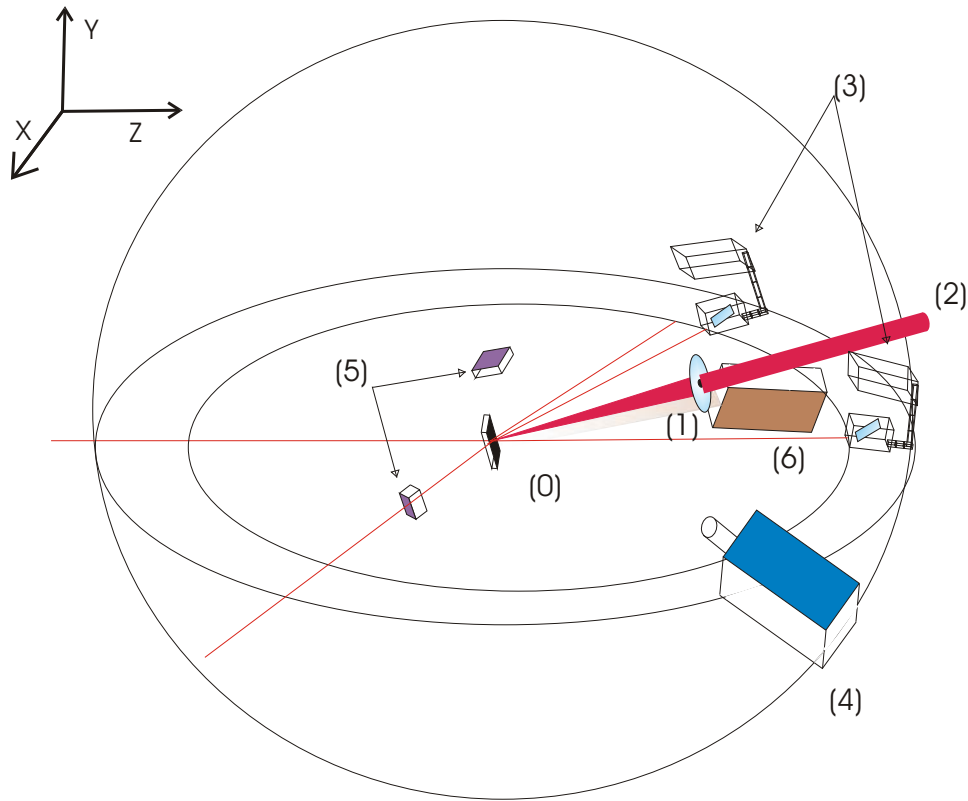


Figure 3.28: 45° setup scheme. (0) Target, (1) last lens, (2) laser beam, (3) FSSR spectrometers, (4) VM-502 spectrometer, (5) X ray pinhole cameras and (6) visible streak camera.

expansion in order to allow for better observation. The two FSSR had different observation angles, one of them was directed perpendicular to the target surface. The VM-502 spectrometer was added to obtain information about the plasma emission in the UV range.

FSSR

The FSSR observation angles have no correspondence to the ones from the *normal* incidence setup, since they were placed at 90° and 10° with respect to the target surface. The device placed perpendicular to the target surface was Fs1.

The Fs1 spectrometer used as light sensor a X ray CCD camera with filters to avoid saturation. A PP filter was also used to stop visible light from entering the CCD chip. Thick plastic filters composed by 12 micrometers of Mylar and $22 \mu\text{m}$ of Kapton were placed between the spectrometer crystal and the CCD detector. The transmission of these thick plastic materials in the X ray range is rather low as shown in Fig. 3.29, with the combined transmission curve of Mylar, Kapton, and the PP filters in the wavelength range of Fs1. Even with such a low transmission, the CCD became saturated at high laser fluxes at the peak of the main spectral lines.

The line intensities in the spectra have to be scaled according to the transmission

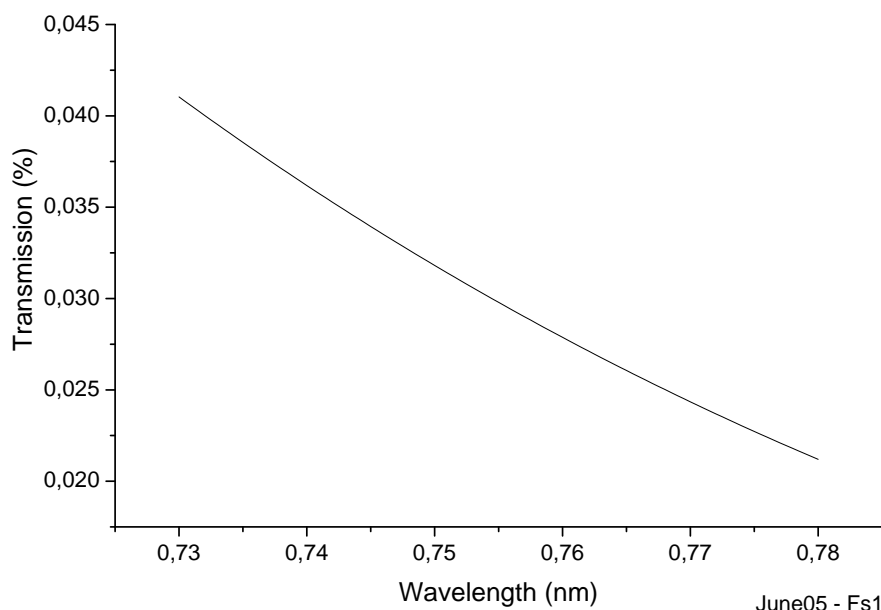


Figure 3.29: X ray transmission for the filter employed on the Fs1 spectrometer

profile between 7.8 and 7.3 Å.

| Line | Transition | λ (Å) | Denomination |
|--------------|---|---------------|-------------------------|
| He- γ | $1s^2\ ^1S_0 - 1s4p\ ^1P_1$ | 7.473 | Resonant |
| He- γ | $1s^2\ ^1S_0 - 1s4p\ ^3P_1$ | 7.478 | Intercombination |
| 4l satellite | $1s^22p\ ^2P_{3/2} - 1s2p4p\ ^2D_{5/2}$ | 7.730 | Satellite |
| 4l satellite | $1s^22p\ ^2P_{3/2} - 1s2p4p\ ^2D_{3/2}$ | 7.731 | Satellite |
| He- β | $1s^2\ ^1S_0 - 1s3p\ ^1P_1$ | 7.851 | Resonant |
| He- β | $1s^2\ ^1S_0 - 1s3p\ ^3P_1$ | 7.863 | Intercombination |

Table 3.2: The main He- β and He- γ spectral lines.

The main spectral lines for this configuration are the He- β and He- γ transitions with some satellites, as can be seen from Table 3.2; the ratio of their intensities to those of the satellites gives clues about the plasma characteristics.

X ray pinhole cameras

Two X ray cameras were used in this setup with observation directions perpendicular to each other. The first one (Ph1) is placed on the top of the target looking along the $-y$ axis, with the convention of Fig. 3.30. The second pinhole (Ph2) was placed perpendicular to Ph1, parallel to the $-x$ axis in the same figure. The Ph1 camera had only one hole covered with two different filters during the experiments, the Ti and the PP filters. As both filters probe very distinct plasma regions the records reflect the differences between them, see Fig. 3.31. The Ph2 camera had two pinholes of 150 μm diameter covered with Ti and PP filters respectively, so the regions of the X ray plasma

can be compared at the same lasing conditions.

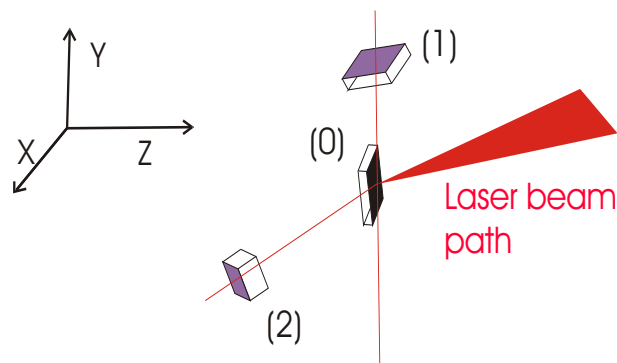


Figure 3.30: Pinhole cameras orientation with respect to the target. (0) Target, (1) Ph1, and (2) Ph2.

The magnification factor of Ph1 was modified during the experimental time from 0.5 to 1 to find the most adequate value for the recording of geometrical changes in the plasma emission. The factor 0.5 was finally chosen because of a better fitting of the image on the X ray film.

Visible streak camera

Because of the reduced laser flux used for this configuration, the optical density filter has been removed. The streak time was adjusted to 200 ns in order to observe the plasma expansion in more detail thus the total observation time was around 140 ns.

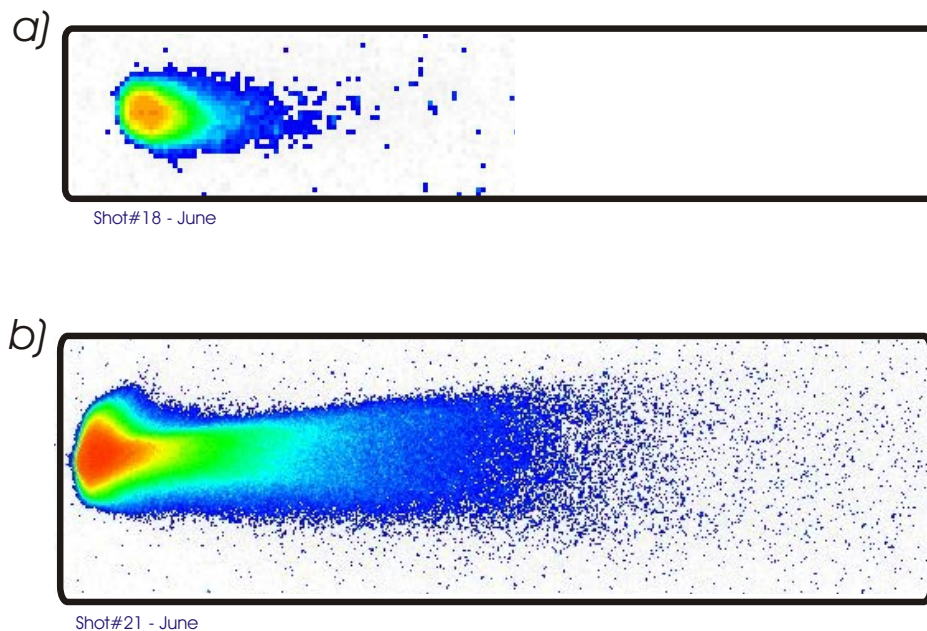


Figure 3.31: Ph1 records with a) Ti filter and b) PP filter. Not at the same scale.

Chapter 4

Experimental Results

Presented here are the results obtained with the setups and devices described in the previous chapter. The first section discusses the generation of plasma jet structures made of highly charged ions and the experimental conditions needed therefore to produce them. Besides, the changes in jet properties due to modifications in lasing conditions are commented. The influence of the laser beam divergence on plasma characteristics is described in the second section. The last section is dedicated to a quantitative analysis of the ultraviolet spectra.

Section 4.1 Plasma jets

In the experiments made with the *nhelix* laser ionic jet structures were obtained under certain experimental conditions. The name "jet" is given to a well collimated propagation of highly charged ions produced in the plasma. This propagation takes place over longer distances than usual plasma expansion. The jets are observed with the X ray pinhole cameras and FSSR spectrometers, and have an aspect ratio, i.e. the ratio between the jet length and diameter, of two times more than the rest of the plasma plume.

It was found experimentally that the focus of the last lens of the *nhelix* laser chain had to be placed in front of the target surface for such jets to be formed. The role of laser parameters, including the focal position with respect to the target surface, on the jet generation has been determined from X ray pinhole cameras and FSSR images. The last ones allow for correlations between the spatial extension of the lines and jet structures.

4.1.1 Jet generation

The observation of plasma jet generation was made in the frame of a scientific program of the GSI [60] with the aim of measurement of the ion stopping power of plasmas. For such measurements the knowledge of the plasma parameters is of particular importance, because the energy loss depends on them, as indicated by the Bohr-

Bethe-Bloch formula:

$$-\frac{dE}{dx} = 4\pi n_{tot} \frac{Z_{eff}^2 e^4}{m_e v^2} [\Lambda_0 + Z_{eff} \Lambda_1 + f_{Bloch}(v)], \quad (4.1)$$

where n_{tot} denotes the density of bound and free electrons and m_e the electron mass, Z_{eff} is the effective charge of the beam ion and v its velocity. The expression $Z_{eff} \Lambda_1$ is the Barkas term, equivalent to the second Born correction, $f_{Bloch}(v)$ is the Bloch term which bridges the gap between classical and quantum theory and, finally, Λ_0 corresponds to the Born random phase approximation [8].

Recent investigations of laser created plasmas from solid slabs confirmed their high directionability perpendicular to the target surface. A parameter that reflects well this plasma feature is the angular distribution of the plasma flow as deduced from the X ray pinhole camera images and defined in the paragraph 3.2.1. The angular distribution of the plasma emission have received certain attention in connection with the use of laser pulsed plasmas for chemical vapour deposition techniques [61]. The ionic angular distribution changes with the ion charge, becoming narrower as the ion charge grows [62]. With the PP filters at the pinhole cameras only highly charged Mg ions are visible, therefore a narrow angular distribution should be seen on such images.

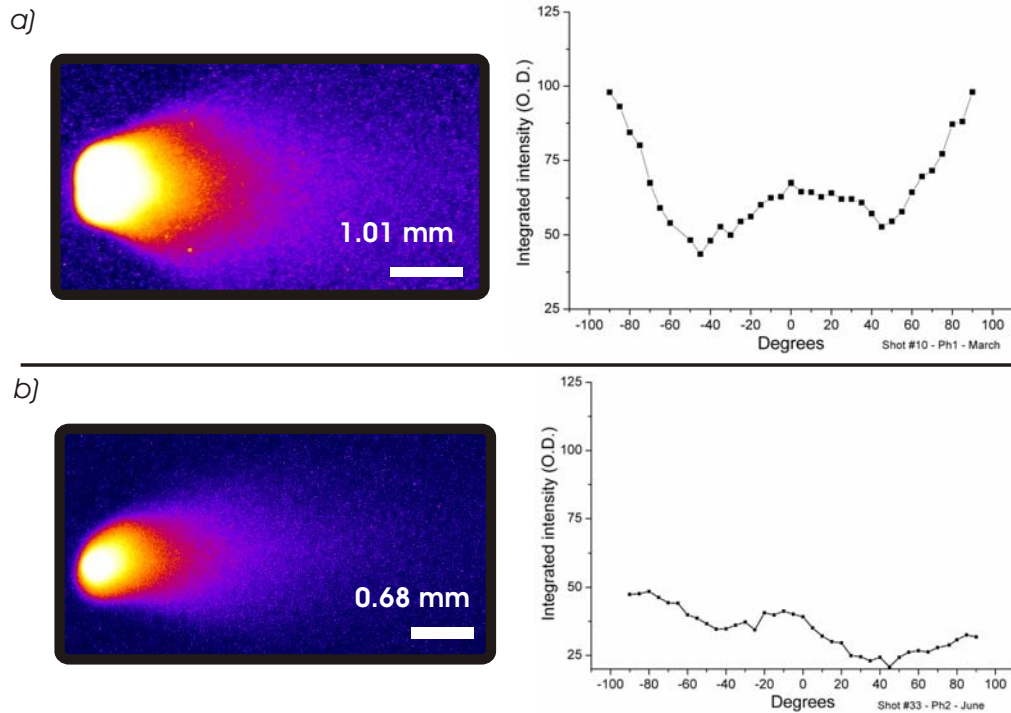


Figure 4.1: X ray pinhole images and corresponding angular distributions outside the saturated hot spot. The laser beam was focused *a)* at the target surface and *b)* 0.5 mm behind the target surface.

Both characteristics of ionic directionability and small divergence angle of highly

charged ions were found during these experiments:

- a) With the laser beam focused at the target surface with an orientation of 0° , the *normal* setup, the highly charged ion emission observed in the X ray pinhole images is spread over a small angle and mainly in the direction perpendicular to the target surface with no jet structures. This absence can be deduced from pinhole camera images and the plasma angular distribution. The privileged expansion in a direction perpendicular to the target surface can be seen in Fig. 4.1, (a).
- b) If the laser beam focus is behind the target surface, the angular distribution measured from X ray pinhole images is flat and jet structures are also missing. In figure 4.1, (b) the results of an experiment with the focus 0.5 mm behind the target surface and the laser beam at 45° with respect to the target surface are shown. No significant differences are visible in the comparison with the previous situation, despite of the smaller expansion angle and scale. Similar results were obtained for other focus positions behind the target surface.

These experimental results show that as long as the laser beam is focused behind or at the target surface no jet structures occur, independently of the laser orientation. However, such structures are formed if the laser beam is focused in front of the target within a certain range of distances.

Plasma expansion with the laser focus too close or too far from the target surface; see (a) and (c) in Fig. 4.2 respectively, does not present any jet formation. This is observed just with the focus positioned between 0.5 and 1.0 mm in front of the target surface. The jet detaches from the normal plasma flow and may achieve aspect ratios up to 4.6, see (b) in Fig. 4.2. An estimation of the maximum kinetic energy achieved by the ions in the jet can be done by taking the jet length as the distance traveled by them during the 16 ns of the laser pulse, also the time the X ray emission lasts. The 4.4 mm observed jet length leads thus to a maximum kinetic energy of the magnesium ions of 9.5 keV.

| Distance from focus to target surface (mm) | Aspect ratio |
|--|--------------|
| 0.2 | 2.0 |
| 1.0 | 4.6 |
| 1.4 | 4.0 |

Table 4.1: Plasma aspect ratio from the X ray pinholes

Table 4.1 shows that a larger plasma expansion is obtained when the distance between the focus and the target surface is augmented, as reflected in the plasma aspect

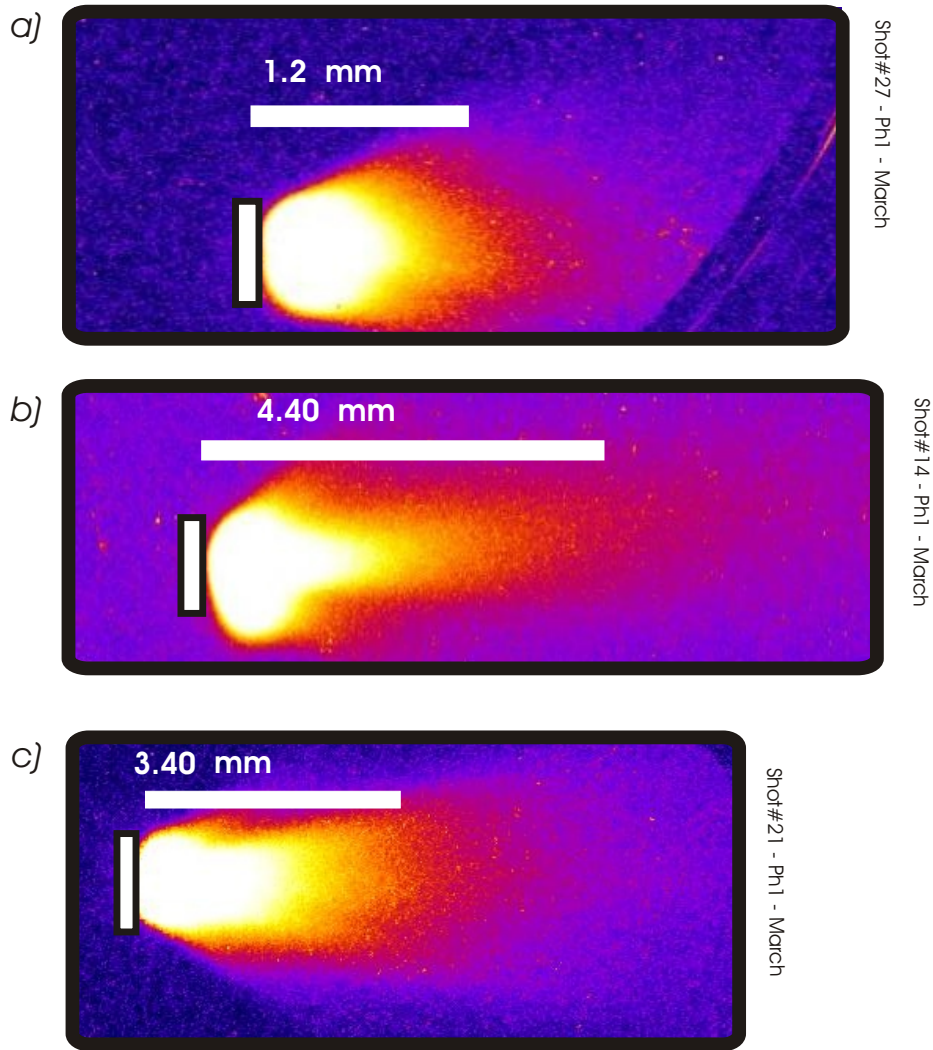


Figure 4.2: Pinhole recorded plasma expansions with focus *a)* 0.2 mm, *b)* 1.0 mm and *c)* 1.4 mm in front of target surface. The vertical bars represent 0.80 mm and the position of the original target surface.

ratio of 4 that appears with the focus 1.4 mm in front of the target surface. As the distance from the focus to the target surface becomes larger, the plasma volume that can be heated to higher temperatures is also increased as the images from Fig. 4.2 show. The largest plasma aspect ratio is measured when jets are produced, that means a larger plasma expansion due to jet generation.

Plasma kinetic energy is proportional to the electron temperature and reflects the efficiency of laser energy absorption by the plasma. Therefore variations in laser energy absorption are reflected in the electron temperature. In experiments made with similar values of laser flux, the electron temperature will give an indication of the fraction of energy that has been absorbed by the the plasma. An estimation of the T_e was made under experimental conditions for which jet formation was observed, by using the model from [45] as explained in Sec 2.3.

The temperature reaches a maximum of 160 ± 24 eV for the three experiments

when the distance from the focal point to the target surface is adequate for jet structure generation, despite the fact that uncertainties associated with these measurements make a comparison with values at other focusing positions rather difficult. The temperature of 160 ± 24 eV was measured at a distance of $95 \mu\text{m}$ from z coordinate origin. This origin is at the vertical point with the maximum emission in the FSSR spectra. The temperature has a value of 130 ± 19 eV for the other two focusing schemes, with the focus at 0.2 and 1.4 mm in front of the target surface respectively. These values were measured at distances of 57 and $37 \mu\text{m}$ from the z coordinate origin, respectively.

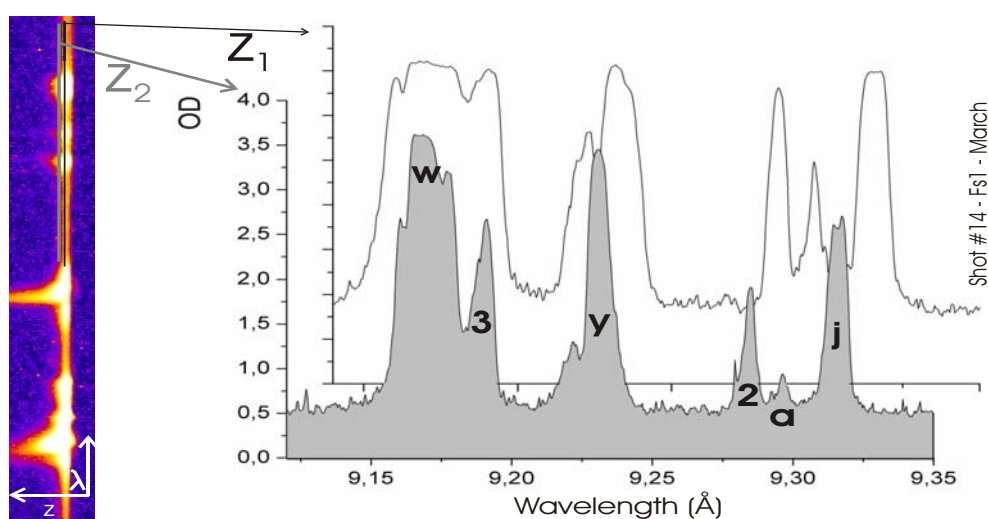


Figure 4.3: Spectra at $Z_1=47$ and $Z_2=95$ micrometers from the maximum emission position.

The variation of the vertical position of the electron temperature estimation is imposed because of constraints based on the experimental results. Closer to the target surface the spectra are saturated, making any quantification of the satellite-resonance intensities impossible. An example of this is given in Fig. 4.3, that shows two spectra at 47 and 95 micrometers in the spatial direction for the spectrum depicted at the central position in Fig. 4.3. To avoid the saturation more filters would have been necessary, but their addition leads to an elimination of the weaker radiation emitted far from the hot plasma region, of particular interest as is the radiation emitted by the expanding plasma.

The saturation in the spectrum at 47 micrometers is so large that even the line identification is not clear in the set of the resonant lines thus the spectrum at $95 \mu\text{m}$ has to be used to obtain an accurate estimation of the electronic temperature. When the focus was at 0.2 mm in front of the target surface the distance to obtain a useful spectrum could be reduced to 57 micrometers. The increase of the saturation region appears when the jet is formed, and implies a larger emission volume for the ions that

emit the lines observed in the FSSR spectrometers. In this case, the highly charged ions that form the spectrum have an important contribution to jet formation.

These spectra were acquired with the laser beam oriented normal to the target surface so the observed lines correspond to the He-like w and y with their satellites. The peak at higher wavelength, marked with j in Fig. 4.3, is formed by the association of three satellites which are not resolved. These are j , k and l mentioned in Table 3.1 at page 54. The a peak includes three other satellites, the b , d , and a meanwhile resonance and intercombination peaks are marked by the letters w and y respectively. At the left side of the intercombination line there is a satellite transition, the q satellite between the levels $1s^22s\ ^2S_{1/2} - 1s2s2p\ ^2P_{3/2}$ at 9.235 Å. Not only the 2l satellites, transitions of the form $1s^22l - 1s2l'2l''$, are in these spectra, but transitions between levels $1s^23l - 1s2l'3l''$ and $1s^24l - 1s2l'4l''$, the so-called 3l and 4l satellites, are also present. The number 3 signals the presence of a 3l satellite group and the peak situated at the right position of the resonance line is formed by the superposition of 3l and 4l satellite groups.

4.1.2 Laser flux threshold

Without changing other setup parameters, a laser flux threshold for jet formation has been observed. To investigate the threshold value the focus was positioned where the jets start to be created, i.e. at 0.5 mm in front of the target surface with the *normal* laser configuration.

With a flux of $2 \pm 1 \cdot 10^{13}$ W/cm² plasma production is achieved with geometries similar to the ones obtained with the focus at the target surface and there is no trace of any jet structure. When the laser pumping energy is doubled and the laser flux achieves a value of $4 \pm 1 \cdot 10^{13}$ W/cm², jets are generated.

Using once again the satellite-resonance ratio from the Fs1 spectra of Fig. 4.4 to estimate the electron temperature, similar values are obtained: 130 ± 19 eV when the jet is formed and 140 ± 21 eV with the lowest laser flux. Nevertheless, there is an increase by a factor of 3 in the total X ray emission for the higher value of the laser fluency.

The strong increase in the emission observed in the Fs1 spectra is also seen in the Ti filtered pinhole images, but with a value that is not possible to be precisely determined because of the films' saturation. When the jets are not present, the recorded intensity from the Ti filtered pinhole camera has a maximum value of the order of 0.7 (in optical density units on the X ray film), as (a) in Fig. 4.4 shows. In the case of jet creation, this maximum is in the saturation range of the film that is 3.5–3.6 optical density units. The emission ratio between both cases is hence at least 5, but it may be definitely higher. Thus much more highly charged ions are generated when the jet is formed, part of them expanded within the jet.

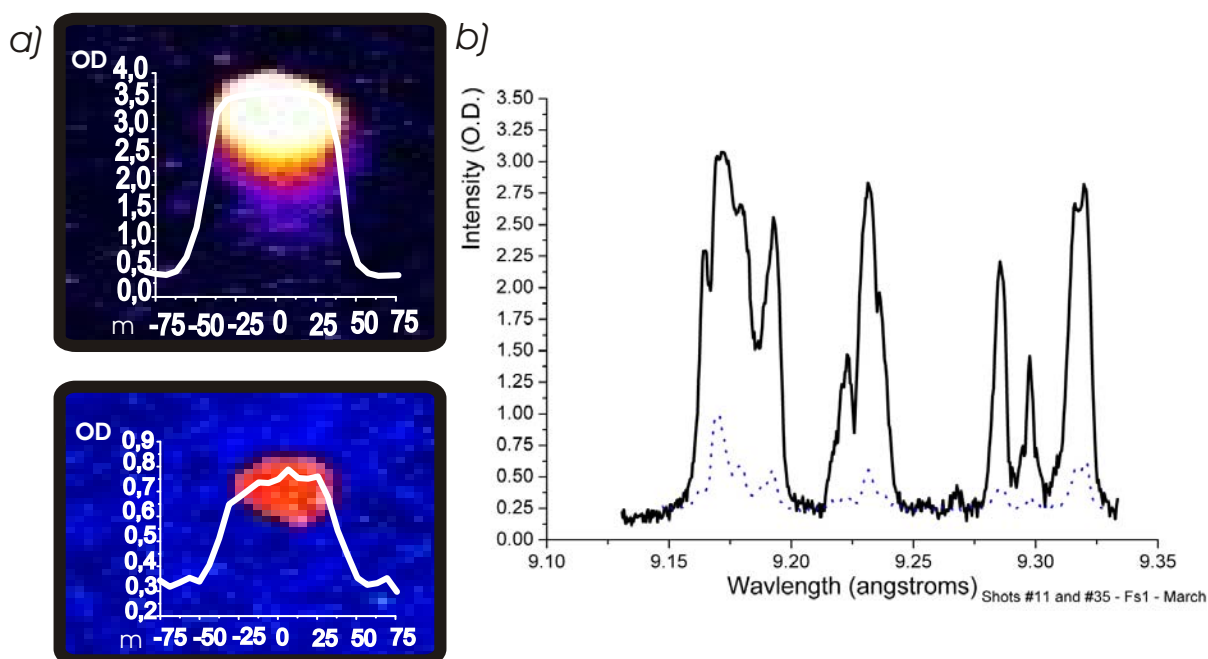


Figure 4.4: *a)* Ti pinholes for experiments with high fluency (upper) and low fluency. *b)* Fs1 spectra with the two laser fluxes. The dashed line corresponds to the low fluency case.

The study of plasma regions with a wavelength at maximum intensities outside the X ray spectrum was also made in order to find out if there are links among different plasma regions and their measured characteristics. In the case of jet formation, the cold plasma region that shines mainly in the visible region and the one that emits X ray spectra have similar behaviours: larger volumes appear in the visible streak images simultaneously with the X ray jet fingerprint (see Fig. 4.5).

The plasma velocity in the expansion direction, the dimension visible in the streak images, was estimated with the method described in paragraph 3.2.2, page 45. The cold plasma moves faster when the jet is formed, suggesting a linear dependence on the laser flux, as table 4.2 shows. The estimated velocity reached by the cold plasma when jets are formed is 1.8 times the value of the velocity at the lower laser flux, a value almost equal to the change in laser flux. Hence a correlation between the cold plasma expansion velocity and the laser flux was found, which suggests that such a correlation is maintained between the hot spot geometry and the cold plasma. But the last connection is to be further investigated because of the lack of data where only the laser flux changed, without the formation of X ray emitting jets.

| Laser flux (W/cm^2) | Cold ions mean velocity (Km/s) |
|---------------------------------------|--------------------------------|
| $2 \pm 1 \cdot 10^{13}$ | 44 |
| $4 \pm 1 \cdot 10^{13}$ | 78 |

Table 4.2: Plasma velocities at different laser flux values.

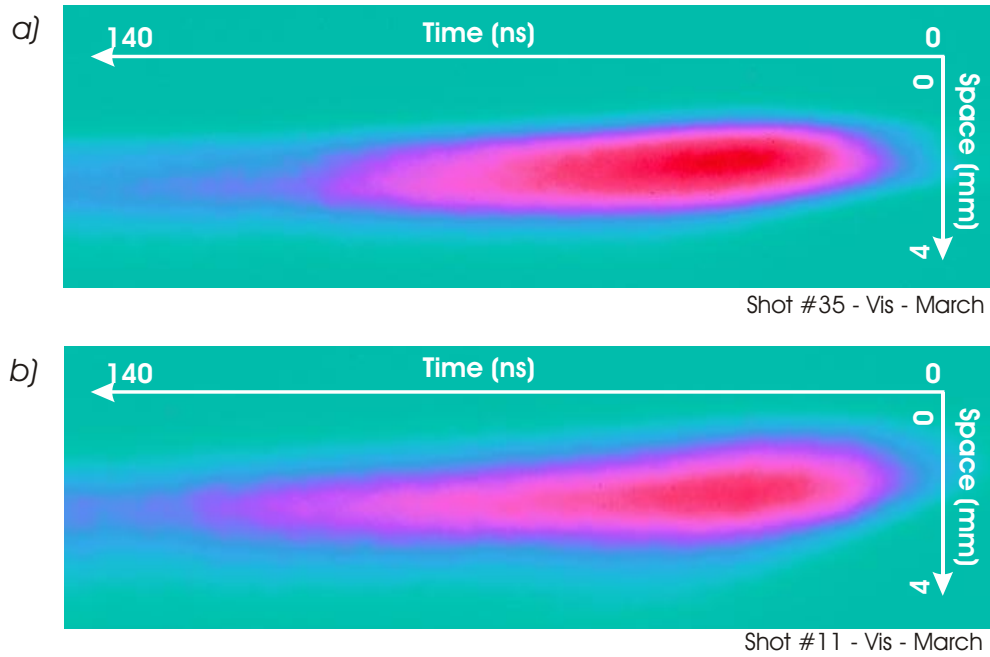


Figure 4.5: Visible streak images *a)* with $4 \cdot 10^{13} \text{ W/cm}^2$, and *b)* $2 \cdot 10^{13} \text{ W/cm}^2$.

The errors in the measurements used to calculate the laser flux (formula 3.2 in paragraph 3.1.2) give a relatively high final error of the determined laser flux. This inaccuracy does not allow for more detailed studies on the value of the laser flux threshold or the behaviour of the jet structure dependent with the laser flux.

4.1.3 Influence of the laser incidence angle

The influence of the laser beam incidence angle on jet generation is proved and quantified in this section. As it was stated in previous sections, the laser incidence angle is not a critical parameter for jet formation, but due to nonlinear effects that are angle dependent, it has a certain influence on the jet length. The two experimental setups described in the Section 3.3 on page 52 differ mainly in the laser beam incidence angle so a comparison of data obtained with these setups, the *normal* and the 45° , was made while keeping experimental parameters as similar as possible.

Thus, the value of the laser flux was $3 \pm 1 \cdot 10^{13} \text{ W/cm}^2$ for the *normal* setup and $2 \pm 1 \cdot 10^{13} \text{ W/cm}^2$ in the 45° case. The laser focus positions have been varied from 0.8 mm to 1.0 mm in the 45° and *normal* setups.

An augmented jet length is observed with the laser beam incidence angle of 45° . At the same time the maximum value of the emission recorded by the pinhole cameras decreases, as it can be seen in the traces of Fig. 4.6. The jet size was measured on pinhole images that had the same PP filter, the one with higher transmission properties, see page 42.

The jet size was measured from the expansion traces perpendicular to the target

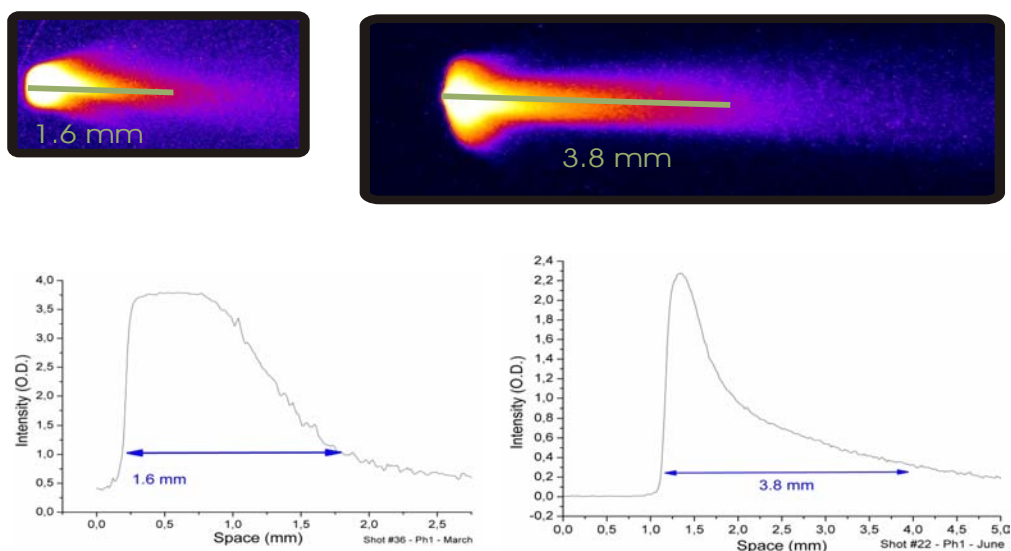


Figure 4.6: Pinhole images and traces with the jet lengths for the case of normal incidence (*left*) and 45° laser beam incidence (*right*)

surface obtained from the X ray pinhole images, taking care that the distance measured corresponds to the plasma expansion. The points at the beginning and end of the expansion with intensity levels 2 times larger than the noise levels were chosen to obtain the expansion length showed in Fig. 4.6. With this procedure the jet length varies from the 1.6 mm with the laser beam perpendicular to the target surface to the 3.8 mm measured when the orientation was at 45° , see Fig. 4.6.

The jet emission follows an exponential decay in one spatial dimension, observed from trace shapes, since the plotted OD units are proportional to light intensity. The parameters showed in the table 4.3 were calculated with the fitting routine of the ORIGIN program, based on a Levenberg-Marquardt algorithm. Fitting results confirm the observed increase in the jet size as the decay parameter $t1$ is larger when the laser beam angle of incidence is 45° .

Fit expression: $y = A1 * \exp(-x/t1) + y_0$

| Experiment setup | y_0 (O.D. values) | $A1$ (O.D. values) | $t1$ (mm) |
|------------------|---------------------|--------------------|-------------------|
| 45° | 0.077 ± 0.003 | 4.7 ± 0.1 | 1.28 ± 0.01 |
| <i>normal</i> | 0.446 ± 0.005 | 19.0 ± 0.4 | 0.540 ± 0.003 |

Table 4.3: Exponential decay fitting parameters value for both laser angles.

Using the visible streak data obtained in these two experiments the velocity of the cold ions was estimated with the method explained in the last paragraph of the section dedicated to the streak camera, page 45. Since the pulse duration is constant, a larger jet size implies a higher mean ion velocity. In fact, the velocity deduced from the streak images follows this trend: it is 64 km/s when the incidence angle is 45° and

40 km/s in the other case. These velocities allow us to make an estimation of the order of magnitude of the cold ions' mean kinetic energy: using the non relativistic expression and approximating the ion masses with the magnesium atomic mass. The values obtained are 0.5 keV for the faster case and 0.2 keV in the slower case. An apparent contradiction exists between these energies and the electron temperature, as the cold plasma has larger mean kinetic energies than the electron temperatures of the hot plasma radiating in the X ray range. But the calculated energies are for ions which move faster from the average of the overall ionic velocity distribution. Thus their energy is also far from the equilibrium one, i.e. higher than the mean obtained from electron temperature, as the data show.

Section 4.2 Influence of the laser beam divergence in the generated plasmas

The influence of the laser beam divergence on plasma characteristics and how this influence changes with other laser parameters is presented in this section. Experiments with the focus in front and behind the target surface were made to compare the differences arising from the focus positioning.

4.2.1 Non divergent laser beam

Using the *normal* incidence setup the relative position of the focus was always in front of the target. The distance of the focus to the target surface was varied from 0.5 to 7.5 mm. With these variations, the laser fluency and light intensity distribution change simultaneously, so any change on the plasma parameters must be assigned to both, without a clear separation of the two parameters.

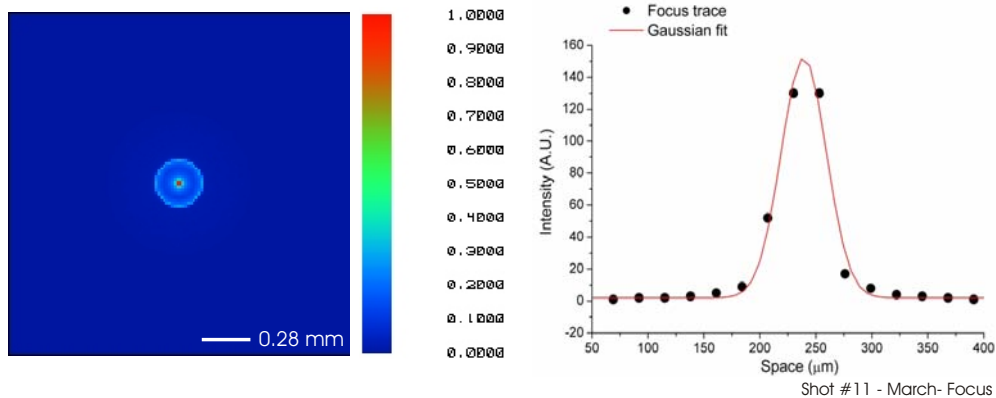


Figure 4.7: Light distribution at the target surface simulated with ZEMAX, left, and measured with the focus 0.5 mm in front of the target surface, right.

The laser fluency changed by one order of magnitude from $4 \pm 1 \cdot 10^{13}$ to $1 \pm 0.4 \cdot 10^{12}$

W/cm^2 with the increase of the distance, while the diameter of the light intensity distribution went from $46 \mu m$ to $740 \mu m$ when the focus moved from 0.5 to 7.5 mm. The spot size change was estimated from the ZEMAX simulations and measured with the CCD camera method described in paragraph 3.1.2, with good agreement between both methods.

To estimate the alteration of the light distribution at the target surface, this parameter is first presented together with the ZEMAX simulation in Fig. 4.7 for a distance from the focus to the target surface of 0.5 mm. The standard Gaussian energy distribution in the laser spot is clearly visible. When the distance from the focus to the target surface is increased to 7.5 mm, the laser light distribution on the target surface became annular, with an asymmetry that is not observed in the simulations (see Fig. 4.8).

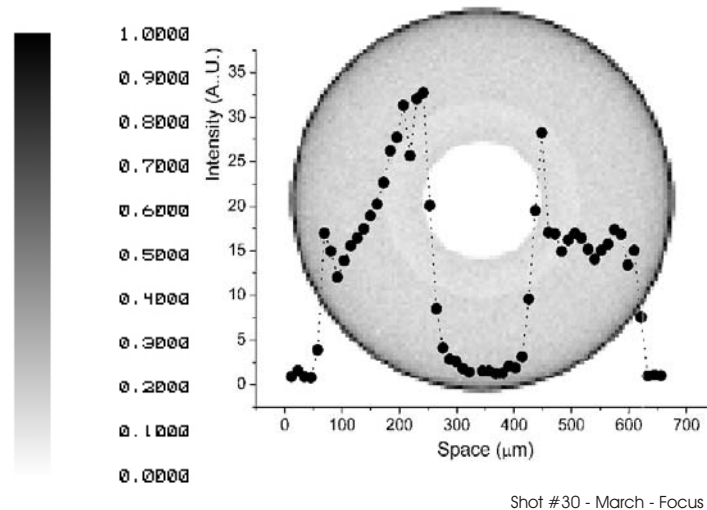


Figure 4.8: ZEMAX simulation (*scaled image*) and measured (*superimposed graph*) light distribution on target with 7.5 mm between focus and target surface.

Insight to the energy absorption processes can be obtained from the electronic temperature at the hot spot position using the satellite to resonance lines ratio. With the data from the Fs1 spectrometers, see Fig. 4.9, estimated temperatures are around 130 eV for both cases.

For a focus at 7.5 mm from the target surface, the electron temperature was 129 ± 19 eV while a value of 133 ± 20 eV is found for 0.5 mm from the target surface. From the observation of the spectra, two other characteristics are inferred: an increase in the plasma emission with the laser flux, and an electron density without appreciable difference between both cases. An almost consistent electron temperature irrespective of the distance between the focus and the target surface was also previously observed [63] but within a shorter range than the one tested here.

The increase in the X ray emission is associated with a growth of the number of ions on the higher energy state that allows them to emit in this wavelength range. It

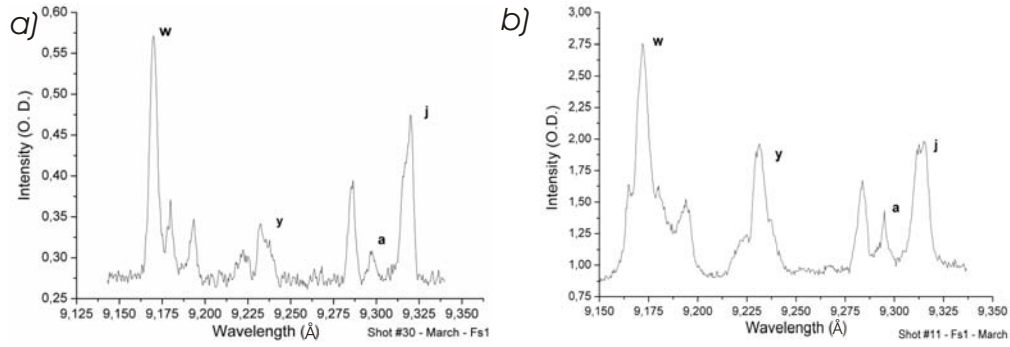


Figure 4.9: X ray spectra for both experimental situations: *a)* the focus at 7.5 mm and *b)* 0.5 mm in front of the target.

is not a proportionality relation, so the factor 4 of increase in the emission of the *j* satellite peak does not imply the same ratio for the plasma volume.

The ratio of the intercombination *y* to the resonant line *w* decreases when the electron density is reduced. The intensity ratio of *j* to *a* satellites behaves in the opposite way. As Table 4.4 shows, the difference between the two focusing situations is not significant, indicating the previously mentioned preservation of the electron density or a change too small to be measured with certainty.

| Laser fluency (W/cm^2) | <i>y-w</i> ratio | <i>j-a</i> ratio |
|--|------------------|------------------|
| $4 \pm 1 \cdot 10^{13}$ | 0.70 ± 0.07 | 1.4 ± 0.14 |
| $1 \pm 0.4 \cdot 10^{12}$ | 0.60 ± 0.06 | 1.5 ± 0.15 |

Table 4.4: Lines ratio

With a distance of 7.5 mm between the focus and the target surface, the hot spot was displaced from the target surface, as the FSSR spectra in Fig. 4.10 show.

The blurring on the (*b*) spectrum visible in this figure comes from an imprecise focusing of the FSSR. This can have two different causes. Either the FSSR are not correctly aligned or the X ray source is displaced. The FSSR alignment was made under the assumption that the X ray source was at the target surface and it does not change with the displacement of the focus. The observed blurred spectrum implies that the generation of X rays was not at the target surface, but away from it.

The visible streak camera images also show a larger emission from the cold plasma in the direction of observation, perpendicular to the plasma expansion. This widening implies that the region of cold plasma generation moved away from the target surface. In fact, since the source for cold plasma is the expansion of the hot plasma volume, if the hot spot was produced away from the target surface, there must be an expansion also on the visible streak camera image. The images from Fig. 4.11 (*a*) confirm this idea with the observed bump in the streak image of the plasma produced with the focus 7.5 mm in front of the target surface.

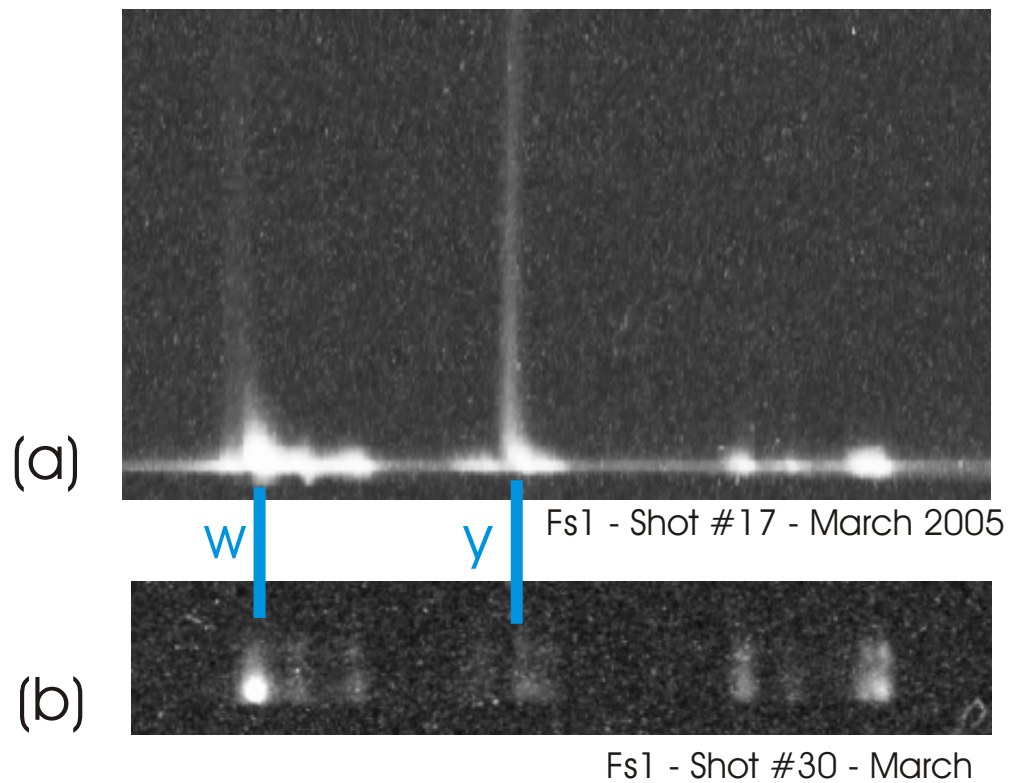


Figure 4.10: Fs1 spectra with the focus at *a)* 1.0 mm and *b)* 7.5 mm in front of the target with the resonant and intercombination lines emphasized.

The lifetime of the plasma does not change dramatically in the two situations, as the total emission time is similar. The emission duration is defined as the FWHM for the time during which light is emitted. The value changes from 49 to 43 ns when the focus distance goes from 7.5 to 1.0 mm. As it is visible in the same figure, there is an increase in the light emission for the lower flux, corresponding with the larger distance from the focus to the target surface. This behaviour is in opposition with the one observed for X ray emission. Light observed in the visible streak camera images is produced in two different ways, as discrete lines from electron transitions between low charged ion states, like Mg III, and Planck radiation. Both processes are temperature sensitive, so a temperature change exists for the cold plasma, in opposition to the behaviour of the plasma emitting in the X ray region. Whether the temperature increased or decreased with the increase in emission is not deducible from the data: the Planck curve displacement that may generate the increase could be caused by the movement of the emission maximum towards higher wavelengths and therefore higher temperatures or vice versa, depending upon the unknown initial position of this maximum.

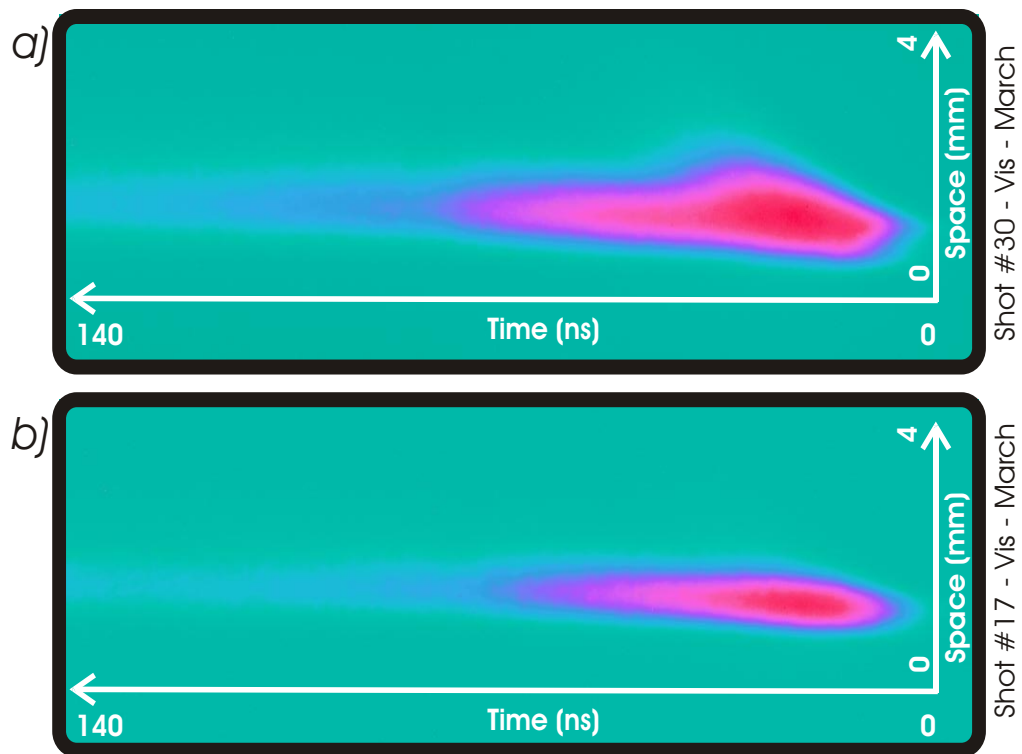


Figure 4.11: Visible streak images *a)* with focus at 7.5 , and *b)* 1.0 mm from the target surface.

4.2.2 Divergent laser beam

Measurements were made to observe the change in the plasma characteristics if the laser beam was divergent. To make the laser beam divergent, the last spatial filter in the *nhelix* chain was modified. Its last lens was displaced 1.5 mm from its original position, so that the laser beam diameter was increased from 50 to 65 mm before the focusing lens inside the target chamber. To avoid the creation of ion jets, the focus was always behind the target surface, with three different values for the distance from the target surface: 0.5, 1.0, and 1.8 mm.

Using these focus positions the focus shape was modified from a Gaussian shape to an annular one, as Fig. 4.12 illustrates, and the spot diameter varied from $69 \mu\text{m}$ with the focus 0.5 mm behind the target surface to $207 \mu\text{m}$ when the focus was 1.8 mm behind the target surface. These parameters permit the depicted laser fluency change with laser energy around 30 Joules. As the last lens of the *nhelix* chain was not corrected for aberrations, the Gaussian distribution profile was surrounded by an intensity ring caused by aberrations when the distance between the focus and the target surface increases. With the focus 1.00 mm behind the target the Gaussian is already transformed because of the ring that creates the step on the Gaussian wings. When the focus is 1.80 mm behind the target the ring becomes large enough to surround the Gaussian, with an intensity in the ring equivalent to the Gaussian peak.

The fluency values were calculated and are displayed in Fig. 4.12, varying from $7 \pm 2 \cdot 10^{13} \text{ W/cm}^2$ maximum for 0.5 mm to $7 \pm 3 \cdot 10^{12} \text{ W/cm}^2$ for 1.8 mm distance from the target surface.

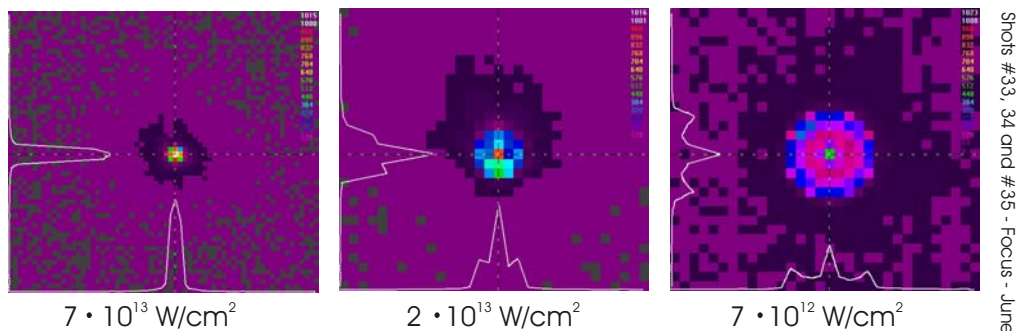


Figure 4.12: Focus shapes and fluencies with the focus 0.5 mm, *left*, 1.0 mm, *center* and 1.8 mm, *right* behind the target surface.

X ray diagnostics

The ratios of the He- γ to He- β line peaks, the $1s^2 \ ^1S_0 - 1s4p \ ^1P_1$ and $1s^2 \ ^1S_0 - 1s4p \ ^1P_1$ transitions respectively, see Table 3.2 on page 57 for denominations, did not vary significantly for the three focus placements, nor did the line widths. The highest change in the ratios was of the order of 10% and was measured for the ratio of the satellite to the resonant lines.

Within the frame of the collisional radiative model the intensity ratios of the satellites to He- γ can be linked to T_e variations, concretely the overlapped satellites $1s^2 2p \ ^2P_{3/2} - 1s2p(3P)4p \ ^2D_{5/2}$ and $1s^2 2p \ ^2P_{3/2} - 1s2p(3P)4p \ ^2D_{3/2}$ at wavelengths of 7.7279 and 7.7269 Å respectively. The population of the levels for the He- β and He- γ lines comes from different channels, as in the case of the the He- β line the recombination process does not count as much as collisional excitation. For the He- γ line the population of the excited level is achieved mainly through the recombination channel. Since the largest variation in the ratio of the satellite to the resonant lines is about 10%, the electron temperature variation is also small.

This lack of large differences in the electron density and temperature can be confirmed by analyzing the Fs1 spectra from Fig. 4.13, where experimental data and simulated spectra are shown. The lines represent the experimental values while the shadowed spectra are from simulations performed with the MARIA code [64] by using an electron temperature of 200 eV and an electron density of 10^{20} cm^{-3} .

On the other hand, the total emission shows a strong dependence on the laser fluency or light intensity distribution. The most intense line is always He- β , as the $1s3p - 1s^2$ transition that creates this line is easier to excite than the the He- γ that comes from the higher level $1s4p$. Therefore it is used here as a reference for intensity variations, which go from 10 300 counts for the highest fluency to 3 100 for the lowest

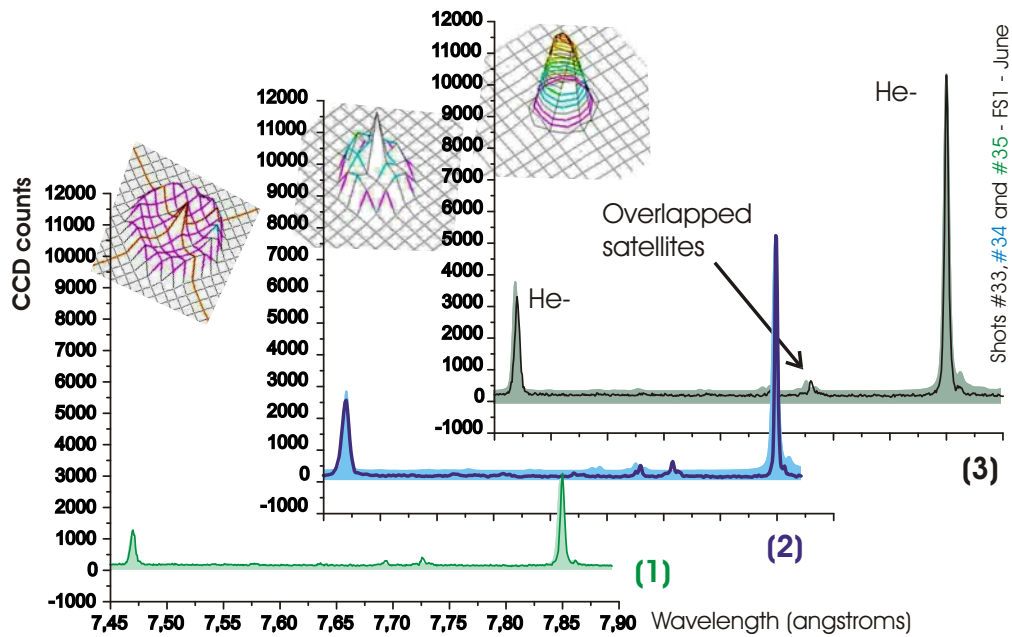


Figure 4.13: Fs1 spectra for the three focus position and shapes. Laser focus (1) 1.8 mm, (2) 1.0 mm and (3) 0.5 mm behind the target. Focus shapes are pictured in the superior left corner.

fluency, i.e. a ratio of 3.3 .

X ray pinhole images have no large variations in size, but in their total detected intensity: there is a small increase of the emission size as the fluency decreases (see Fig. 4.14) while the total emission enhances its maximum almost three times, from 0.45 OD achieved when the focus was closer to the target to 1.35 OD for the larger distance.

If the length of the plasma expansion in the direction perpendicular to the target surface is measured as the FWHM of the trace from Fig. 4.14, the expansion values go from the 0.47 ± 0.02 mm for 1.8 mm behind the target to 0.57 ± 0.03 mm for 0.5 mm.

The increase in the X ray emission recorded by the pinhole camera and the reduction in the Fs1 spectra have their origin in two complementary phenomena. Since the fluency is reduced, the plasma formed by He-like Mg ions is also reduced and the Fs1 spectra reflect such a fact, see Fig. 4.13. But with the change in the focus shape, the generation of colder ions is enhanced as recorded by the Ph1 pinholes. This leads to the apparent contradiction between larger volumes of plasma and less spectral emission from He-like ions.

To make a diagnostic of the colder plasma, again the visible streak camera is used and the mean ionic velocity is estimated from these images. The results are presented in Table 4.5.

An increase in velocity is observed when the fluency decreases and the distance between target surface and focus is increased. The mean kinetic energy was calculated from the velocities with the classical expression $E_k = (1/2)mv^2$ since the mean

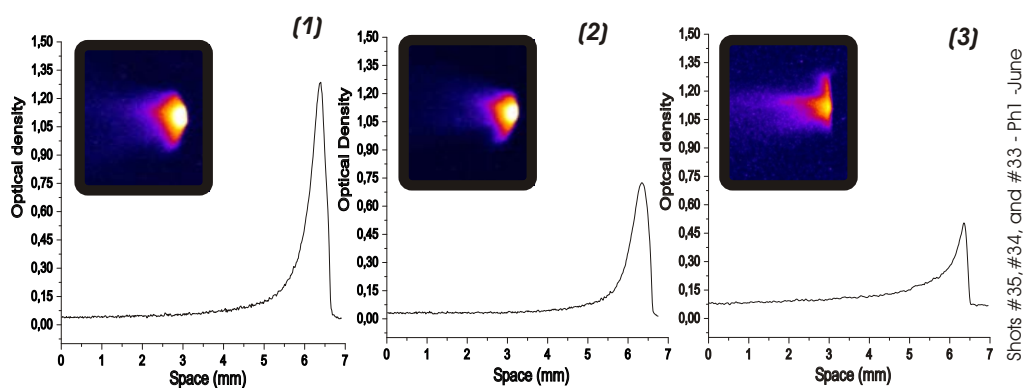


Figure 4.14: Ph1 images and horizontal profiles for different target surface to laser beam focus distances. (1) 1.8 mm, (2) 1.0 mm, and (3) 0.5 mm.

| Laser fluency (10^{13} W/cm ²) | Target surface - focus distance (mm) | Velocity (km/s) |
|---|--------------------------------------|-----------------|
| 7 ± 2 | 0.5 ± 0.1 | 60 ± 6 |
| 2 ± 0.8 | 1.0 ± 0.1 | 70 ± 7 |
| 0.7 ± 0.3 | 1.8 ± 0.1 | 90 ± 9 |

Table 4.5: Velocities for different distances between laser beam focus and target surface

ionic velocity is well below light velocity c . The kinetic energy varies from 0.92 keV for 1.8 mm, to the 0.51 keV for 0.5 mm behind the target surface. The apparent contradiction between the kinetic energy of the cold ions and the electron temperature of the hot plasma is, as mentioned before (see page 68), due to the place occupied by the measured cold ions in the velocity distribution function that is away from the equilibrium value.

Ultraviolet spectra results

The influence of the focus shape and laser fluency on the UV spectra with a divergent laser beam was studied. The spectral line relative intensities become similar as the distance between laser focus and target surface is increased, so the similarities in these ratios are correlated with the focus intensity profiles, see Fig. 4.15. At larger distances the intensity distribution develops the ring around the central peak, that makes the light spots very similar when the target surface is at 1.0 and 1.8 mm from the laser focus. As with X ray pinhole intensities, the total intensity increases inversely to the fluency, with a large step in the emission values correlated with the appearance of the ring.

The most intense spectrum occurs when the distance from the laser focus to the target surface is relatively large, in correspondence with the lowest fluency value of $7 \pm 2 \cdot 10^{12}$ W/cm². The increase in the line intensity is larger in transitions of Mg III at 218 nm and Mg V at 243 nm.

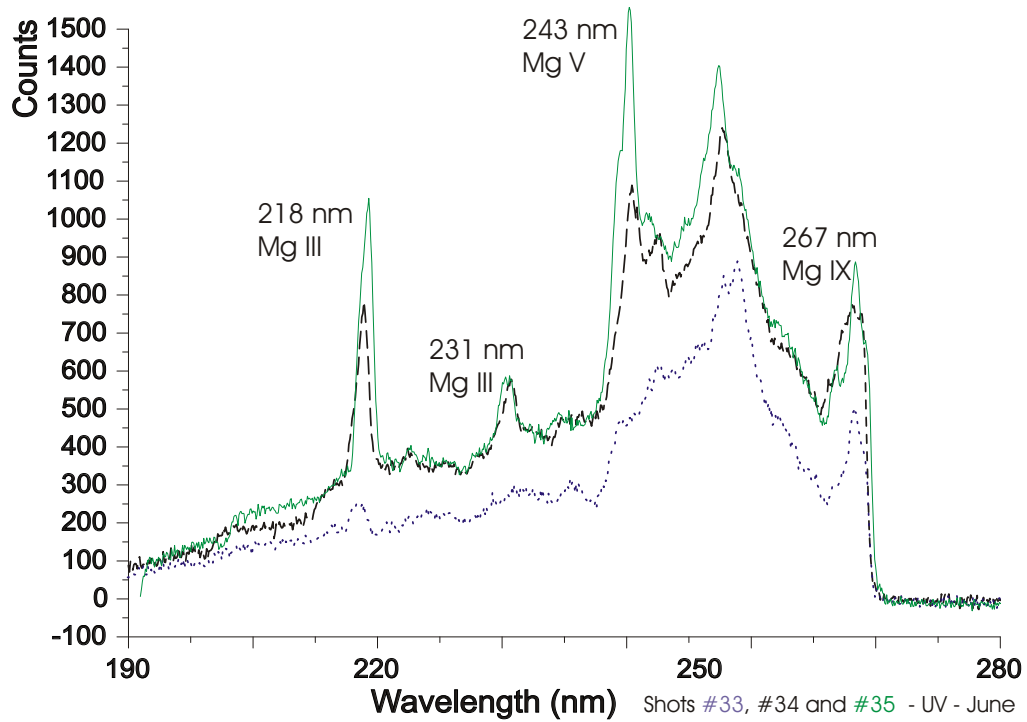


Figure 4.15: UV spectra dependence on the distance from target surface to focus of (—) 1.8, (---) 1.0, and (...) 0.5 mm.

Section 4.3 Analysis of the ultraviolet spectra

The ultraviolet spectral region was studied with the VM-502 spectrometer, adjusted to the wavelength interval between 200–270 nm. Spectra integrated in space and time, as the ones obtained in these experiments, are difficult to interpret, even more in the UV region, where many different transitions are possible at similar wavelengths.

4.3.1 Ultraviolet spectra calibration

Spectra calibration of the experimental data from the VM-502 has many difficulties. Usually, in the chosen bandwidth there are some standard lines used for the spectra calibrations; well known lines that help to look for the experimental dispersion of the device, always different to the theoretical one.

| Wavelength (nm) | Down level | Excited level | Transition probability (s^{-1}) |
|-----------------|----------------------|----------------------|-------------------------------------|
| 221.5 | $1s^23s \ ^2S_{1/2}$ | $1s^23p \ ^2P_{3/2}$ | $9.67e+07$ |
| 228.1 | $1s^23s \ ^2S_{1/2}$ | $1s^23p \ ^2P_{1/2}$ | $8.85e+07$ |

Table 4.6: Magnesium Li-like 3s-3p transitions.

The central lines of the present experiments were the Li-like transitions $1s^23s \rightarrow 1s^23p$, listed in Table 4.6 with some of their characteristics. Within them, no standard transition exists which can be used to start the calibration process. So the only re-

maining guide was the wavelength value.

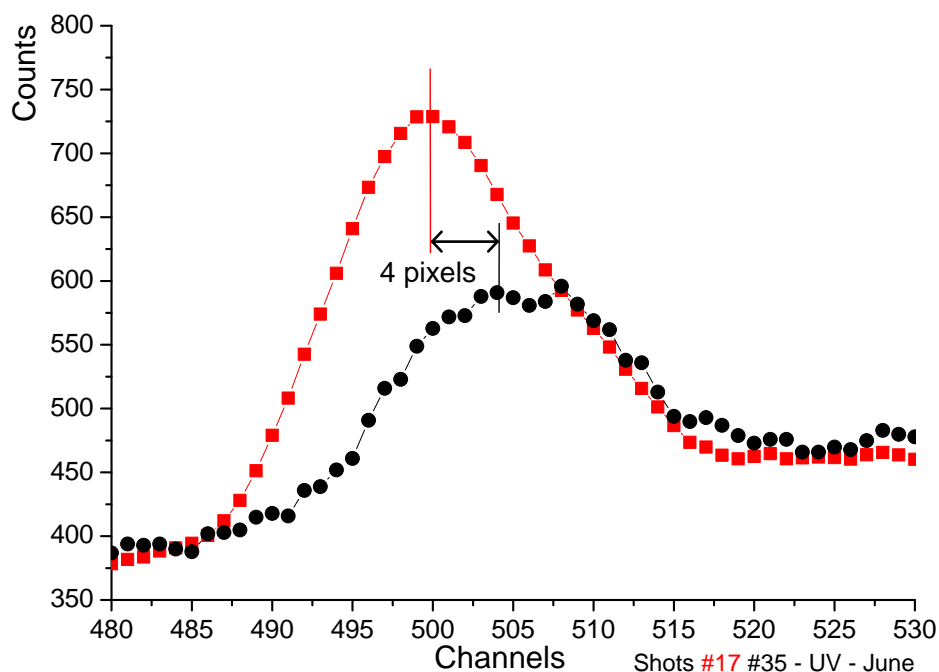


Figure 4.16: Peak displacement for two uncalibrated VM-502 spectra

Provided that the shape of the dispersion law is known, it is necessary to assign a wavelength to each peak in the calibration spectra. But this is difficult because of the large number of possible transitions for a certain wavelength interval. Moreover, line position varies from shot to shot hence the calibration must be done individually for each experiment by using previous calibrated spectra for first approximations. Figure 4.16 illustrates a shot to shot variation of four channels in the peak position of the same transition, a typical situation.

Transitions and their corresponding wavelengths are provided by on-line databases. During this work the data from the National Institute of Standards (NIST) [65] and from the International Science and Technology Center [66] were used. Candidate lines are numerous but the lack of adequate plasma models for this region of the spectrum makes the assignment of the observed peaks to transitions difficult. The maximum precision for the wavelength of a certain peak without prior knowledge of other lines is ± 1 nm. Table 4.7 makes clear how many transitions may be found within 1 nm.

The difference between the wavelengths of the two first transitions in the table is 0.1 nm, which is undetectable due to the error of the VM-502. Nevertheless the assignment of one or another ion charge state will lead to different conclusions, thus the wavelengths and transitions assigned in the different cases must be coherent. If one line is thought to come from low charge state ions, like Mg II or Mg III, no

| Ion | Wavelength (nm) | A (s ⁻¹) | Levels |
|-------|-----------------|----------------------|--|
| Mg IX | 221.07 | 7.99e+07 | 1s ² 2p3s ³ P ₁ - 1s ² 2p3p ³ D ₂ |
| Mg II | 221.14 | | 2p ⁵ (2P ⁰)3s3p(3P ⁰) ⁴ P _{3/2} - 2p ⁵ (2P ⁰)3p2(3P) ⁴ P _{5/2} |
| Mg X | 221.50 | 9.67e+07 | 1s ² 3s ² S _{1/2} - 1s ² 3p ² P _{3/2} |
| Mg II | 221.70 | 9.63e+04 | 2p ⁶ 4s ² S _{1/2} - 2p ⁶ 9p ² P _{1/2} |
| Mg IX | 221.81 | 1.05e+08 | 1s ² 2p3s ³ P ₂ - 1s ² 2p3p ³ D ₃ |

Table 4.7: Lines from the NIST dabase

lines from highly charged ions like Mg IX or Mg XI may be present. Transitions like 2p⁶4s - 2p⁶9p in Mg II at 221.70 nm cannot be seen simultaneously with those like 1s²2p3p - 1s²2p3d in Mg IX at 218.13 nm.

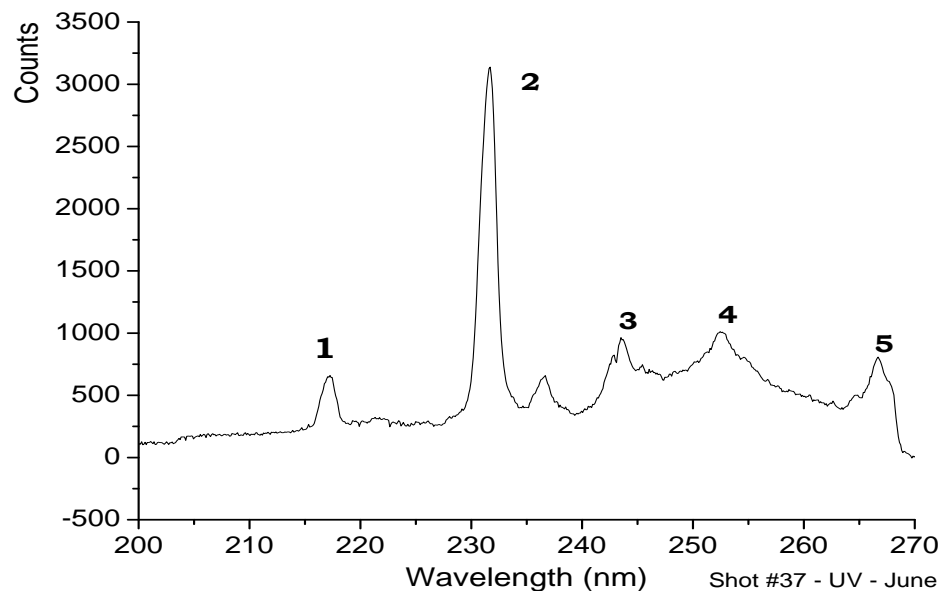


Figure 4.17: Ultraviolet spectrum used as calibration example.

As an example the calibration of the spectrum of Fig. 4.17 is presented here. To obtain the spectrum, the divergent laser beam was focused 1.00 mm in front of the target surface, in the 45° configuration. The largest peak recorded in this experiment is number 2 from Fig. 4.17. Using the NIST database as primary information source, the following lines are assigned to the observed peaks:

Peak 1 At 217.7 nm the transition $2s^2 2p^5 3s \ ^1P_1 - 2s^2 2p^5 3p \ ^1D_2$ from Mg III. Other transitions from the same excited ion levels, except the fine structure, are present at different positions in the same spectrum, thus this assignment is reasonable.

Peak 2 The large peak at 231.8 nm is thought to be produced by the combination of two transitions: $2s^2 2p^5 3s \ ^1P_1 - 2s^2 2p^5 3p \ ^3D_2$ at 231.8 nm from Mg III and $2s^2 2p^3 (2P^0) 3d$

${}^3P_0 - 2s^22p^4(4P)3s {}^3P_1$ at 231.6 nm from Mg V. The ions have relatively close charge states and the transitions have large oscillator strengths.

Peak 3 A Mg V transition with a wavelength of 243 nm, and it is the same level that enhances the intensity in the 231 nm: $2s^22p^3(2P^0)3d {}^3P_2 - 2s^22p^4(4P)3s {}^3P_2$, with the difference only in the fine structure.

Peak 4 Another fine structure peak from Mg III at 252.9 nm between the levels $2s^22p^53s {}^3P_0 - 2s^22p^53p {}^3S_1$.

Peak 5 A very intense Mg I transition corresponding to the levels $3s3p - 3s7d$ with wavelength of 267 nm is assigned to this peak.

4.3.2 Influence of the laser beam divergence

The emission in the UV range has been studied in relation to the laser beam divergence. To change the laser beam from the non-divergent to the divergent situation, the lens in the last spatial filter was defocused as it is described in paragraph 4.2.2. The relative position of the laser focus with respect to the target surface covered all possibilities: in front, at the target surface and behind it.

Large differences in the laser fluency and spot shape were obtained by varying the distance between focus and target surface from 1.5 mm behind the target to 0.5 mm in front of it.

With the divergent laser beam, the UV emission was increased for all focus positions but with large variations between them (see Fig. 4.18). Stronger emission is produced with the focus in front of the target surface, with a ratio of the divergent to the non-divergent cases of the order of 3 for the line at 241 nm. This is equal to the observed ratio with the focus at the target surface. The largest ratio is produced with the focus 1.5 mm behind the target surface, where the ratio between the divergent case to the non-divergent case is 6.

Normalized spectra were also compared to see the variation in their relative lines ratio. To normalize the spectra, different lines were chosen trying to bring the maximum intensity close to 1. When the focus was at 0.5 mm in front of the target surface the transition at 231 nm was assigned the maximum value, since it is one of the most intense lines in this spectrum, as graph (a) in Fig. 4.19 shows. For the opposite focus position, at 1.5 mm behind the target, the chosen transition was the line at 241 nm from Mg III.

The general features of the spectra allow for a differentiation in the changes associated with the laser beam divergence when the focus is in front or behind the target. With the focus in front of the target, the UV spectra show a strong dissimilarity in the intensity of the transitions from Mg III at 247 nm and from Mg I at 257 nm, since

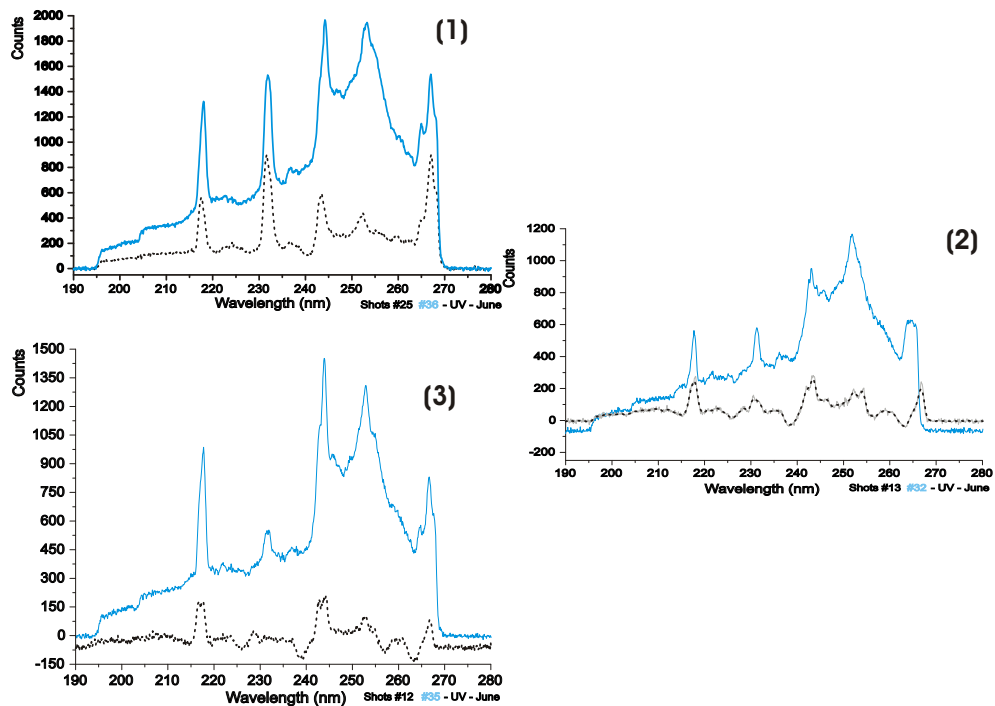


Figure 4.18: UV spectra for the three focus-target positions. — with divergent and ... non-divergent laser beam. (1) focus 0.5 mm in front of the target surface, (2), at the surface and (3) focus 1.5 mm behind the target surface.

these lines are much stronger in the divergent beam case. If the focus was behind the target the spectra did not differ much, the largest variation being in the line at 253 nm.

The normalized intensities show larger differences when the maximum intensity ratio variation is less pronounced, i.e., with the focus 0.5 mm in front of the target. If the focus is behind the target, the situation is reversed as Fig. 4.19 shows. There, the line ratios are not so different for the two laser divergences. Nevertheless the total emission increases 6 times with the divergent laser beam.

Concerning the cold plasma generation measured by the total UV emission, the laser beam parallelism is an important factor, as the previous paragraphs at page 79 state. But there is less influence on the expanded plasma characteristics, since the normalized spectra do not differ so much.

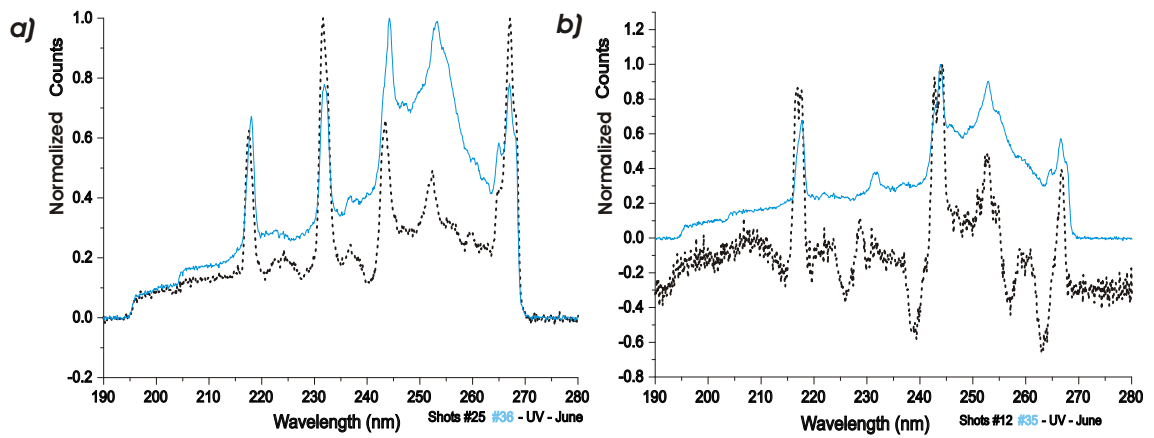


Figure 4.19: Normalized spectra with — non parallel and ... parallel laser beam with the focus *a)* 0.5 mm in front of the target surface and *b)* 1.5 mm behind the target surface.

Chapter 5

Conclusions and outlook

In this chapter the main conclusions from the experimental results are presented, with a compendium of the jet characteristics. Also important properties of the laser produced plasmas are compiled here, with a final section dedicated to an outlook on future possibilities.

Conclusions

The formation of jet structures of highly charged magnesium ions has been achieved at the *nhelix* laser system and spatially characterized over a large range of laser parameters. The last lens of the laser beam must be focused 0.5 to 1.0 mm in front of the target surface in order to obtain the jets, that had a maximum estimated kinetic energy of 9 keV/ion with a low jet divergence, less than 10° . Cylindrical highly ionized plasma volumes with a plasma aspect ratio of 4.5 can be maintained over the laser pulse time as the quasi-static situation is reached within the first nanosecond of the laser pulse.

The ions that appear in these jets are highly charged states, up to Li-like ones, as these are the only ions that may emit in the X ray range that the pinhole cameras observe. The expansion of He-like ions that emit He- α , He- β and He- γ lines as observed by the FSSR also confirm contributions from these charged states.

The electron temperature of the hot X ray radiating spots seemed larger in the presence of the jets, but the error of its estimation does not permit a definitive conclusion. Apart from the characteristic laser focusing necessary to obtain the jets, there is a threshold value for the laser flux: at $2 \cdot 10^{12}$ W/cm² the plasma is produced, but the jets are not formed. Jet production was observed with two times higher laser flux and other experimental parameters unaltered, so the threshold value lies between 2 and $4 \cdot 10^{12}$ W/cm².

Emission in the X ray range and therefore the highly charged ion density increases when the laser conditions lead to jet formation, regardless of the lower fluency caused by the movement of the lens focus from the target surface to positions in front of it.

Comparison of diagnostic tools in different spectral regions had allowed for the

study of very different plasma regions and relations were found between them. The cold plasma expansion is larger with the presence of the jets in the X ray domain. The colder region mainly emits in the visible and ultraviolet spectral regions and was studied with the ultraviolet spectrometer and the visible streak camera. A hotter region emits in the X ray range and was recorded with the FSSR spectrometers and the pinhole cameras. Electron temperatures did not vary significantly with the focal shape and laser flux within the investigated laser parameters. On the contrary, the recorded geometry of the X ray region had much larger variations. Both facts lead to conclude that the plasma expansion geometry is weakly linked to the energy equilibrium.

Outlook

Experimental parameters needed to obtain jets of highly charged magnesium ions have been determined within this work. Nevertheless, the physical process leading to the jet formation is still not fully understood. A possible explanation for these phenomena is the heating of the expanding plasma when it reaches the focus position in front of the target. Due to the quasi-static state the plasma may contain magnetic fields able to collimate it, leading to the jet shape observed in pinhole images, while the heating at the focus position will account for the longer expansion observed. Such collimation has been observed with external magnetic fields at much lower laser fluxes, 10^8 W/cm^2 [67].

Dependences of the plume geometry on the ion charge were found for lower fluxes, from 10^6 to 10^9 W/cm^2 , in works related to the characterization of laser plasma ion sources for industrial applications [68]. They show a strong dependence of the mean ion charge on the focus position and a maximum ion production with the focus in front of the target surface. At *nhelix* fluencies, the ion production was also increased with the focus of the laser beam placed in front of the target surface, when the jets appear, so a extension of the cited work was achieved.

A theoretical model able to reproduce these results is a task for future work, with more experiments to confirm the theoretical predictions. The extension of these results to thin targets should be straightforward, provided the adequate laser flux, as the laser-plasma interaction happens in a thin sheath of the order of nanometers and the target sheaths with a thickness of micrometers used at the GSI are thus thick enough.

Bibliography

- [1] R. A. Snavely, M. H. Key, S. P. Hatchett, T. E. Cowan, M. Roth, , T. W. Philips, M. A. Stoyer, E. A. Henry, T. C. Sangster, M. S. Singh, S. C. Wilks, A. MacKinnon, A. Offenberger, D. M. Pennington, K. Yasuike, A. B. Langdon, B. F. Lasinski, J. Johnson, M. D. Perry, and E. M. Campbell. *Intense High-Energy Proton Beams from Petawatt-Laser Irradiation of Solids*. PHYSICAL REVIEW LETTERS, 85(14):2945–2948, October 2000.
- [2] Stephen P. Hatchett, Curtis G. Brown, Thomas E. Cowan, Eugene A. Henry, Joy S. Johnson, Michael H. Key, Jeffrey A. Koch, A. Bruce Langdon, Barbara F. Lasinski, Richard W. Lee, Andrew J. Mackinnon, Deanna M. Pennington, Michael D. Perry, Thomas W. Philips, Markus Roth, T. Craig Sangster, Mike S. Singh, Richard A. Snavely, Mark A. Stoyer, Scott C. Wilks, and Kazuhito Yasuike. *Electron, Photon, and Ion Beams from the Relativistic Interaction of Petawatt Laser Pulses with Solid Targets*. PHYSICS OF PLASMAS, 7(5):2076–2082, May 2000.
- [3] H. Schwoerer, S. Pfotenhauer, O. Jäckel, K.-U. Amthor, B. Liesfeld, W. Ziegler, R. Sauerbrey, K. W. D. Ledingham, and T. Esirkepov. *Laser-Plasma Acceleration of Quasi-Monoenergetic Protons from Microstructured Targets*. NATURE, 439:445–448, January 2006.
- [4] J. Stamper and B. H. Ripin. *Faraday-Rotation Measurements of Megagauss Magnetic Fields in Laser Produced Plasmas*. PHYSICAL REVIEW LETTERS, 34:138–141, January 1975.
- [5] S.J. Gitomer, R. D. Jones, F. Begay, A.W. Ehler, J.F. Kephart, and R. Kristal. *Fast Ions and Hot Electrons in the Laser-Plasma Interaction*. PHYSICS FLUIDS, 29(8):2679–2688, August 1986.
- [6] P. Maier-Komor, G. Dollinger, and R. Krücken. *Preparation and Investigation of Thick Carbon Foils Prepared by Laser Plasma Ablation Deposition*. NUCLEAR INSTRUMENTS AND METHODS IN PHYSICS RESEARCH A, 561:4–10, 2006.
- [7] Julian Knipp and Edward Teller. *On the Energy Loss of Heavy Ions*. PHYSICAL REVIEW, 59:659–669, April 1941.

- [8] M. Roth, C. Stöckl, W. Süß, O. Iwase, D. O. Gericke, R. Bock, D. H. H. Hoffmann, M. Geissel, and W. Seelig. *Energy Loss of Heavy Ions in Laser-Produced Plasmas*. EUROPHYSICS LETTERS, 50(1):28–34, April 2000.
- [9] D. L. Matthews, P. L. Hagelstein, M. D. Rosen, M. J. Eckart, N. M. Ceglio, A. U. Hazi, H. Medeck, B. J. MacGowan, J. E. Trebes, B. L. Whitten, E. M. Campbell, C. W. Hatcher, A. M. Hawryluk, R. L. Kauffman, L. D. Pleasance, G. Rambach, J. H. Scofield, G. Stone, and T. A. Weaver. *Demonstration of a Soft X-Ray Amplifier*. PHYSICAL REVIEW LETTERS, 54(2):110–114, January 1985.
- [10] F. B. Rosmej, D. H. H. Hoffmann, W. Süß, M. Geissel, P. Pirzadeh, M. Roth, W. Seelig, A. Ya. Faenov, I. Yu. Skobelev, A. I. Magunov, T. A. Pikuz, R. Bock, U. N. Funk, U. Neuner, S. Udrea, A. Tauschwitz, N. A. Tahir, B. Yu. Sharkov, and N. E. Andreev. *Observation of MeV Ions in Long-Pulse, Large-Scale Laser-Produced Plasmas*. JOURNAL OF EXPERIMENTAL AND THEORETICAL PHYSICS LETTERS, 70(4):270–276, August 1999.
- [11] F. B. Rosmej, D. H. H. Hoffmann, W. Süß, A. E. Stepanov, Yu. A. Satov, Yu. B. Smakovskii, V. K. Roerich, S. V. Khomenko, K. N. Makarov, A. N. Starostin, A. Ya. Faenov, I. Yu. Skobelev, A. I. Magunov, M. Geißel, P. Pirzadeh, W. Seelig, T. A. Pikuz, R. Bock, T. Letardi, F. Flora, S. Bollanti, P. Di Lazzaro, A. Reale, A. Scafati, G. Tomassetti, T. Auguste, P. D’Oliveira, S. Hulin, P. Monot, and B. Yu. Sharkov. *The Generation of Fast Particles in Plasmas Created by Laser Pulses with Different Wavelengths*. JOURNAL OF EXPERIMENTAL AND THEORETICAL PHYSICS, 94(1):60–72, 2002.
- [12] Francis R. Chen. *Plasma Physics and Controlled Fusion*, volume II. Plenum Press, New York, 233 Spring Street, New York, N.Y. 10013, 1988.
- [13] D. A. Frank-Kamenetskii. *Plasma. The Fourth State of Matter*. MACMILLAN PRESS, LTD, New York, 1972.
- [14] Alvin Seiff, Donn B. Kirk, Tony C. Knight, John D. Mihalov, Robert C. Blanchard, Richard E. Young, Gerald Schubert, Ulf Von Zahn, Gerald Lehmacher, Frank S. Milos, and Jerry Wang. *Structure of Jupiter: Galileo Probe Measurements*. SCIENCE, 272:844–845, May 1996.
- [15] Hasso B. Niemann, Sushil K. Atreya, George R. Carignan, Thomas M Donahue, John A. Haberman, Dan N. Harpold, Richard E. Hartle, Donald M. Hunten, Wayne T. Kasprzak, Paul R. Mahaffy, Tobias C. Owen, Nelson W. Spencer, and Stanley H. Way. *The Galileo Probe Mass Spectrometer: Composition of Jupiter’s Atmosphere*. SCIENCE, 272:846–847, 1996.

- [16] Edward T. Lu and Russel J. Hamilton. *Avalanches and the Distribution of Solar Flares*. THE ASTHROPHYSICAL JOURNAL, 380:L89–L92, October 1991.
- [17] Mario Livio. *Astrophysical Jets a Phenomenological Examination of Acceleration and Collimation*. PHYSICS REPORTS, 311:225–245, 1999.
- [18] Bruce A. Remington, David Arnett, R. Paul Drake, and Hideaki Takabe. *Modeling Astrophysical Phenomena in the Laboratory with Intense Lasers*. SCIENCE, 284:1488–1493, May 1999.
- [19] Francis. F. Chen. *Industrial Applications of Low-Temperature Plasma Physics*. PHYSICS OF PLASMAS, 2(6):2164–2175, June 1995.
- [20] Masao Ushio. *Arc Discharge and Electrode Phenomena*. PURE & APPLIED CHEMISTRY, 60(5):809–814, 1988.
- [21] H. Alfvén, L. Linberg, and P. Mitlid. *Experiments with Plasma Rings*. JOURNAL OF NUCLEAR ENERGY, PART C: PLASMA PHYSICS, 1:116–120, 1960.
- [22] *Brief Introduction to the Q-Machine*. <http://www.physics.uiowa.edu/xplasma/Qmachine.html>, 2006.
- [23] J. E. Balmer and T. P. Donaldson. *Resonance Absorption of 1.06- μ M Laser Radiation in Laser-Generated Plasma*. PHYSICAL REVIEW LETTERS, 39(17):1084–1087, October 1977.
- [24] S. Yu. Gus'kov, N. N. Demchenko, K. N. Makarov, S. G. Nishchuk, T. A. Pikuz, Yu. A. Satov, I. Yu. Skobelev, Yu. B. Smakovskii, A. Ya. Faenov, S. V. Khomenko, and B. Yu. Sharkov. *Influence of Angles of Incidence of Laser Radiation on the Generation of Fast Ions*. JOURNAL OF EXPERIMENTAL AND THEORETICAL PHYSICS LETTERS, 73(12):655–660, 2001.
- [25] A. R. Piriz and R. F. Portugues. *Landau–Darrieus Instability in an Ablation Front*. PHYSICS OF PLASMAS, 10(6):2449–2456, June 2003.
- [26] S.E. Bodner, D. G. Colombant, J. H. Gardner, R. H. Lehmberg, S. P. Obenschain, L. Phillips, A. J. Schmitt, J. D. Sethian, R. L. McCrory, W. Seka, C. P. Verdon, J. P. Knauer, B.B. Afeyan, and H. T. Powell. *Direct-Drive Laser Fusion: Status and Prospects*. PHYSICS OF PLASMAS, 5(5):1901–1918, May 1998.
- [27] A. Sh. Abdullaev, Yu. M. Aliev, and V. Yu. Bychenkov. *Magnetic Instability of Laser-Produced Plasma and Spontaneous Generation of Magnetic Fields*. PHYSICS LETTERS, 71 A(1):63–65, April 1979.

- [28] Rémy Fabbro, Claire Max, and Edouard Fabre. *Planar Laser-Driven Ablation: Effect of Inhibited Electron Thermal Conduction*. PHYSICS OF FLUIDS, 28(5):1463–1481, May 1985.
- [29] A. Caruso, A. de Angelis, G. Gatti, R. Gratton, and S. Martelluci. *Change in the Scaling Laws for Laser Produced Plasmas Through the Critical Regime*. PHYSICS LETTERS, 35A(4):279–280, June 1971.
- [30] A. Caruso and R. Gratton. *Some Properties of the Plasma Produced by Irradiating Light Solids by Laser Pulses*. PLASMA PHYSICS, 10:867–877, 1968.
- [31] Clare E. Max, C. F. McKee, and W. C. Mead. *A Model for Laser Driven Ablative Implosions*. PHYSICS OF FLUIDS, 23(8):1620–1645, August 1980.
- [32] J. Benavit. *Collisionless Plasma Expansion Into a Vacuum*. PHYSICS OF FLUIDS, 22(7):1384–1392, July 1979.
- [33] Th. Müller, B. K. Sinha, and K. P. Rohr. *Direction-Selective Free Expansion of Laser Produced Plasmas from Planar Targets*. PHYSICAL REVIEW E, 67(26415), 2003.
- [34] S. N. Srivastava and K. Rohr. *Scaling Law of Angular Emission Distributions of Laser Ablated Particle Pulses from Monoatomic and Compound Targets*. BEAM INTERACTIONS WITH MATERIALS & ATOMS, 237:497–506, 2005.
- [35] A. Neogi and R. K. Thareja. *Dynamics of Laser Produced Carbon Plasma Expanding in a Nonuniform Magnetic Field*. JOURNAL OF APPLIED PHYSICS, 85(2):1131–1136, January 1999.
- [36] H. C. Pant, V. N. Rai, and M. Schukla. *Behaviour of Expanding Laser Produced Plasma in a Magnetic Field*. PHYSICA SCRIPTA, T75:104–111, 1998.
- [37] I. I. Sobelman, L. A. Vainshtein, and E. A. Yukov. *Excitation of Atoms and Broadening of Spectral Lines*. Springer Series in Chemical Physics. Springer-Verlag, 1981.
- [38] Andrea Thum-Jaeger, Binoy K. Sinha, and Klaus P. Rohr. *Time of Flight Measurements on Ion-Velocity Distribution and Anisotropy of Ion Temperatures in Laser Plasmas*. PHYSICAL REVIEW E, 63(16405), 2000.
- [39] J. A. Stamper, K. Papadopoulos, R. N. Sudan, S. O. Dean, and E. A. McLean. *Spontaneous Magnetic Fields in Laser-Produced Plasmas*. PHYSICAL REVIEW LETTERS, 26:1012–1015, April 1971.
- [40] T. J. M. Boyd, G. J. Humphreys-Jones, and D. Cooke. *Structure of Magnetic Fields Generated in Laser Produced Plasmas*. PHYSICS LETTERS, 88A(3):140–143, March 1982.

- [41] D. A. Tidman and J. A. Stamper. *Role of Magnetic Fields in Suprathermal Particle Generation by Laser-Produced Plasmas*. APPLIED PHYSICS LETTERS, 22(10):498–499, May 1973.
- [42] Piergiorgio Nicolosi and Giuseppe Tondello. *Satellite Spectra from Laser-Produced Plasmas of Be, C, N, and O in He-Like and Li-Like Configurations*. JOURNAL OF THE OPTICAL SOCIETY OF AMERICA, 67(8):1033–1039, August 1977.
- [43] I. Yu. Skobelev, A. Ya. Faenov, T. A. Pikuz, A. I. Magunov, F. Flora, S. Bollanti, P. DiLazzaro, D. Murra, A. Reale, L. Reale, G. Tomassetti, A. Ritucci, G. Petrocelli, S. Martellucci, N. Lisi, and F. B. Rosmej. *Spectral Transitions from the Rydberg Autoionization States of a Li-Like Mg X Ion*. JOURNAL OF EXPERIMENTAL AND THEORETICAL PHYSICS, 95(3):421–428, 2002.
- [44] A. H. Gabriel and T. M. Paget. *Measurement and Interpretation of Dielectronic Recombination Satellite Line Intensities*. JOURNAL OF PHYSICS B: ATOMIC AND MOLECULAR PHYSICS, 5:673–685, March 1972.
- [45] A. H. Gabriel. *Dielectronic Satellite Spectra for Highly-Charged Helium-Like Ion Lines*. MON. NOT. R. ASTR. SOC., 160:99–119, 1972.
- [46] Henry Van Regemorter. *Rate of Collisional Excitation in Stellar Atmospheres*. ASTROPHYSICAL JOURNAL, 3:906–915, November 1962.
- [47] G. Schaumann, M.S. Schollmeier, G. Rodriguez Prieto, A. Blazevic, E. Brambrinck, M. Geissel, S. Korostiy, P. Pirdazeh, M. Roth, F.B. Rosmej, A.YA. Faenov, T.A. Pikuz K. Tsigutkin, Y. Maron, N.A. Tahir, and D.H.H. Hoffmann. *High Energy Heavy Ion Jets Emerging from Laser Plasma Generated by Long Pulse Laser Beams from the NHELIX Laser System at GSI*. LASER AND PARTICLE BEAMS, 23:503–512, 2005.
- [48] Hamamatsu Photonics. *Guide to Streak Cameras*, 1994.
- [49] A. A. Berezhnoy, N. Hasebe, M. Kobayashi, G. Michael, and N. Yamashita. *Petrologic Mapping of the Moon Using Fe, Mg, and Al Abundances*. ADVANCES IN SPACE RESEARCH, 37:45–49, 2006.
- [50] Q. Qian, T. A. Tyson, W. A. Caliebe, and C.-C. Kao. *High-Efficiency High-Energy-Resolution Spectrometer for Inelastic X-Ray Scattering*. JOURNAL OF PHYSICS AND CHEMISTRY OF SOLIDS, 66:2295–2298, 2005.
- [51] A. Thorne, U. Litzén, and S. Johansson. *Spectrophysics*. Springer-Verlag, Heidelberg, 1999.
- [52] *Operating Instructions ARC Model VM-502*.

- [53] F. Venneri and G. Gerdin. *Time-Resolved Temperature Measurement of a Pinch Plasma Using the Dispersive X-Ray Analysis of the Continuum Emission*. REVIEW OF SCIENTIFIC INSTRUMENTS, 61(12):3797–3806, December 1990.
- [54] A. Ya. Faenov, S.A. Pikuz, and A.I. Erko. *High-Performance X-Ray Spectroscopic Devices for Plasma Microsources Investigations*. PHYSICA SCRIPTA, 50:333–338, 1994.
- [55] I. Yu. Skobelev, A. Ya. Faenov, B. A. Bryunetkin, V. M. Dyakin, T.A. Pikuz, S. A. Pikuz, T.A. Shelkovenko, V.M. Romanova, and A. R. Mingaleev. *Investigating the Emission Properties of Plasma Structures with X-Ray Imaging Spectroscopy*. JOURNAL OF EXPERIMENTAL AND THEORETICAL PHYSICS, 81(4):692–718, 1995.
- [56] B. L. Henke, S. L. Kwok, J. Y. Uejio, H. T. Yamada, and G. C. Young. *Low-Energy X-Ray Response of Photographic Films. I. Mathematical Models*. JOURNAL OF THE OPTICAL SOCIETY OF AMERICA, 1(6):818–827, December 1984.
- [57] B. L. Henke, J. Y. Uejio, G. F. Stone, C. H. Dittmore, and F. G. Fujiwara. *High-Energy X-Ray Response of Photographic Films: Models and Measurement*. JOURNAL OF THE OPTICAL SOCIETY OF AMERICA B, 3(11):1540–1550, November 1986.
- [58] L. A. Vainshtein and U.I. Safranova. *Wavelengths and Transition Probabilities of Satellites to Resonance Lines of H- and He-Like Ions*. ATOMIC DATA AND NUCLEAR DATA TABLES, 21:49–68, January 1978.
- [59] J.L. Bobin. *High Intensity Laser Plasma Interaction*. PHYSICS REPORTS (REVIEW SECTION OF PHYSICS LETTERS), 122(4):173–274, 1985.
- [60] C. Stöckl, O. Boine-Frankenheim, M. Geißel, M. Roth, H. Wetzler, W. Seelig, O. Iwase, P. Spiller, R. Bock, W. Süd, and D.H.H. Hoffmann. *Experiments on the Interaction of Heavy Ions with Dense Plasma at GSI-Darmstadt*. NUCLEAR INSTRUMENTS & METHODS IN PHYSICS RESEARCH A, 415:558–565, 1998.
- [61] F. Falk, J. Meinschien, G. Mollekopf, K. Schuster, and H. Stafast. *CN_x Films Prepared by Laser Chemical Vapour Deposition*. MATERIALS SCIENCE AND ENGINEERING B, 46:89–91, 1997.
- [62] J. A. Waltham, P. F. Cunningham, M. Notcutt, and M. M. Michaelis. *Ion Flow Characteristics from Laser-Produced Line Plasmas*. JOURNAL PHYSICS D: APPLIED PHYSICS, 22:766–769, 1989.
- [63] M. Chvojka, B. Králiková, E. Krouský, L. Láska, K. Mašek, O. Renner, K. Rohlena, J. Skála, O. Štirand, and P. Tenda. *An Effect of the Target Position Relative to the Laser Focus on X-Ray Emission from the Laser Plasma*. LASER AND PARTICLE BEAMS, 10(4):743–751, 1992.

- [64] F. B. Rosmej. *Hot Electron X-Ray Diagnostics*. J. PHYS. B. LETT.: AT. MOL. OPT. PHYS., 30:L819, 1997.
- [65] *NIST Atomic Spectra Database*. <http://physics.nist.gov/PhysRefData/ASD/index.html>, 2006.
- [66] *SPECTR-W3 Online Database on Spectral Properties of Atoms and Ions*. <http://spectr-w3.snz.ru>, 2006.
- [67] A. N. Mostovych, B. H. Ripin, and J. A. Stamper. *Laser-Produced Plasma Jets: Collimation and Instability in Strong Transverse Magnetic Fields*. PHYSICAL REVIEW LETTERS, 62(24):2837–2840, June 1989.
- [68] R. J. Conzemius, Shankai Zhao, R. S. Houk, and H. J. Svec. *Effect of Laser Focus on Ion Production in the Laser Ion Source for Elemental Analysis*. INTERNATIONAL JOURNAL OF MASS SPECTROMETRY AND ION PROCESSES, 61:277–292, 1984.

Index

- nhelix* , 33
- PP* filter, 42
- Ti* filter, 42
- positioning camera*, 38
- sensing camera*, 38

- angular distribution, 60
- angular intensity distribution, 42
- Arc discharge, 23

- calorimeter, 37
- collision frequency, 18
- Critical density, 21
- cyclotron frequency, 20

- damage threshold, 33
- Debye length, 18
- deep focus, 38

- f number, $f/\#$, 25
- Faraday isolator, 35
- FSSR, 48
- FSSR-1D, 49
- FSSR-2D, 49

- Glow discharges, 23

- inverse bremsstrahlung, 25

- Local thermodynamic equilibrium, 18

- Magnetic pressure, 20
- Multichannel plate, MCP, 44

- NIST, 77

- optical density, 51
- optical thickness, 30

- photodiode, use, 37
- plasma, 17
- Plasma frequency, 20
- Plasma gun, 23
- Plasma parameter, 19
- plasma temperature, 17

- Q machines, 23
- quasi-stationary vacuum plasma state, 27

- RF plasmas, 24
- rod amplifier, 34

- Soft Polarizing Aperture (SPA), 34
- spatial filters, 34

- Threshold flux, ϕ_{th} , 26

Appendix A

Program ANGULINT.f90

```
! ANGULINT.f90 version 1.25
!
! FUNCTIONS:
! ANGULINT      - Entry point of console application (Main program, man...)
!
! Example of displaying 'Hello World' at execution time and program to
! integrate the angular traces after calibrate the intensity from accounts
! to Optical density.
!
!
!*****
!
! PROGRAM: ANGULINT
!
! PURPOSE: Obtain calibrated integrations of angular traces.
!
!*****

program ANGULINT
use DATA_WORK
use OptDen
implicit none

character(40) infile !Name of the lines file.
character(40) logfile !Name of the logfile.
character(300) question
logical dum1 !Dummy logic value. Different uses.
real dum !Dummy number.
integer file_rows !Number of rows in the file.
```

```
real vector_data(1000,1) !Data vector
real vector_result(1000,1) !Results vector.
real index !Index for loops.
real max !Maximum value of the O.D. transformed file.
real row_int !Row where the integration should start or finish.
real mean_up !Value of mean data points up of row_int position.
real mean_down !Value of mean data points down of row_int position.
    logical direction !Direction of the integration (True => up and viceversa).
logical existance !If the log file exists in some form..
real integral !Integral value.
character int !Confirmation to continue go out or make another iteration.

print *, 'Hello World'
print *,''

!Input data file:
002 question = 'Data file name, please?'
    infile = file_in(question)

!To know the number of rows:
file_rows = 0
open(unit=1,file=infile)
do while (.not. eof(1))
    read(1,100 ) dum
file_rows = file_rows +1
end do
    100 format (T1, F6.4)
rewind(1)
close(unit=1)
    print *, 'The number of rows in',infile,'is:',file_rows

!Reading data file
open(unit=1,file=infile)
do index=1, file_rows
    read (1,200) (vector_data(index,1))
    !print *,vector_data(index,1)
end do
```

```
close (unit=1)
200 format (T7, F5.0)
!Transforming in O.D. values:
do index=1,file_rows
  vector_result(index,1) = dimage(vector_data(index,1))
end do

!Maximum O.D. value:
max = bigger (vector_result,file_rows,1,1)
print *,'max valor:',max

!Point of integration:
  !The point that I look is where the closest to the value max/2,
  !so the one where the "pendiente" of value - max/2 changes.
do index = 2, file_rows
  if ( (vector_result(index-1,1) - (max/2)) * ( vector_result(index+1,1) -
(max/2) ) < 0) then
    row_int = index
    print *,'Posicion fila:',row_int
    exit
  end if
end do

!Choose the integration direction:

if ( (row_int + 30 > file_rows) .or. (row_int - 30 < 0) ) then

  if ( row_int + 20 > file_rows .or. (row_int - 20 < 0) ) then

    if ( row_int + 10 > file_rows .or. (row_int - 10 < 0) ) then
      !So few points that it must be beginning or end of the file
      if ( row_int + 10 > file_rows ) then
        direction = .TRUE.
        print *,'Arrrrriba!!!'
        goto 001
      end if
    if (row_int - 10 < 0) then
      direction = .FALSE.
```

```
print *, 'Abbbbbajjjjo!!!'
goto 001
end if
    end if

do index = row_int - 10, row_int !Calculate the media of the upper part of the
!data.
    mean_up = vector_result(index,1) + mean_up
    end do
mean_up = mean_up / 10
do index = row_int +1, row_int + 10 !Calculate the media of the lower part of
!the data.
    mean_down = vector_result(index,1) + mean_down
    end do
mean_down = mean_down / 10

else !With 20 points (The 20 "then")
do index = row_int - 20, row_int !Calculate the media of the upper part of
!the data.
    mean_up = vector_result(index,1) + mean_up
    end do
mean_up = mean_up / 20
do index = row_int +1, row_int + 20 !Calculate the media of the lower part
!of the data.
    mean_down = vector_result(index,1) + mean_down
    end do
mean_down = mean_down / 20
    end if

else !With 30 points (The "30" then)
do index = row_int - 30, row_int !Calculate the media of the upper part of
!the data.
    mean_up = vector_result(index,1) + mean_up
    end do
mean_up = mean_up / 30
do index = row_int +1, row_int + 30 !Calculate the media of the lower part
!of the data.
    mean_down = vector_result(index,1) + mean_down
    end do
```

```
mean_down = mean_down / 30
end if
```

```
001 if (mean_up > mean_down) then
  direction = .TRUE.
  print *, 'Arrrrriba!!!'
  else
  direction = .FALSE.
  print *, 'Abbbbaajjjjo!!!'
  end if
```

```
!Integration:
integral = 0
if (direction == .TRUE.) then
  do index = 1, row_int
    integral = vector_result(index,1) + integral
  end do
else
  do index = row_int, file_rows
    integral = vector_result(index,1) + integral
  end do
end if
```

```
!Data presentation:
print *, 'File name:', infile
print *, 'Integral valor:', integral
print *, ''
print *, 'Writing log...'
```

```
!Writing log file:
logfile = 'integral_log.txt'
```

```
open (unit=2, file=logfile, err=003, action = 'READWRITE', pad='YES', &
& position = 'APPEND' )
write (2,*) 'file: ', infile
if (direction == .TRUE.) then
  write (2,*) 'integration initial row:', row_int, 'and direction: Arrrrriba!!!'
```

```
else
  write (2,*) 'integration initial row:', row_int, 'and direction: Abbbbjjjjo!!!'
end if
write (2,*) 'Integration value:', integral
do index=1, 3
  write (2,*) ''
  end do
close (unit=2)

!To do a new run of the program:
print *, 'New iteration? (y/n)'
read *, int
if ( int == 'y' ) then
  goto 002
else
  goto 999
end if

003 print *, 'Error file: Problems creating the log file.'

999 print *, 'Program finished.Have a nice day!'
  pause

end program ANGULINT
```

Appendix B

Module DATA_WORK.f90

```
!*****
!  
! MODULE DATA_WORK (Version 1.75)  
!  
! To handle data structures and find some useful quantities.  
!  
!*****  
module DATA_WORK  
    contains  
!*****  
!  
! FUNCTION bigger  
! CALCULATES The biggest number in a given column  
!   of the given matrix.  
!  
!*****  
real function bigger (matrix,rows,columns,take)  
    implicit none  
    integer rows, columns !Matrix dimensions  
        real matrix(rows,columns)  
    integer take !Column to select the bigger number  
    integer i !Index number  
        bigger = matrix(1,take)  
    do i=1,rows,1  
        if (bigger .LT. matrix(i,take)) then  
            bigger = matrix(i,take)  
        end if  
    end do  
end function bigger
```

```

!*****
!
! FUNCTION media
! CALCULATES The media of a given column data set
!   in the given matrix.
!
!*****
      real function media(matrix,rows,columns,take,number)
implicit none
integer rows, columns !Matrix dimensions
      real matrix(rows,columns)
integer number !Number of data to make the media of
integer take !Column to make the media
integer i !Index number
real dummy !dummy variable
      dummy = 0
      do i=1,number,1
         dummy = dummy + matrix(i,take)
      end do
      media = dummy / number
      end function media

!*****
!
! FUNCTION file_in
! GIVES The name of a file, checking if it exists.
!
!*****
      character(40) function file_in(question)
implicit none
logical file_yes !logical value (1=file exists)
character(40) infile !File name.
character(300) question !Question string.
character(Num(question)) :: ques_trunc !Blank truncated 'question' string.

      ques_trunc = question

```



```
1 print *, ques_trunc
read *,infile
inquire(file= infile, exist= file_yes)
if (file_yes == .FALSE.) then
  print *, 'The file',infile,'does not exist! Try again, please:'
  goto 1
end if
  file_in = infile
end function file_in

!*****
!
! FUNCTION num
! GIVES The number of non empty characters in a string
!
!*****
  pure integer function Num(string)
  implicit none
  character(*), intent(IN) :: string !String
Num = len_trim(string) + 1 !Number of full characters in 'question'
  end function Num

end module DATA_WORK
```


Appendix C

Module OptDen.f90

```
!*****
!  
! MODULE OptDen (Version 1.00)  
!  
! To transform counts on optical density values for various scanners.  
!  
!*****  
module OptDen  
contains  
!*****  
!  
! FUNCTION dimage  
! CALCULATES the optical density value for a given count for the  
!DIMAGE IV scanner  
! FROM Personal calibration  
!  
!*****  
real function dimage(count)  
  implicit none  
  real count  
  real P1, P2, P3 !Calibration variables.  
  
  P1 = 0.00002  
  P2 = 0.00019  
  P3 = 0.00014  
  dimage = P1*count*(1+P2*exp(P3*count))  
end function dimage  
end module OptDen
```


Acknowledgment

I would like to thank Professor Hoffmann for the opportunity to work on this exciting topic, that gave to me so many great times. I also want to thank Professor Roth who agreed to be the thesis co-advisor and his laser team at GSI which accepted me as a member. Without the guidance of both advisors I would never have been able to finish this work.

During the experimental time I had the good help of Dr. Olga Rosmej and Svetlana Korostiy from GSI and Professor Faenov and Dr. Tania Pikuz from Russia, who spent a lot of time working on the experiments. The collaboration with them made it possible to achieve the results.

The laser was managed by many good and talented people, and in order to recognize all of them I would like to mention here Gabriel Schaumann, Marius Schollmeier and Alexander Pelka. A lot of what I have learned of optics comes from conversations with them. Much of what I know today of plasma physics I owe to people who have been teaching me: Dr. Magunov and Dr. Schlegel, mainly.

As many of the readers sure know this version that you have here is the result of the interaction with many correctors: Professor Roberto Piriz, and Dr. Serban Udrea. They made this work readable and properly presented, so I would like to thank them the hard work they have done.

These years here would be more difficult without all the friends that I made during this time. Some are at GSI now, like Stanislav, Darek, Katarzyna, Gosia, Juan, Chilo, and Georgios. Others are a little bit away either in their original countries, Juan Sabin, the Timinsky or Alejandro will be good examples of that, or in different places as Alex is living currently in China and Mateusz in Frankfurt.

Just at the end I want to thank my family and Asia, always helping and supporting me, calming hysterical thoughts and pushing me through the difficulties. The fact that I was able to finish this work is partly due to their continued friendship and support.

Hiermit erkläre ich, dass ich die Arbeit selbstständig und nur mit den angegebenen Hilfsmitteln angefertigt und nicht schon früher eine Promotion versucht habe.

5. Juli 2006

Gonzalo Rodríguez Prieto

Name: Gonzalo

Surname: Rodríguez Prieto

Birth date and place: 10th - October - 1975 in Pontevedra, Galicia, Spain.

Nationality: Spanish.

Education

Diploma on Physics, Electronics. Santiago de Compostela University, Spain.
April 2003.

Title: *A digital Electronics Design for Diamond Detectors in HADES: The SDE2*

Master of Physics, Optoelectronics. Santiago de Compostela University, Spain.
October 1993 - February 2001.

Secondary school studies. Instituto de enseñanza secundaria Valle Inclán.
Pontevedra
October 1989 - July 1993.

Primary school studies.(E.G.B.) Pontevedra
October 1981 - July 1989.